PROPOSAL FOR A NEW NEUTRINO DETECTOR AT FERMILAB

F.E. Taylor and J.K. Walker

Fermilab Proposal No. 594

Scientific Spokespeople:

J. K. Walker, Fermilab
Extension No. 4272
and
F. E. Taylor, Northern
Illinois Univ., Department
of Physics, DeKalb, IL
Phone No. (815) 753-1773

PROPOSAL FOR A NEW NEUTRINO DETECTOR AT FERMILAB

P. Berge, D. Bogert, R. Hanft, F. Nezrick, T. Oshugi, L. Stutte, J. K. Walker, J. Wolfson, Fermilab National Accelerator Laboratory, Batavia, IL

G. Brandenburg, W. Busza, J. Friedman, H. Kendall, L. Osborne, L. Rosenson, Massachusetts Inst. of Tech., Cambridge, MA

F. E. Taylor, Northern Illinois Univ., DeKalb, Il

M. Abolins, W. Francis, D. Owen, Michigan State University, East Lansing, MI

February 1978

ABSTRACT

We propose a study of neutral current neutrino scattering on electron and nuclear targets. For this purpose we propose constructing a 400 ton neutrino detector for Fermilab which provides detailed kinematic information on final-state electrons, muons, and hadrons. The detector can be triggered selectively and has good sensitivity for rare processes. This allows exploration of a new range of physics inaccessible to present bubble chambers and electronic detectors. The detector design is based on plastic flash chambers. These are used to determine electron energy and angle, hadron energy flow direction, and particle identification through finely sampled shower development. We have tested a 1/10 linear scale prototype of the detector with the following results:

a. The energy and angle can be measured with high resolution for an electron. These resolutions are comparable or superior to the resolutions obtained with the Neon filled 15' B.C.

b. Muon trajectories can be measured with angular resolution of 1.8 mrad (projected angle) which is at least 3 times better than with previous electronic detectors.

c. Angular resolution for hadronic energy flow is consistent with the theoretical limit set by fluctuations in the cascade. This gives an angle resolution of 6 mrads at 100 GeV hadron energy.

The detector is modular, easy to construct, inexpensive, and has electronic readout. We estimate that we can begin taking data one year from date of approval.

Tests can begin with a subsection of the detector as it is constructed using the wide band beam and

dichromatic neutrino beam scheduled for the second half of 1978. We request a data run early in 1979 with the narrow band beam. The principal emphasis in this run will be the study of the semileptonic neutral current interactions of ν and $\bar{\nu}$.

A second exposure is requested with the wide band double horn beam. In this case, we shall obtain data on the elastic scattering of neutrinos and antineutrinos on electrons. Multi lepton (both muon and electron) production will also be studied in this exposure.

Table of Contents

I. INTRODUCTION

In the last five years experiments on the interaction of high energy neutrinos have provided clear evidence that the weak interactions remain a rich and exciting area for future investigations. Among the most dramatic discoveries have been:

1. The existence of neutral currents.[1] To study the semileptonic neutral current interactions further, it is necessary to explore both the Lorentz structure and internal symmetries of the current. This will require accurate measurements in the scaling variables x and y.
2. Events involving the production of two or more leptons.[2] The observation of enhanced strangeness production in di-lepton events is consistent with production of charmed particles. However, the unexpectedly large muon momenta observed in some tri-muon final states[2] suggests a new source of leptons. In addition, an event with four muons has recently been observed at CERN and also at Fermilab. Detection of electrons in association with muons is clearly of great interest.
3. A few events of neutrino electron elastic scattering have been observed in the bubble chambers at CERN and Fermilab and also in a counter experiment at CERN. This leptonic neutral current should be studied in much greater detail.

Thus far, it has been possible to carry out these studies only with muon-type neutrinos and with detectors with either low mass - high resolution, or high mass-low resolution.

Our detector achieves high resolution as well as high mass and is technologically straightforward to construct and hence capable of making a unique contribution.

We have designed a massive detector whose major new features include:

a. Electron identification, with measurement of both the direction and total energy of the associated shower,

b. Measurement of muon angle and momentum with much improved resolution over most previous detectors.

c. Measurement of the angle of hadronic energy flow, and of the total energy of the hadron system.

II. PHYSICS JUSTIFICATION

1. Semi-Leptonic Neutral Current Reactions

The reactions of interest are:

$$\nu_\mu(\bar{\nu}_\mu) + N \rightarrow \nu_\mu(\bar{\nu}_\mu) + \text{hadrons}. \qquad (1)$$

The major objective of this experiment is to study the energy and angular distribution of these neutral current reactions up to 350 GeV neutrino energy. The results will reveal the space-time structure of the hadronic weak neutral current and its symmetry properties.

Knowledge of the energy and direction of the incident neutrino is essential to this experiment. This is achieved with the new 350 GeV dichromatic beam[11]. The hadron total energy, E_H, and direction, θ_H, of energy flow will be determined. We have measured the angular resolution for θ_H (see Appendix A for details); it is at the theoretical limit set by fluctuations in the hadronic cascade. Our angle resolution for θ_H is almost a factor of 2 better than a similar experiment at CERN.[3] Hence a detailed study will be made of the distribution of events in q^2 and ν , or correspondingly in the scaling variables $y = E_H/E_\nu$ and $x = q^2/2M\nu$. Clear event signature will be achieved by demanding the absence of a muon of energy greater than 2 GeV in the event. A typical event rate from K neutrinos is one per 22 pulses of 1.5×10^{13} protons with the narrow band beam set at 250 GeV.

Charged current data will be taken simultaneously with the neutral current data. Not only do the charged current events provide a continuous check of the apparatus, but they also provide additional information on possible high-y anomalies in $\bar{\nu}_\mu$ reactions.

2. Neutrino Electron Elastic Scattering

We propose a wide band exposure for which the principal objective is a study of neutrino electron elastic scattering.

A. The reactions of interest are:

$$\nu_\mu + e^- \rightarrow \nu_\mu + e^- \quad (2)$$

$$\bar{\nu}_\mu + e^- \rightarrow \bar{\nu}_\mu + e^- \quad (3)$$

These reactions can proceed only through the neutral current and hence provide a sensitive test of different gauge models without the complication of hadronic structure.

For energies $E_\nu > m_\mu{}^2/2m_e = 11$ GeV the reactions:

$$\nu_\mu + e^- \rightarrow \mu^- + \nu_e \quad (4)$$

$$\bar{\nu}_e + e^- \rightarrow \mu^- + \bar{\nu}_\mu \quad (5)$$

can be studied. These reactions are different forms of the inverse muon decay and involve the charged current only.

Reactions (2), (3), and (4) can be studied immediately with the detector and existing neutrino beams. A search for the reaction:

$$\bar{\nu}_\mu + e^- \rightarrow \mu^- + \bar{\nu}_e \quad (6)$$

which violates the additive lepton number conservation law would also be made. Existing tests[4] on the allowable extent of a multiplicative law are very unrestrictive.

Both the Gargamelle[5], Aachen-Padua[6], and Columbia-BNL groups[6] have probably observed the elastic neutrino scattering process. Some progress will occur through the BEBC and Fermilab 15' exposures and also the approved counter experiment[7] aimed at this process at Fermilab. However, the neutrino-electron experiments are extremely difficult and will benefit greatly from a 400 ton detector which has the sensitivity and resolution designed to investigate these processes. We discuss later the sensitivity we shall have to different gauge models.

The neutrino flux will be monitored internally by simultaneously measuring the elastic reaction,

$$\nu_\mu + n \rightarrow \mu^- + p \qquad (7)$$

and also the reaction:

$$\bar{\nu}_\mu + p \rightarrow \mu^+ + n \qquad (8)$$

In addition, the total neutrino and antineutrino charged current cross sections will be measured to provide an independent check of the fluxes.

B. Multi Lepton Production

During the wide band exposure we propose to trigger on dimuons. Some of the unique aspects of our detector may help to identify the various mechanisms which are present in addition to charm production.

Events due to neutrino production of three muons have been observed at Fermilab and CERN.[2] There are also two events with four muons in the final state.[2] In a recent analysis, Albright[8] et. al. have concluded that no known single mechanism can account for the observations. Even the bulk of the three muon data does not seem to have a

simple origin. One of the more promising explanations of the data involves the radiative production of a muon pair in a normal charged current interaction. The consequences of this interpretation are:

a. The produced muon pair would have low invariant mass.

b. The angle of hadron energy flow is related to the angles and momenta of the muons.

The excellent muon and hadron energy flow angle resolution provided by the proposed detector will give a stringent test of either the above model or other interpretations of the data.

In addition, we propose searching for the reactions:

$$\nu_\mu + Z \rightarrow \mu\mu e + \text{"X"} \qquad (9)$$

$$\rightarrow \mu\mu ee + \text{"X"}$$

$$\rightarrow \mu\mu\mu e + \text{"X"}$$

$$\rightarrow \mu\mu\mu\mu e + \text{"X"}$$

The associated hadronic system "X" will have its energy and angle of energy flow measured. A study of these reactions involving electrons as well as muons should shed light on the origin of these interesting events.

III. DETECTOR

A. General Description

The neutrino target is to be used in conjunction with the large toroidal magnetic facility in Lab C at Fermilab. The target will have the following characteristics:

a. Large mass (we will have approximately 400 tons).

b. Fine grain sampling for hadronic energy flow measurements.

c. Selective trigger.

d. Ability to measure electrons with good angular resolution.

e. Ability to separately identify electrons by distinguishing electromagnetic from hadronic cascades.

f. Modular construction allowing reconfiguration in response to new physics results.

g. Modest cost.

The proposed detector is shown in Figure 1. The detector is 19.5 meters long and has hexagonal cross section with a 4.0 meter transverse size. The detector is located immediately upstream of the existing 7.32 meter diameter iron toroids in Lab C. Flash chambers[9] are alternated with 0.953 cm thick sheets of fiber-reinforced cement and aluminum throughout the length of the detector. A submodule is shown in Figure 2 and a full module in Figure 3. Information from the chamber is recorded directly by magnetostrictive lines and stored on magnetic tape. The detector is triggered using planes of proportional wire counters which are located at 30.4 cm intervals throughout the detector.

B. Flash Chambers

The flash chambers are constructed from extruded polypropylene plastic at a cost of $1.50/sq. meter. The

individual cells of plastic are 5 mm x 5 mm cross section and are filled with the standard spark chamber gas of 90% Ne + 10% He. Gas manifolds are thermo-vacuum formed from Uvac plastic. The gap between electrodes is chosen to be 3.5 cm. All cement sheets are covered with aluminum foil to minimize the required high voltage. When an event of interest is detected by the proportional counters a high voltage pulse of 15KV is applied across the gap, thereby causing a glow discharge in the tubes where the particles traversed the chambers. The cement planes are similar to aluminum in regard to radiation length and collision length but are considerably less expensive.

The neutrino target is built up of alternating flash chamber and cement layers. Each flash chamber plane is rotated by 60° from the previous flash chamber layer to give x-y-u coordinate measurements. A 0.6 cm sheet of lead and a plane of proportional counters are placed at 30.4 cm intervals throughout the neutrino target. The lead sheet provides discrimination of hadrons from electrons.

The total number of collision lengths in the target is 42, the total number of radiation lengths is 167 and the total weight is 400 tons.

C. Proportional Tubes

For triggering purposes, two proportional tube hodoscope detector planes will be installed in addition to the existing coarse grained scintillation hodoscopes in the 7.32 meter toroid (see Figure 4). These tubes, similar to those placed throughout the neutrino detector, will be constructed from extruded aluminum tubes in the form of 13' length, with 1" x 1/2" holes. The tubes

will be vertical in all cases. Behind the toroid one row will be stacked on top of another to cover the full 24' height of the toroid. Throughout the target, the wires in four adjacent 1" x 1/2" cross section tubes will be connected to a sin amplifier. This will result in 39 amplifiers per plane giving a total of 2,500 amplifiers in the target. Behind the toroid, each of the two planes will have a total of 576 amplifiers. The total number of channels is then 3652.

Each tube has a 50μm diameter gold plated tungsten wire centered in the 1" x 1/2" hole (see Figure 5). The filling gas mixture will be 80% argon and 20% methane which provides a high drift velocity. Our tests with a full scale 13' long detector of this form show that the output pulse from the tube occurs < 160 nsec after the particle traverses the detector. Excellent pulse height response is obtained as shown in Figure 5, which shows the spectrum obtained with Fe^{55}. As pulse height information is not required from the tubes behind the toroid but rather the digital information corresponding to whether it has been struck by a muon, we can have a cheap amplifier (< $12) on each wire. These tubes will provide a trigger for di-muons. Pulse height information is required from the planes in the target and in this case the amplifiers cost $35 each.

D. Detector Tests

An extensive series of tests have been made with the prototype detector which is approximately 10% of the length of the final proposed neutrino detector. This length is adequate for measuring the key parameters:

a. hadron energy flow angular resolution.

b. electron energy and angle resolution.

These tests have been performed in the M5 test beam in the Meson Laboratory and the N3 beam in the Neutrino Area. A full description of the tests and results are given in Appendix A.

E. Large Scale Prototype Flash Chamber Production

We have successfully constructed 8' x 4' flash chambers and read them out with the magnetostrictive system described in the Appendix B. Our present efforts are directed towards constructing the first 2 ton sub-module which is 13' x 13' x 4". We expect to construct 30 tons by July and, there after, our production rate can be 50 tons/month. We are confident that the proposed 13' x 13' chambers can be fabricated in the way described in the engineering design report issued by the Neutrino Department.[10]

F. Detector Characteristics

A summary of the properties of the detector is given in Table I.

Table I

NEUTRINO TARGET PROPERTIES

Total Mass	400 tons		
Fiducial Mass (Neutral Currents)	300 tons		
Dimensions	4.0m x 4.0m x 19.5m (Hexagonal cross section)		
Location	Lab C		
Construction	Layers of flash chambers giving 3 views sandwiched between layers of cement. Every 18 flash chamber planes there is 6mm of Pb followed by proportional counter hodoscope.		
Average Density	1.59 g/cm^3		
Calorimeter Properties		(no Pb)	(Global averag with Pb)
	Collision length:	46.1 cm	43.4
	Radiation length:	18.2 cm	11.7 cm
	Sampling every 3.5% of collision length Sampling every 9% of radiation length		
Resolutions	Vertex position:	$\pm$ 2.5mm	
	Electron Energy:	$\sigma(E_e) =$	$0.10\ E_e$
	from flash chamber and probably similar energy resolution from the proportional chambers for $E_e > 20$ GeV.		
	Electron projected angle $\sigma(\theta_e) = 2 + 70/E_e$ mrad		
	Hadron energy by use of proportional counters:	$\frac{\sigma(E_H)}{E_H} =$	$1.6/\sqrt{E_H}$
	Hadron energy flow: (Projected angle)	$\sigma(\theta_H) = 4.0 + (360/E_H)$ mrad	
	Muon momentum:	$\frac{(\Delta P)}{P} = \pm$ 15%	
Event Handling	1 event/1 msec horn pulse		

IV. SEMI LEPTONIC NEUTRAL CURRENTS

Introduction

Since the discovery[1] of the weak neutral current in 1973, there has been great interest to understand this new phenomenon. The qualitative properties of this current are at present known to be the following:

1. The neutral current couples to electrons since $\nu_\mu e^-$ scattering has been observed.
2. The neutral current couples to both u and d quarks since ν_μ-nucleus scattering has been observed.
3. The neutral current is flavor-diagonal for the coupling to charged fermions. The small branching ratio of the decay $K_L^o \rightarrow \mu^+\mu^-$ implies that the coupling of the type $\bar{s}d$ is suppressed to a high degree. In addition there is information indicating that the charm changing neutral currents of the type $\bar{c}u$ are also strongly suppressed. Off-diagonal couplings of the neutral currents to leptons such as $\bar{\mu}e$ are not present, since the decay $\mu^- \rightarrow e^-e^+e^-$ has not been seen.
4. The neutral current is not pure vector or axial vector current since $\sigma(\nu_\mu N) \neq \sigma(\bar{\nu}_\mu N)$.
5. The production of π^o's in the reactions $\nu_\mu N \rightarrow \nu_\mu N\pi^o$ and $\nu_\mu p \rightarrow \nu_\mu p\pi^o$ are consistent with the presence of both isovector and isoscalar components.[20]

The study of deep inelastic neutrino scattering through the neutral current interaction presents the opportunity for observing the weak interaction with no quark flavor change in analogy to deep inelastic electron/muon

scattering via the electromagnetic current. Of great interest is to measure both the x and y distributions of deep inelastic scattering. The x distributions for neutrino and anti-neutrino scattering have to date not been measured with high statistical accuracy. These distributions provide information on the scaled momentum distributions of the valence and sea quarks in the nucleon as probed by the weak neutral current and hence will provide unique information. Furthermore, the deep inelastic scattering off isoscalar targets provides a nontrivial test of one parameter gauge theory models like $SU(2)\otimes U(1)$ etc.

The Experiment

The proposed detector is well suited for the measurement of the x and y structure of semi-leptonic neutral currents. The detector has the following characteristics relevant to this reaction; 1) large fiducial mass ($\geq$ 300 tons) and hence high event rates in the narrow band beam, 2) good muon identification using the fine grain sampling flash chambers and the iron toroid facility, 3) accurate measurement capability of the primary vertex location (thereby increasing the y acceptance and aiding in the determination of the narrow band beam energy), and 4) accurate measurement capability of the hadron energy flow (both energy and flow direction) using the flash chambers and proportional tube counters.

To measure the semi-leptonic neutral current process, we must determine a) the kinematical acceptance, and b) the resolutions in the scaling variables x and y. We shall also discuss rates, expected backgrounds, and a trigger selective to neutral currents.

a. Kinematic Acceptance

The kinematics of the semi-leptonic neutral

current reaction is specified by the incident neutrino energy E_ν (known a priori from the narrow band beam), the incident neutrino direction, the hadron energy E_H, and θ_H, the hadron energy flow direction. These kinematic quantities are defined in the diagram.

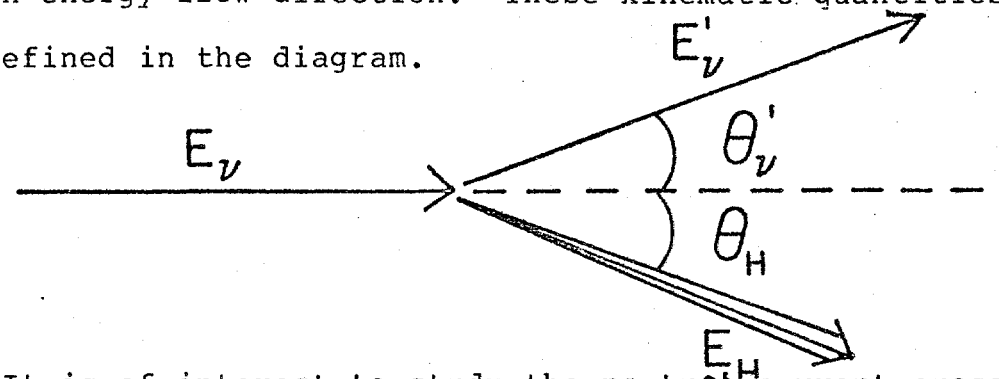

It is of interest to study the neutral current cross section $d\sigma/dxdy$, in terms of the scaling variables x and y; where:

$$x = \frac{Q^2}{2M\nu}, \quad Q^2 = 4E_\nu E'_\nu \sin^2 \frac{\theta'_\nu}{2}, \quad \nu = E_H - M \tag{10}$$

$$y = (E_H - M)/E \ , \quad M = 0.94 \text{ GeV}/c^2. \tag{11}$$

The appropriate kinematics for the Fermilab narrow band beam for neutrinos and antineutrinos are shown in figures 6a and 6b respectively. From these kinematics we see that for $y_{min} = 0.1$ the hadron energy ranges from 20 GeV to 250 GeV and the hadron energy flow direction ranges from 0° to 16°. Both of these ranges lie within the acceptance of the detector.

The acceptance in y is from 0.1 to 0.9. The lower limit of y is chosen to select only K neutrino events. This discrimination is accomplished by measuring the radial position of the primary vertex and using the different angle-energy correlations of the K neutrinos and the π neutrinos in the narrow band beam. The neutrino energy and the corresponding y min versus the radial distance from the center of the neutrino beam is shown in Figure 7a and 7b respectively and for the anti-neutrino beam in Figure 7c and 7d respectively.

(The finite secondary beam phase space has not been included in these figures.) We see that a detector radius of 1.8m at approximately 1.2km from the meson decay corresponds to y_{min} = 0.1 for both the neutrino and the antineutrino beam. The acceptance in y becomes roughly flat above y = 0.45, since for y > 0.45 no radius cut is necessary to eliminate π-neutrino events. The discrimination against charged current events requires some mininum detectable energy left to the muon (or electron) in the final state. Hence y_{max} = 0.9 which implies E_μ(min) = 14 GeV and is, therefore, easily detectable. (A muon of energy > 5 GeV will penetrate the full 19.5 meters of the detector).

The acceptance in x ranges from $0.0 \leq x \leq 1.0$, however, some inefficiency of the detector occurs at small y, large x where the hadron angle becomes large with respect to the incident neutrino direction. Since these low y events must be detected at a large radius to discriminate against π-neutrino events, some fraction of the hadron shower can sometimes escape the detector.

These considerations were included in a Monte Carlo program which computed the acceptance of the detector for neutral current events as a function of x and y. A neutral current "event" at a given x and y was accepted if: a) the primary vertex was at a radial distance from the neutrino beam axis satisfying $R_{min} \leq R_V \leq 1.8$m, where we approximate the relations in Figure 7b by $R_{min} = \frac{1}{1.17} \ln (0.5/y_{min})$ meters, b) the neutrino traveled $20\lambda_o$ (λ_o = collision length in the detector = 43.4 cm). (This was required since wide angle charge current events could be confused with neutral

current events), and c) the hadron shower could flow $15\lambda_o$ in the detector. The maximum radius of the detector was assumed to be 2.0m. The results of this calculation are shown in Table II and III for a positive secondary energy of 250 GeV and a negative secondary energy of 200 GeV respectively. The acceptance is generally > 80% over the table except for low y, or large x. The inefficiency at low y is due to the radius cut, required for K-neutrino discrimination and the inefficiency at large x is due to large angles of either the lepton or hadrons.

b. Resolution Function

The resolutions in x and y are computed by folding in the neutrino beam energy resolution, the angular resolution of the hadron energy flow (See Appendix A for the details of the measurement of this resolution), and the hadron energy resolution.

The narrow band beam resolution with the primary vertex measured by the flash chambers is assumed to be $\sigma(E_\nu) = 0.09\ E_\nu$ determined primarily by the momentum acceptance of the kaon beam. (The contribution due to the random decay locations in the decay pipe is roughly 1/2 the contribution due to the momentum acceptance of the kaon beam.) The resolution in the hadron energy flow direction (projected angle) is given by $\sigma(\theta_H) = 4.0 + 360/E_H$ (E_H in GeV and θ_H in mrad). This is determined from the measured projected angular resolution from the M5 and N3 beam line tests. This angle resolution is nearly a factor of 2 smaller than that expected for the angle resolution in the CERN WA-18 experiment.[3]

TABLE II

Acceptance Efficiency Po=250 GeV/c

y \ x	0.1	0.3	0.5	0.7	0.9
0.1	0.29	0.22	0.18	0.18	0.15
0.3	0.92	0.80	0.72	0.65	0.58
0.5	0.98	0.86	0.76	0.71	0.67
0.7	0.94	0.80	0.74	0.66	0.58
0.9	0.79	0.64	0.48	0.37	0.28

Average Acceptance = 0.60

TABLE III

Acceptance Efficiency Po=200 GeV/c

y \ x	0.1	0.3	0.5	0.7	0.9
0.1	0.28	0.22	0.17	0.17	0.15
0.3	0.91	0.78	0.71	0.63	0.57
0.5	0.98	0.85	0.74	0.70	0.64
0.7	0.94	0.79	0.71	0.63	0.55
0.9	0.77	0.60	0.44	0.31	0.22

Average Acceptance = 0.58

The hadron energy is measured by using the proportional tube counters which sample the hadronic shower every 0.6 of a collision length and every 2.6 of a radiation length. The resolution of the hadron energy is estimated to be $\sigma(E_H) = 1.6\sqrt{E_H}$ (E_H in GeV) from linearly scaling the resolution of a CITF calorimeter[12] which sampled the hadron shower every collision length in iron to the proposed calorimeter which will sample the hadron shower every 0.6 of a collision length. This also assumes that the proportional tube counters have 2.5 times worse energy resolution than scintillation counters for the same shower sampling.[12a] In addition, the flash chamber information may be used to measure the hadron energy by counting the number of cells which fire as is done for measuring electron energies. The resolution obtainable, however, by this method for hadron showers is at present unknown. Proportional tube counters sample only the ionization of the hadron system, and hence are sensitive to only the kinetic energy T_H of the hadron system and not the total energy $E_H = T_H + M_H$. Measurement of E_ν, T_H, θ_H is, however, sufficient to reconstruct the event. In fact, assuming $T_H \simeq E_H \simeq P_H$ results in an error in x of $\leq$ 14% and an error in y of $\leq$ 12%.

A Monte Carlo program was written which reconstructed measurable neutral current events at secondary beam energies of E^+ = 250 GeV and E^- = 200 GeV with the experimental uncertainties described above. The expected resolutions are shown in Table IV and V for K neutrinos in the dichromatic beam. It is noticed that the error in y is determined by the error in E_H for $E_H \geq$ 50 GeV,

TABLE IV
RESOLUTIONS P_o = 250 GeV/c

$\frac{\sigma x}{\sigma y}$

y \ x	0.1	0.3	0.5	0.7	0.9
0.1	$\frac{0.09}{0.04}$	$\frac{0.20}{0.047}$	$\frac{0.26}{0.041}$	$\frac{0.35}{0.041}$	$\frac{0.44}{0.044}$
0.3	$\frac{0.08}{0.075}$	$\frac{0.16}{0.075}$	$\frac{0.22}{0.071}$	$\frac{0.26}{0.069}$	$\frac{0.34}{0.07}$
0.5	$\frac{0.09}{0.09}$	$\frac{0.21}{0.10}$	$\frac{0.33}{0.09}$	$\frac{0.39}{0.095}$	$\frac{0.71}{0.094}$
0.7	$\frac{0.34}{0.12}$	$\frac{0.76}{0.12}$	$\frac{0.87}{0.12}$	$\frac{0.89}{0.12}$	$\frac{1.28}{0.12}$
0.9	$\frac{0.50}{0.14}$	$\frac{0.85}{0.14}$	$\frac{1.1}{0.14}$	$\frac{1.3}{0.14}$	$\frac{1.5}{0.14}$

$\sigma(E_\nu) = 9\% \; E_\nu$

$\sigma(E_H) = 1.6 \sqrt{E_H}$

$\sigma(\theta_H) = 5.66 + 509/E_H$ (mrad) (polar angle)

TABLE V
RESOLUTIONS P_o = 200 GeV/c

$\frac{\sigma x}{\sigma y}$

y \ x	0.1	0.3	0.5	0.7	0.9
0.1	$\frac{0.095}{0.095}$	$\frac{0.20}{0.048}$	$\frac{0.28}{0.044}$	$\frac{0.37}{0.043}$	$\frac{0.46}{0.045}$
0.3	$\frac{0.087}{0.079}$	$\frac{0.17}{0.079}$	$\frac{0.23}{0.074}$	$\frac{0.28}{0.074}$	$\frac{0.36}{0.073}$
0.5	$\frac{0.093}{0.10}$	$\frac{0.22}{0.11}$	$\frac{0.37}{0.099}$	$\frac{0.56}{0.10}$	$\frac{0.54}{0.10}$
0.7	$\frac{0.37}{0.13}$	$\frac{0.72}{0.13}$	$\frac{0.87}{0.13}$	$\frac{1.09}{0.12}$	$\frac{1.27}{0.12}$
0.9	$\frac{0.45}{0.14}$	$\frac{0.81}{0.15}$	$\frac{1.1}{0.15}$	$\frac{1.1}{0.15}$	$\frac{1.5}{0.15}$

$\sigma(E_\nu) = 9\%\ E_\nu$

$\sigma(E_H) = 1.6\ \sqrt{E_H}$

$\sigma(\theta_H) = 5.66 + 509/E_H$ (mrad) (polar angle)

while for $E_H < 50$ GeV, it has roughly equal contributions from the errors in the incident neutrino energy and in the hadron energy. The error in x depends on all the measured quantities E_ν, E_H, and θ_H and hence is correspondingly larger.

The mass of the hadron system may also be reconstructed by computing $M_H^2 = M_p^2 + 2 M_p E_\nu - 2M_p E'_\nu - Q^2$. The approximation $T_H \approx E_H$ underestimates the mass by $\sim$ 8%, but this is small compared to the mass resolution $\sigma(M_H) = 13\%$. Including the hadron shower opening angle and the initial structure may improve this resolution somewhat. A study of the hadron system for charged current events will be performed.

C. Event Rates

The neutral current event rates are computed by assuming:

$$\frac{d\sigma(NC)}{dxdy} = \frac{d\sigma(CC)}{dxdy} \quad \frac{\sigma(NC)}{\sigma(CC)} \tag{12}$$

where we take[13]

$$\frac{d\sigma^{\nu_\mu N}(CC)}{dxdy} = \frac{G^2 M E_\nu}{\pi} F_2^{\nu_\mu N}(x) \tag{13}$$

$$\frac{d\sigma^{\bar{\nu}_\mu N}(CC)}{dxdy} = \frac{G^2 M E_\nu}{\pi} F_2^{\nu_\mu N}(x)\,(1-y)^2 \tag{14}$$

We shall approximate: $F_2^{\nu N}(x) = \frac{1}{1.8} F_2^{ed}(x)$ measured at SLAC.[14] We assume:

$$\frac{\sigma^{\nu_\mu}(NC)}{\sigma^{\nu_\mu}(CC)} = 0.29 \text{ and } \frac{\sigma^{\bar{\nu}_\mu}(NC)}{\sigma^{\bar{\nu}_\mu}(CC)} = 0.36 \tag{15}$$

The target fiducial mass is 300 tons with a fiducial cross section of $10m^2$ corresponding to 1.8×10^{32} nucleons or 1.8×10^{27} nucleons/cm^2 presented to the narrow band beam. The incident neutrino flux is determined by the new "twisted beam" version of the narrow band beam.[11] It is assumed that both the neutrino and anti neutrino flux is uniform over the fiducial area of radius 1.8 m. The rates are calculated for 6×10^{18} protons on target for both neutrino and antineutrino exposures. The secondary beam momentum is set at 250 GeV/c for neutrinos and at 200 GeV/c for anti neutrinos.

Putting all these factors together we have: (for kaon-neutrinos)

$$\frac{dN^{\nu_\mu N} \text{ events}}{dxdy} = 50604 \; F_2^{\nu_\mu N}(x) \tag{16}$$

$$\frac{dN^{\bar{\nu}_\mu N} \text{ events}}{dxdy} = 6694 \; F_2^{\bar{\nu}_\mu N}(x) \; (1 - y)^2 \tag{17}$$

Folding in the acceptance with these differential rates, we find the rates (in bins $\Delta x = 0.2$ and $\Delta y = 0.2$) given in Tables VI and VII. The rates are for the K-neutrinos component of the narrow band beam.

We note that for the neutrino exposure, it is possible to measure out to $x = 0.8$. For the anti-neutrino exposure, data may be taken out to $x = 0.6$. Increased statistics for antineutrinos may be obtained by running the secondary momentum at 100 GeV instead of 200 GeV. The K^- rates in the secondary beam would be increased by a factor of 5. We shall measure the neutrino induced neutral currents first and judging from our experience, select an appropriate anti-

TABLE VI

ν_μNC Event Rate Po=250GeV/c

y \ x	0.1	0.3	0.5	0.7	0.9
0.1	796	404	108	18	0.5
0.3	2345	1448	443	66	2
0.5	2521	1570	468	72	2
0.7	2404	1464	452	67	2
0.9	2027	1157	293	37	1

Σ=18,119

TABLE VII

$\bar{\nu}_\mu$ NC Po=200 GeV/c, Event Rate

y \ x	0.1	0.3	0.5	0.7	0.9
0.1	70	39	10	2	0.05
0.3	138	84	26	4	0.1
0.5	76	47	14	2	0.06
0.7	26	16	5	1	0.02
0.9	2	1	0.3	0.03	0.001

Σ=564

neutrino beam energy.

d. Backgrounds

Background events in the measurement of neutral currents have several sources. There can be cosmic ray events with an incident neutral particle which can mimic a neutral current event. These events may be reduced by using a short beam spill and by mixing a known sample of cosmic ray events with neutrino events by triggering the detector during the accelerator off time.

The background due to charged current events is not serious. The $y < 0.9$ cut requires that the muon from charged current events has $E_\mu > 14$ GeV. Charged current muons which are contained within the fiducial volume will travel at least 20 interaction lengths. A large fraction of the muons which leave the ficucial volume at large angle will strike the tube plane placed behind the first 24 foot toroid magnet and will be vetoed. The monitoring of charge current events allows a subtraction of this background by extrapolating the charge current data distributions.

A Monte Carlo study was performed to determine the veto inefficiency of the veto wall behind the 24 foot toroid. For charged current events for $\theta_\mu \leq 5°$, the veto efficiency is excellent. For $\theta_\mu > 5°$, the efficiency drops off becoming ~0.55 for large angles. The efficiency is given in Table VIII.

The background from the wide band neutrinos in the narrow band beam is small. From the design report of the twisted narrow band beam,[11] this background is < 6% for both neutrino and anti-neutrino beams. A measurement of this background may be made by taking data with the secondary beam slits closed.

The background of $\nu_e + N \rightarrow e^- +$ hadrons with the electromagnetic shower and the hadronic shower mixed together can simulate a neutral current event. This background can be calculated[16] and is estimated to be (1-3)% of the neutral current rate and hence is easily subtracted from the data.

Incident neutrons and photons from interactions upstream can simulate neutrino interactions in the neutrino detector - target. These backgrounds can be estimated by measuring the longitudinal position of a primary interaction. Neutron and photon events will show a characteristic short attenuation length, whereas for neutrino events this attenuation length will be infinite.

e. Trigger

To trigger on neutral currents, we require a local energy deposition of > 10 GeV together with a veto at the back of the 24 foot toroids and a veto at the

TABLE VIII
MUON VETO EFFICIENCY

P_o = 200/250 GeV/c

y \ x	0.1	0.3	0.5	0.7	0.9
0.1	1.0/1.0	1.0/1.0	1.0/1.0	1.0/1.0	1.0/1.0
0.3	1.0/1.0	1.0/1.0	1.0/1.0	1.0/1.0	1.0/1.0
0.5	1.0/1.0	1.0/1.0	1.0/1.0	1.0/1.0	0.995/0.997
0.7	1.0/1.0	1.0/1.0	0.990/0.991	0.960/0.970	0.920/0.938
0.9	0.994/0.998	0.875/0.896	0.733/0.776	0.635/0.681	0.551/0.591

front of the detector. Experience with the two existing neutrino detectors has shown that this trigger is adequate to keep the trigger rate to less than one trigger per millisecond of beam. This simple trigger is $\geq$ 99% efficient except for large x and/or for large y. Another trigger will be used to simultaneously record charged current events.

f. Simulation of the Experiment

To simulate the deep inelastic scattering via the neutral current, a Monte Carlo program was written which generated events with a given x and y dependence with the appropriate statistics. These events were required to meet the acceptance criteria for unambiguous K-neutrino events discussed above. The accepted events were reconstructed with the experimental resolutions in the incident neutrino energy, hadron energy and hadron energy flow angle. The x and y distributions were then computed by dividing out the apparatus acceptance. Finally these distributions were compared with the input distributions.

The neutrino and anti-neutrino events were generated by equations 16 and 17 respectively with $F_2^{\nu_\mu}(x) \sim (1 - x)^3$. A cut for y (measured) $\leq$ 0.8 was made since the large y events have a poor x resolution. The "measured" distributions are shown in Figure 8 through 11. The x distributions are for all y $\leq$ 0.8, and the y distributions are for all x. One sees that the power of the (1 - x) dependence is nicely reconstructed for both neutrino and anti-neutrino running conditions. For neutrino running, a cut in y can be used to

determine the x -distribution for various values of y, and vise-versa. For anti-neutrino running this may be done in coarse bins which separate low y from high y.

In summary, the x and y resolutions are quite adequate to determine the x and y distributions for both neutrino and anti-neutrino running.

V. NEUTRINO ELECTRON ELASTIC SCATTERING

A fundamental reaction to be studied in neutrino physics is the pure neutrino-lepton elastic scattering. This reaction allows the weak neutral current to be studied with no complicating hadron physics, and hence, is a major test of the theory. Several major difficulties must be overcome in this study. They include: a) low event rate requiring a large mass detector, and b) large backgrounds which necessitate a fine-grained high resolution detector and good prompt triggering. We shall first discuss background discrimination for the elastic neutrino-electron scattering reaction:

$$\nu_\mu e^- \rightarrow \nu_\mu e^- \tag{18}$$

There exist two important sources of background, the quasi-elastic inverse beta-decay of the neutron:

$$\nu_e n \rightarrow p e^- \tag{19}$$

and single π° production by the neutral current neutrino interaction:

$$\nu_\mu N \rightarrow \nu_\mu N \pi^\circ \tag{20}$$

Both background reactions are dominated by nucleon form factors with masses $\sim m_p$ and tend to constant cross sections of

$$\sigma(\nu_e n \rightarrow p e^-) = 10^{-38} \text{cm}^2 \tag{21}$$

$$\sigma(\nu_\mu N \rightarrow \nu_\mu N \pi^\circ) = 2 \times 10^{-39} \text{cm}^2. \tag{22}$$

a. Event Rates and Background Rates

Electrons from elastic $\nu_\mu e$ scattering are peaked in a forward cone of angle $\theta_e \simeq \sqrt{\frac{2m_e}{E_\nu}}$ where E_ν is the energy of the incoming neutrino. They are therefore, confined to small

transverse momenta, $p_\perp \leq 200$ MeV/c. Electrons from the inverse beta-decay process have a much broader $p_\perp$ distribution, with a $< p_\perp > \simeq 500$ MeV/c. Thus, it is feasible to discriminate between the two reactions using a cut in $p_\perp$.

Figure 12 shows the expected number of events for $\nu_\mu e$ elastic scattering and inverse beta-decay as a function of $p_\perp$. To obtain these distributions, the following assumptions were made:

1. 2×10^{13} protons/pulse at 400 GeV
   12 second cycle time
   1,000 hours of running
   i.e., 6×10^{18} protons on target
2. The two horn system neutrino beam[15]
3. $\frac{\nu_e}{\nu_\mu} \simeq 0.01$
4. A 360 ton fiducial volume in this detector.
5. For $\sigma(\nu_\mu e \rightarrow \nu_\mu e)$ the following was used
   i. A Weinberg angle of $\sin^2\theta_W = 0.35$
      (i.e., $\sigma \simeq 10^{-42} E_\nu \text{ cm}^2$)
   ii. The functional form[17]

$$\frac{d\sigma^{\nu,\bar{\nu}}}{dE_e} = \frac{G^2 m_e}{2\pi E_\nu^2} \left[E_\nu^2 (g_v \pm g_A)^2 + (E_\nu - E_e)^2 (g_v \mp g_A)^2 + m_e E_e (g_A^2 - g_v^2) \right] \quad (23)$$

where $g_V = -1/2 + 2\sin^2\theta_W$

$g_A = -1/2$

Estimate of the Background:

$$\begin{cases} \nu_e n \rightarrow p e^- \\ \bar{\nu}_e p \rightarrow n e^+ \end{cases} ;$$

1. The functional form[18]

$$\frac{d\sigma^{\nu,\bar{\nu}}}{dE_e} = \frac{M^3 G^2 \cos^2\Theta}{4\,E^2}\left[A \mp B\,\frac{(S-U)}{M^2} + C\,\frac{(S-U)^2}{M^4}\right] \text{ is used,} \qquad (24)$$

where $S-U = 2M(E_\nu + E_e)$

$$A = \frac{Q^2}{4M^2}\left[\left(4 + \frac{Q^2}{M^2}\right)F_A^2 - \left(4 - \frac{Q^2}{M^2}\right)F_{V1}^2 \mp \frac{Q^2}{M^2}\left(1 - \frac{Q^2}{4M^2}\right)F_{V2}^2 + \frac{4Q^2}{M^2}F_{V1}F_{V2}\right]$$

$$B = \frac{Q^2}{M^2}F_A\,(F_{V1} + F_{V2})$$

$$C = \frac{1}{4}\left(F_A^2 + F_{V1}^2 + \frac{Q^2}{4M^2}F_{V2}^2\right)$$

and F_{V1}, F_{V2}, and F_A are the usual dipole-formula nucleon form factors.

The total number of events expected is 697 for $\nu_\mu e^- \rightarrow \nu_\mu e^-$ and 1802 for $\nu_e n \rightarrow p e^-$. A $p_\perp$ cut of 160 MeV/c reduces these numbers to 661 and 79 respectively (12% background, experimental resolution not included). (Since $p_\perp \approx \sqrt{2m_p T_p}$, this is equivalent to the restriction on the kinetic energy of the proton $T_p < 13.6$ MeV, (roughly the energy necessary to penetrate one cm of cement.) In addition, it has been shown[19] that when inverse beta-decay takes place on bound neutrons, there will be significant suppression of this background due to Pauli exclusion. This has been included in the Monte Carlo as a multiplicative factor.

$$R(\vec{Q}) = \frac{3}{2}\frac{\vec{Q}}{2P_F} - \frac{1}{2}\left(\frac{\vec{Q}}{2P_F}\right)^3 \qquad \text{For} \quad \vec{Q} < 2P_F$$

$$= 1 \qquad \text{For} \quad \vec{Q} > 2P_F \qquad (25)$$

where: $\vec{Q} = \sqrt{Q^2 \left(1 + \frac{Q^2}{4M^2}\right)}$

and $P_F = 0.266$ GeV/c

This low Q^2 suppression reduces the background to about 4% under the elastic peak.

As mentioned earlier, the experimental resolutions as determined in the test apparatus were $\frac{\Delta E}{E} = \pm$ 10% and projected angle $\sigma(\theta_e) = 2 + 70/E_e$ (mrad). The resolutions were incorporated into the above Monte Carlo studies.

The angular resolution obtained in the test apparatus is for a projected angle. The Monte Carlo calculation uses a polar angle, so that for the calculation the resolution was multiplied by $\sqrt{2}$.

In addition, in the final apparatus, the average radiation length is 11.7 cm, compared to 10cm for the test apparatus, so that the resolution used was $\sigma(\theta_e) = \sqrt{2} \times 10/11.7 \times (2 + \frac{70}{E_e})$mrad = $(2.42 + \frac{84.6}{E_e})$mrad.

The results are shown in Figures 13 and 14 . The electron energy spectra (Figure 13) is relatively independent of the resolutions.

The $p_\perp$ distribution, (Figure 14) therefore, was calculated incorporating only the angular resolution, since this is by far the dominant source of error.

This distribution has been smeared, but separation of the two processes is clearly possible. The background for a $P_\perp$ cut of 160 MeV/c is estimated to be 17% and can be statistically subtracted by observing the inverse beta-decay

rate at higher $P_{\perp}$ and using the predicted curve to extrapolate to smaller $P_{\perp}$.

Background Due to $\nu_\mu N \to \nu_\mu N\pi^o$

This background is potentially much more serious than is inverse beta-decay since the ν_μ flux is 100 times the ν_e flux. Present data on this reaction indicates that the $(N\pi^o)$ system is dominantly $\Delta(1236)$.[20] One can express the energy of the Δ as:

$$E_\Delta = \frac{M_\Delta^2 + m_N^2 + Q^2}{2m_N}$$

so that the kinetic energy of the Δ is roughly the same as that of the proton in inverse beta-decay (Figure 15). If one considers the worst case, i.e., the π^o takes away the maximum possible energy, $E_{\pi^o} \approx E_\Delta - M_N$, then:

$$E_{\pi^o} = \frac{M_\Delta^2 - M_N^2 + Q^2}{2M_N} .$$

Assuming this reaction is strongly damped by hadronic form factors similar to the corresponding charged current single-pion reactions[21] a Monte Carlo simulation has been made.

In this model, the relative rates for the processes (18) and (20) are 1:166, as shown in Table VII. The neutrino flux is obtained from the Wang parameterization of particle production.

TABLE VII.

CUT	$\frac{\nu_\mu e \to \nu_\mu e}{\nu_\mu N \to \nu_\mu \Delta(1236)}$
None	1/166
$E_\gamma > 1$ GeV	1/1
$E_\gamma > 1$ GeV $P_T^\gamma < 0.2$ GeV/c	15/1
$E_\gamma > 1$ GeV $P_T^\gamma < 0.2$ GeV/c $\theta_\gamma < 100$ mrad	30/1

Clearly, the background from reaction (20) should be at most few percent, especially since a further reduction will be realized by demanding no other hadrons from the vertex.

As further evidence that this background is well in hand, consider the results of a CERN group[6] who studied the four fermion process in a beam of average energy $< E_\nu > = 1.5$ GeV with a detector of the same sampling frequency. Their background from $\nu_\mu N \to \nu_\mu N\pi^0$ was estimated to be $\approx 50\%$. The Fermilab two horn beam has $< E_\nu > = 35$ GeV. Since the four-fermion cross section rises linearly with energy, while $(\nu_\mu N \to \nu_\mu N\pi^\circ)$ is constant, estimated backgrounds from this process should only be a few percent.

Table VIII gives predictions of event rates and background employing the above cuts.

TABLE VIII
EVENTS EXPECTED
(Experimental Resolutions and Cuts Included)

Neutrino Running

Process	Total	$P_- < 160$ MeV/c	$E_e > 5$ GeV
$\nu_\mu e^- \to \nu_\mu e^-$	697	565	362
$\bar{\nu}_\mu e^- \to \bar{\nu}_\mu e^-$	84	64	52
$\nu_e n \to p e^-$	1,613	64	62
$\bar{\nu}_e p \to n e^+$	73	3	3
$\nu_\mu N \to \nu_\mu N \pi^o$	116,000	-	12
$\bar{\nu}_\mu N \to \bar{\nu}_\mu N \pi^o$	13,900	-	< 2

Anti-Neutrino Running

$\nu_\mu e^- \to \nu_\mu e^-$	121	90	65
$\bar{\nu}_\mu e^- \to \bar{\nu}_\mu e^-$	706	570	435
$\nu_e n \to p e^-$	183	9	9
$\bar{\nu}_e p \to n e^+$	883	34	33
$\nu_\mu N \to \nu_\mu N \pi^o$	20,000	-	2
$\bar{\nu}_\mu N \to \bar{\nu}_\mu N \pi^o$	117,000	-	14

Determination of g_V and g_A

Leptonic elastic scattering processes can all be described by two parameters, the vector and axial vector coupling constants, g_v and g_A (Eq. 23). The world's data, to date, on determining these two parameters is shown in Figures 16 & 17(data are from references 22 and 23). How much of an improvement can be obtained from this experiment, and what possible models can be eliminated?

Table VIIIA gives numbers of events expected for neutrino and anti-neutrino running for three distinct models.[24,25] Experimental resolutions are included, and the numbers are for the cuts $p_\perp < 160$ MeV/c and $E_e > 5$ GeV. The latter cut is conservative and may be required from the point of view of cosmic ray background. (As indicated earlier, 1 GeV would be adequate to reject $\Delta \rightarrow n\pi^\circ$ background.) The large differences in number of events predicted make it quite easy to differentiate between these 3 separate models given the 10% (or better) statistics expected.

Shown on Figure 18 is the kind of accuracy one can obtain on g_V and g_A assuming 10% statistics and a 20% systematic error in determining the $\nu_\mu e^-$ and $\bar{\nu}_\mu e^-$ elastic cross sections. The graph shown assumes the Weinberg-Salem model with $\sin^2\theta_W = 0.35$. It can be seen that the accuracy of determining g_V and g_A has increased by roughly an order of magnitude over previous data.

TABLE VIIIA

Events Expected

(Experimental Resolutions Included)

	Salam-Weinberg[17] $g_V = -\frac{1}{2} + 2\sin^2\theta_W$ $g_A = -\frac{1}{2}; \sin^2\theta_W = 0.35$	Vector[24] $g_V = -0.24$ $g_A = 0$	Ambidextrous[25] $g_V = 0.2$ $g_A = -0.25$
Neutrino Running			
ν_μ	362	122	91
$\bar{\nu}_\mu$	52	7	21
Anti-Neutrino Running			
$\bar{\nu}_\mu$	435	61	173
ν_μ	65	21	17

Trigger

It is essential to reduce the trigger rate for neutrino interactions to less than one per pulse. The total interaction rate can be estimated by scaling from the observed rates in the 15' chamber with the double horn focussed beam. This rate is 0.75 events/15 metric tons/10^{13} protons on target. With the 400 ton target, we then expect 20 events/pulse of 10^{13} protons. Hence, we must have a rejection factor of one hundred against semi-leptonic neutrino events to achieve no more than 20% dead time for the rare elastic electron scattering events.

There are two characteristics of hadronic cascades which distinguish them from the electromagnetic showers produced by the events of interest. These characteristics are the large transverse width and longitudinal penetration of hadronic cascades. We consider these in turn.

A. Transverse

Consider a neutrino induced event with vertex location between planes 0 and 1. We define a trigger as the following: (1) veto in plane 0; (2) 1 or 2 of the 4" proportional counters in plane 1 with at least a minimum ionizing pulse height; (3) same as (2) in plane 2; (4) 1,2, or 3 of the 4" proportional counters in plane 3 with at least a minimum ionizing pulse height.

The electronics required for this logic is quite

simple. We have applied these trigger criteria in an off-line manner to the hadronic and electromagnetic events in our test calorimeter. The measured efficiency for the two types of events are shown in Figure 19. The result is that an efficiency for electrons of $\geq$ 90% is achieved and a hadron rejection that varies from 2:1 at 5 GeV to 30:1 at 40 GeV.

B. Longitudinal

Our test calorimeter is not long enough at energies greater than 5 GeV to use our data as a means of studying the effects of longitudinal development on the trigger. However, for the 5 GeV electron and hadron data we considered a trigger which demanded a veto in proportional plane number 7 in addition to the "transverse trigger" described earlier. The resulting electron efficiency is still 98% and the hadron rejection ratio is 50:1. For energies of 10 GeV and above we have to use other data on the longitudinal development of hadronic cascades. Figure 20 shows the number of minimum ionizing particles, or equivalent, versus collision lengths and radiation lengths. At 20 radiation lengths there is still the equivalent of 8 minimum ionizing particles for a 10 GeV hadron cascade. Hence a requirement of a veto at that depth would reject hadrons and yet retain very high efficiency for electrons. At 20 GeV we can go 28 radiation lengths deep and still retain a pulse height equivalent to 8 x minimum ionizing. We would probably demand several vetoes in adjacent planes starting at an appropriate depth from the interaction

vertex. We expect that this will provide a factor of at least three rejection against hadrons in addition to that obtained in the "transverse trigger".

C. Charged Current Event Rejection

The longitudinal trigger described above will reject a large fraction of all charged current neutrino events. Typically muons of energy greater than 1 GeV will be rejected and hence for 30 GeV neutrinos this will provide an automatic 30:1 rejection of all charged current events on the basis of muon rejection. The additional factor of 3, to obtain 100:1, should easily be obtained by hadron rejection as described earlier.

D. Semileptonic Neutral Current Event Rejection

There are 0.27 x 20 = 5.6 events/pulse of 10^{13} protons. Hence, we require a rejection factor of about 30 against the hadronic cascades initiated by neutral currents. Above 30 - 40 GeV the "transverse" trigger described earlier accomplishes this rejection factor. However, in the range 5 - 30 GeV the additional rejection provided by the "longitudinal " trigger is required. Because the "transverse" rejection factor is about 10:1 in this range the required longitudinal rejection factor is about 3:1. We expect that this can be accomplished as described earlier.

Monitoring the $\nu_\mu, \bar{\nu}_\mu$ Flux

The flux of $\nu_\mu, \bar{\nu}_\mu$ can be internally monitored using the quasi-elastic reaction:

$$\nu_\mu n \rightarrow \mu^- p, \; \bar{\nu}_\mu p \rightarrow \mu^+ n \qquad (20)$$

where the energy distribution of the μ^- is related to the neutrino energy spectrum and the resolution here is $\Delta E_\mu / E_\mu \sim 15\%$.

For 10^{18} protons on target and assuming the Wang neutrino flux a detector fiducial area of 10 m^2 gives a total of 39,000 events, as shown in Table IX. Here, the form factor parameterization determined at low energy is assumed.[26]

TABLE IX.

CUTS	$\mu^- p$ EVENTS
None	39,000
$\theta_\mu < 10°$	39,000
T_p (MeV) > 50 MeV	29,000
$\theta_p < 70°$	14,000

Taking only events where a recoil proton track is observed thereby allowing a coplanarity check to be applied to suppress background,[27] a sample of $\sim$12,000 events will be used to obtain the flux shape.

The Gargamelle collaboration has demonstrated that it is possible to extract the quasi-elastic cross section from a complex nucleus target and has shown the background problems are not serious.[28]

We are presently estimating the extent to which we can use the reaction:

$$\bar{\nu} + p \rightarrow \mu^+ + n$$

to monitor the anti-neutrino flux. We have not come to any conclusion in this matter.

With a prescaled trigger we shall also measure the charged current neutrino and anti-neutrino total cross sections. This will provide and independent check on the fluxes.

The $\bar{\nu}_\mu$ elastic scattering rate is about one third of the ν_μ and the background is now from the $\mu^+\pi^\circ n$ final state. With the conservative assumption that photons with $E_\gamma >$ 50 MeV are recognized, this background is less than 5%. This background would again be further suppressed by recognition of a further photon or the neutron. The $\bar{\nu}_\mu$ energy determination is little influenced by missing the neutron since $T_n \lesssim 1$ GeV. Since the hadron is not required to be observed, a sample of $\sim$ 14,000 events will be available for flux determination.

Monitoring Electron Detection Efficiency

The electron detection efficiency of the entire detector assembly can be continuously monitored in our apparatus. By selecting muon-electron scatters produced by muons traversing the entire detector events having scattered electrons with energy greater than 5 GeV can be recorded. We estimate that 1% of all such events will yield these muon-electron events, sufficient for calibration purposes. The energy and angle of muon can be measured by the muon spectrometer to determine the electron kinematics.

VI . Data Analysis Approach

It is likely that the events for the elastic scattering processes will be buried beneath backgrounds by a factor of 100 or more. Although in principle, one could do the full analysis of these events on a digital computer, it may well prove advantageous, in order to get some data out quickly, to have a human operator select some events for preferential processing. To accomplish this, the vertex region of an event would need to be viewed by a scanner, who could make pattern decisions more rapidly and surely than selection by a digital computer. Thus a "play back" system for the electronically digitized data is envisioned. Commercially available digital displays are available with the capability of displaying a discrete raster of 1024 by 1024 points. A single "view" of the proposed detector will require less than this number of points even if every polypropylene flash tube were required to be represented. On the other hand, it is not perhaps necessary to view the entire detector to that accuracy, and a bunching of the data by a factor of 2 tubes mapped into a single display point would permit viewing the entire detector at once. If the operator selected a vertex region, that region could be displayed at full scale or even magnified. There are several types of commercially available computer driven display systems with the general capabilities outlined above.

There are two types of data recording envisioned during the phases of construction outlined in this proposal. During the first few months during which tests are being performed the muon spectrometer will continue to be operated in an optical recording mode with the existing spark chambers.

These data may be viewed on a standard 70 mm scanning table and are already being digitized on the Fermilab SAMM device. The new detector will be read out electronically, but a single module may be photographed simultaneously during the trial runs. Comparisons of the electronic and optical read out systems will verify the performance of the electronic readout. It is possible that one of the three views may be photographed in the complete configuration. This would provide an important check of the electronic readout. The advisability of this will become clearer as a result of the early tests with 30 tons.

We will install flash chamber modules between all of the toroids to provide a complete electronic readout system for the muons. The momentum resolution for the tracks will not be reduced below that obtained with the existing system. The transformation to an all electronic system for the toroids will be done adiabatically to ensure continuous use of the muon facility during the one year period of construction, installation, and testing of the detector.

VII COSTS AND TIME SCHEDULE

The estimate of material cost for the detector is shown in Table IX. The total cost of the detector is estimated to be $654,000. Labor cost for the 400 ton detector fabrication has been estimated by the Neutrino Lab to be $100,000 and is included. The construction of the flash chambers, driving high voltage electronics and magnetostrictive readout can proceed immediately. No new technological developments are required. An engineering design study for rapid production of the detector has been made by the Neutrino Lab staff. The study shows that the complete detector would be operational 12 months from the time of approval. We request that Lab C be available in April, 1978 at which time we would start to install the first 30 tons of detector. This section would be operational by July and be used in conjunction with the double horn beam during the period July through October. Many operational questions could be addressed during this period, including questions of backgrounds, reliability of magnetostrictive readout system, high voltage pulsing requirements, etc., all under the conditions of the 2 msec wide beam pulse and the electrically noisy conditions of Lab C. We consider this approach as a prudent and essential first step before going into full production on the target.

In parallel with this effort, our target production facility would be expanded to a 50 ton per month capacity. Full production would start in August and be complete in March 1979. The target would be stacked in place in Lab C as it was produced. By December, 1978, there would be about 200 tons of target which could be tested with the scheduled narrow band beam exposure. Starting in April, 1979, we will be

ready for a data run. The triggering and backgrounds will undoubtedly be relatively straightforward for the narrow band beam exposure to study semi-leptonic neutral current interactions. For this reason, we think it may be appropriate to have this exposure first. However, we will be ready to run with the wide band beam if required by the schedule.

TABLE IX

L.	Flash Chambers	
	400 ton detector (including labor costs)	
	150 submodules at $2495 each	$374,000
	High Voltage electronics (the E-310 Marx generators will be used.)	$ 20,000
	Subtotal	$394,000
2.	Lead	
	57 sheets (removed from E-310 gamma catchers.	
3.	Flash Chamber Read-Out System	$100,000
5.	Proportional Tube Detectors	
	Extruded aluminum at $1/lb.	$ 6,000
	Wire mounting at $3/wire	$ 3,000
	Electronics at $12/channel amp.	$ 14,000
	Electronics at $35/channel amp.	$128,000
	Gas connections	$ 3,000
		$154,000
	Total Cost	$654,000

REFERENCES

[1]F. J. Hasert, et al., Phys. Lett. 46B, 138 (1973).

[2]Di-Lepton:

A. A. Benvenuti, et al., Phys. Rev. Lett. 34, 419 (1975).

B. B. C. Barish, et al., Phys. Rev. Lett. 36, 939 (1976).

C. J. Blietschau, et al., Phys. Lett. 60B, 207 (1976).

D. C. Baltay, in Proc. of APS Div. of Particles and Fields, BNL, Upton, NY, 6-8 Oct., 1976 (unpublished).

E. F. A. Nezrick, et al., Bull. Am. Phys. Soc. 22, 35 (1976).

F. J. F. Grivaz, et al., Bull. Am. Phys. Soc. 22, 25 (1976).

G. J. von Krogh, et al., Phys. Rev. Lett. 36, 710 (1976).

Tri-Muon:

H. A. Benvenuti, et al., Phys. Rev. Lett. 38, 1110 (1977).

I. B. C. Barish, et al., Phys. Rev. Lett. 38, 577 (1977).

Quadri-Muon:

J. Private communication from J. Steinberger and D. Cline.

[3]Winter, et al., CERN WA-18, CERN/SPSC/75-59/P49.

[4]T. Eichten, et al., Phys. Lett. 46B, 281 (1976).

[5]F. J. Hasert, et al., Phys. Lett. 46B, 121 (1976).

[6]H. Faissner, et al., Proc. Intl. Neutrino Conference, Aachen, 223 (1976) and C. Baltay (private communication).

[7]L. Mo, et al., Fermilab Proposal 253.

[8]C. Albright, private communication.

[9]M. Conversi, et al., EP Internal Report (76-20).

[10]Report issued by W. Nestander; Neutrino Lab.

[11]D. Edwards and F. Sciulli, Fermilab TM-660; D. Edwards, S. Mori and S. Pruss, TM-661.

[12]F. Sciulli, Proc. of Calorimeter Workshop, Fermilab, 79 (1975).

[12a] R. L. Anderson, et al., SLAC-PUB-2039 (1977).

[13]L. M. Sehgal, Phenomenology of Neutrino Reactions, ANL/HEP/PR75-45 (1975).

[14]A. Bodek, PhD. Thesis, MIT (1972), (LNS-COO-3069-116).

[15]Fluxes calculated using the program NUADA, with the Wang spectrum.

[16]B. C. Barish, CALT 68-535.

[17]G. 't Hooft, Nucl. Phys. B35, 167 (1971).

[18]C. H. Llewellyn Smith, Physics Reports 3C, 261 (1972).

[19]J. S. Bell and C. H. Llewellyn Smith, Nucl. Phys. B28, 317 (1971).

[20]D. Haidt, "Neutrino Results from Gargamelle", 1977 International Symposium on Lepton and Photon Interactions at High Energies.

[21]J. Campbell, et al., Phys. Rev. Lett. 30, 335 (1973); S. J. Barish, et al., Phys. Rev. Lett.

[22]J. Blietschau, et al., Nucl. Phys. B114, 189 (1976) and references therein.

[23]F. Reines, H. S. Gurr and H. W. Sobel, Phys. Rev. Lett. 37, 315 (1976).

[24]B. W. Lee and R. Shrock, Fermilab PUB-77/48-THY, June 1977.

[25]A. De Rújula, H. Georgi and S. L. Glashow, HUTP-77/A002, January 1977.

[26]S. J. Barish, et al., ANL-HEP-PR-76-69, to be published in Phys. Rev.

[27]W. Lee, et al., Phys. Rev. Lett. 37, 186 (1976).

[28]S. Bonetti, et al., IL Nuovo Cimento 38A, 260 (1977).

FIGURE CAPTIONS

Figure 1: Front and side view of the proposed neutrino target detector in front of existing Lab C muon spectrometer.

Figure 2: Sub-module of new detector consisting of plastic flash chambers alternated with 1 cm fiber reinforced cement and 0.6 cm aluminum.

Figure 3: Full module of new detector consisting of three sub-modules (Fig. 4) plus 0.6 cm Pb and a layer of proportional tubes.

Figure 4: The Lab C muon spectrometer, with the two proportional tube hodoscope detector planes.

Figure 5: Detail of the proportional tube construction. Also shown is the observed pulse height distribution obtained from a prototype detector using an Fe^{55} source.

Figure 6: Kinematics for the Fermilab narrow band neutrino beam (see Ref. 11). For given neutrino energies, the hadron energy, E_H, is plotted vs. the angle of the hadron shower, Θ_H.

Figure 7: Neutrino energy and $y_{min} = E_{\nu\pi}/E_{\nu K}$ are plotted vs. the radial distance from the center of the neutrino beam for incident neutrinos and antinuetrinos.

Figure 8: The simulated x distribution for all $y \leq 0.8$ for narrow band neutrino neutral current events. The error bars represent the statistical errors.

Figure 9: The simulated x-distribution for narrow band antineutrino neutral current events. A cut in $y \leq 0.8$ was made.

Figure 10: The simulated y-distribution for all x for narrow band neutrino neutral current events.

Figure 11: The simulated y-distribution for all x for narrow band anti-neutrino neutral current events.

Figure 12: $p_\perp$ distributions of the outgoing electron for $\nu_{\mu e}$ elastic scattering and neutron inverse beta decay (with and without Pauli suppression). The number of events is for 6×10^{18} 400 GeV protons on target, the two-horn neutrino beam and a 360 ton fiducial volume in this detector.

Figure 13: Energy distributions of the outgoing electrons in $\nu_\mu e^-$ elastic scattering and neutron inverse beta-decay.

Figure 14: $p_\perp$ distributions as in Fig. 2 , but with experimental resolutions included.

Figure 15: Kinetic energy distribution of the outgoing proton for neutron inverse beta decay (with and without Pauli suppression).

Figure 16: Regions in the (g_V, g_A) plane allowed by the Gargamelle data on the reactions $\nu_\mu e \to \nu_\mu e$ and $\bar{\nu}_\mu e \to \bar{\nu}_\mu e$. The outer contours are 90% confidence level limits.

Figure 17: Regions in the (g_V, g_A) plane allowed by Reines, et al. The two different elliptical regions correspond to the two bins 1.5-3.0 MeV and 3.0-4.5 MeV in scattered electron lab energy.

Figure 18: Regions in the (g_V, g_A) plane allowed in this experiment assuming the Weinberg-Salam model with $\sin^2\theta_W = 0.35$. This assumes 10% statistical error and 20% systematic error

Figure 19: The measured trigger efficiency for electrons and hadrons is plotted versus energy.

Figure 20: The numbers of equivalent minimum ionizing particles versus shower depth for various hadron energies.

Fig. 1

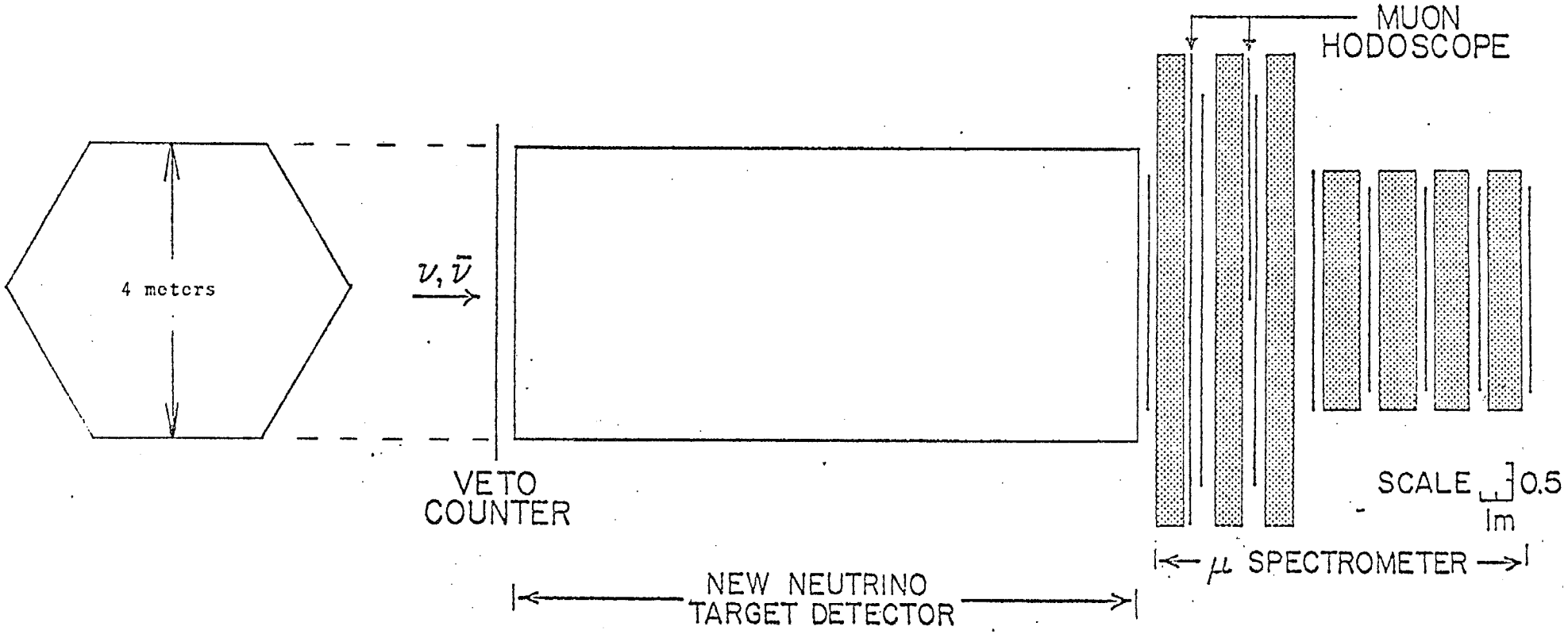
MUON
HODOSCOPE
4 meters
$\nu, \bar{\nu}$
VETO
COUNTER
SCALE
0.5
1m
μ SPECTROMETER
NEW NEUTRINO
TARGET DETECTOR

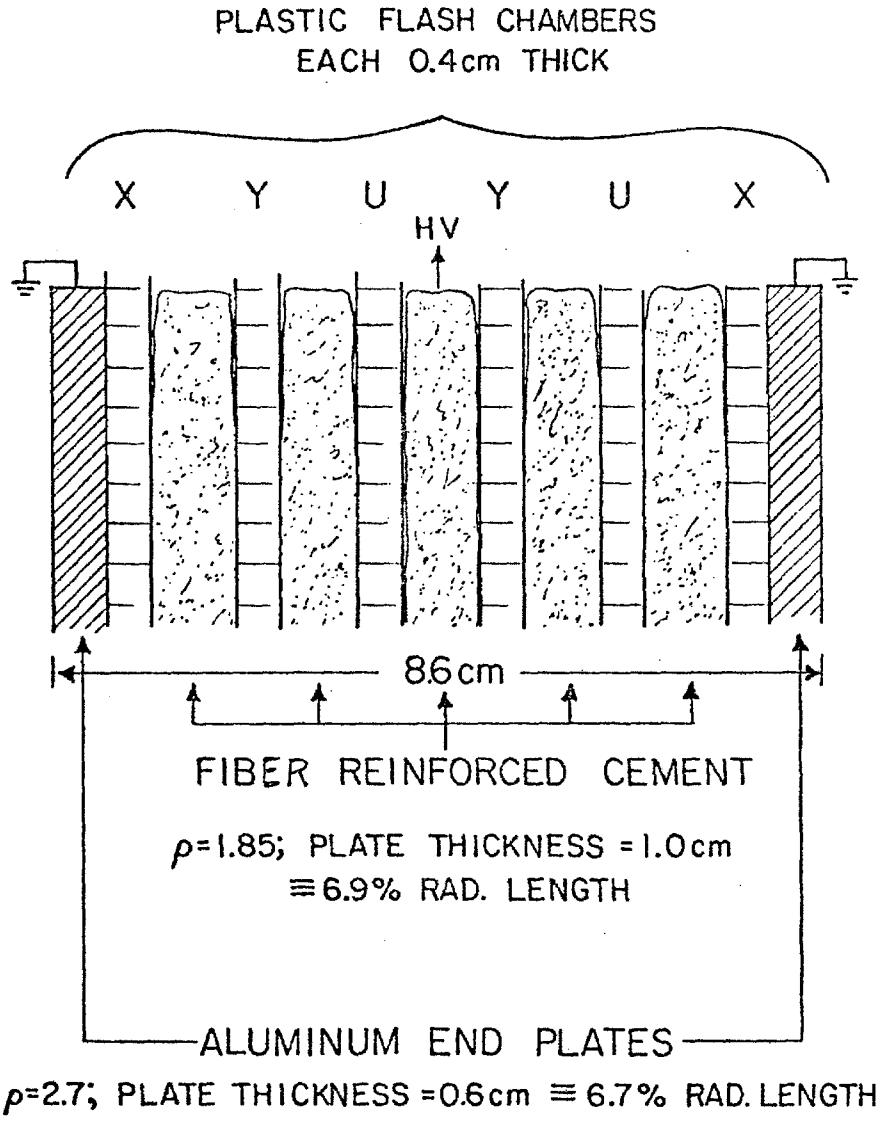

ONE SUB-MODULE OF DETECTOR

Fig. 2

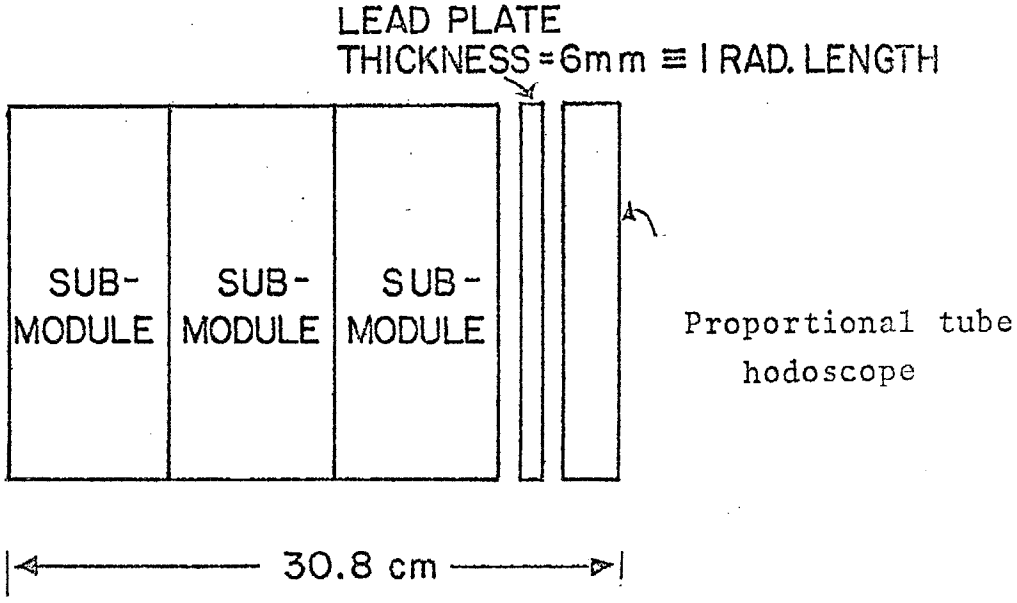

ONE MODULE OF DETECTOR

Fig. 3

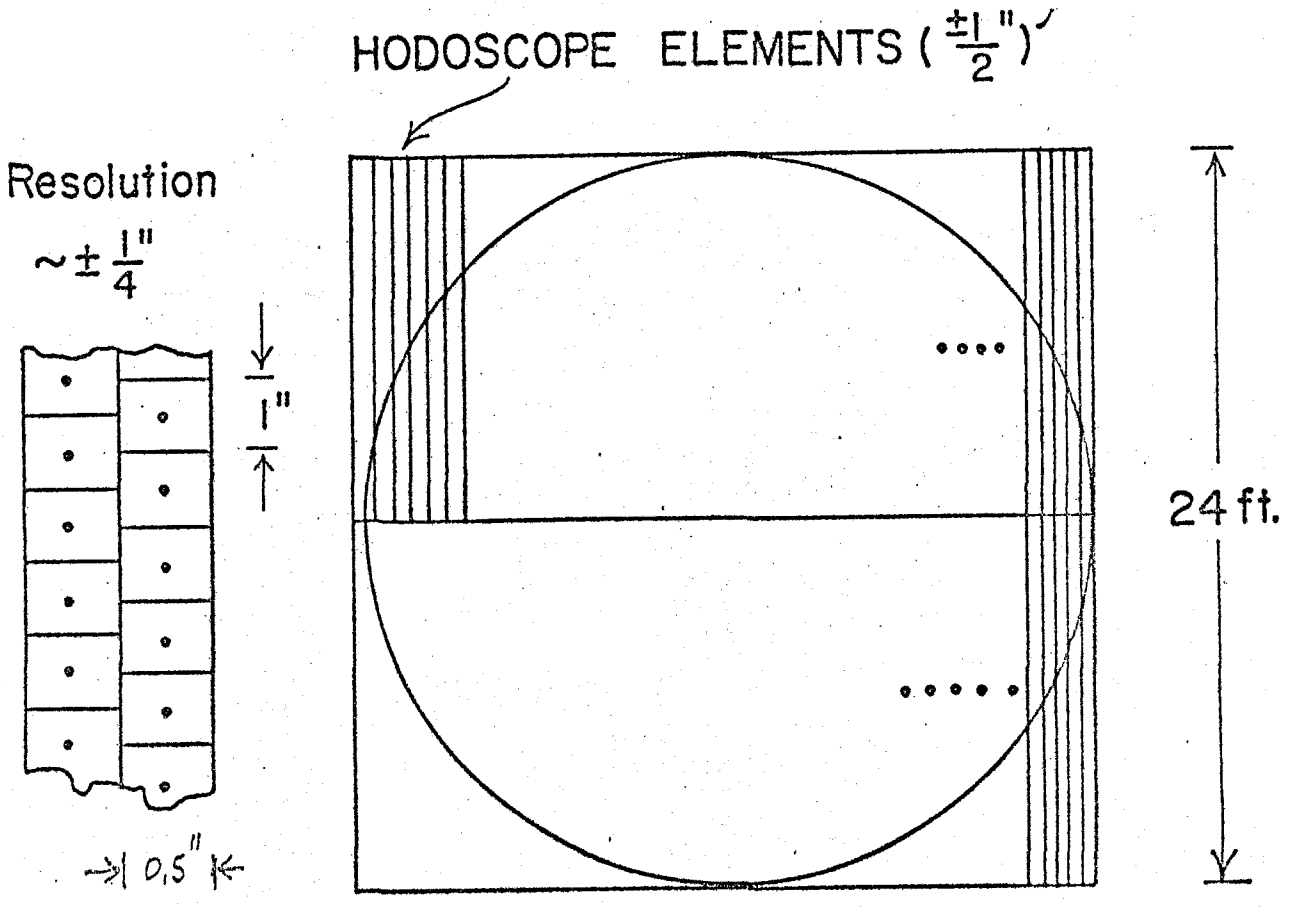

576 Wires / Plane — 2 Planes Total = 1152

Fig. 4

CONSTRUCTION OF PROPORTIONAL TUBES

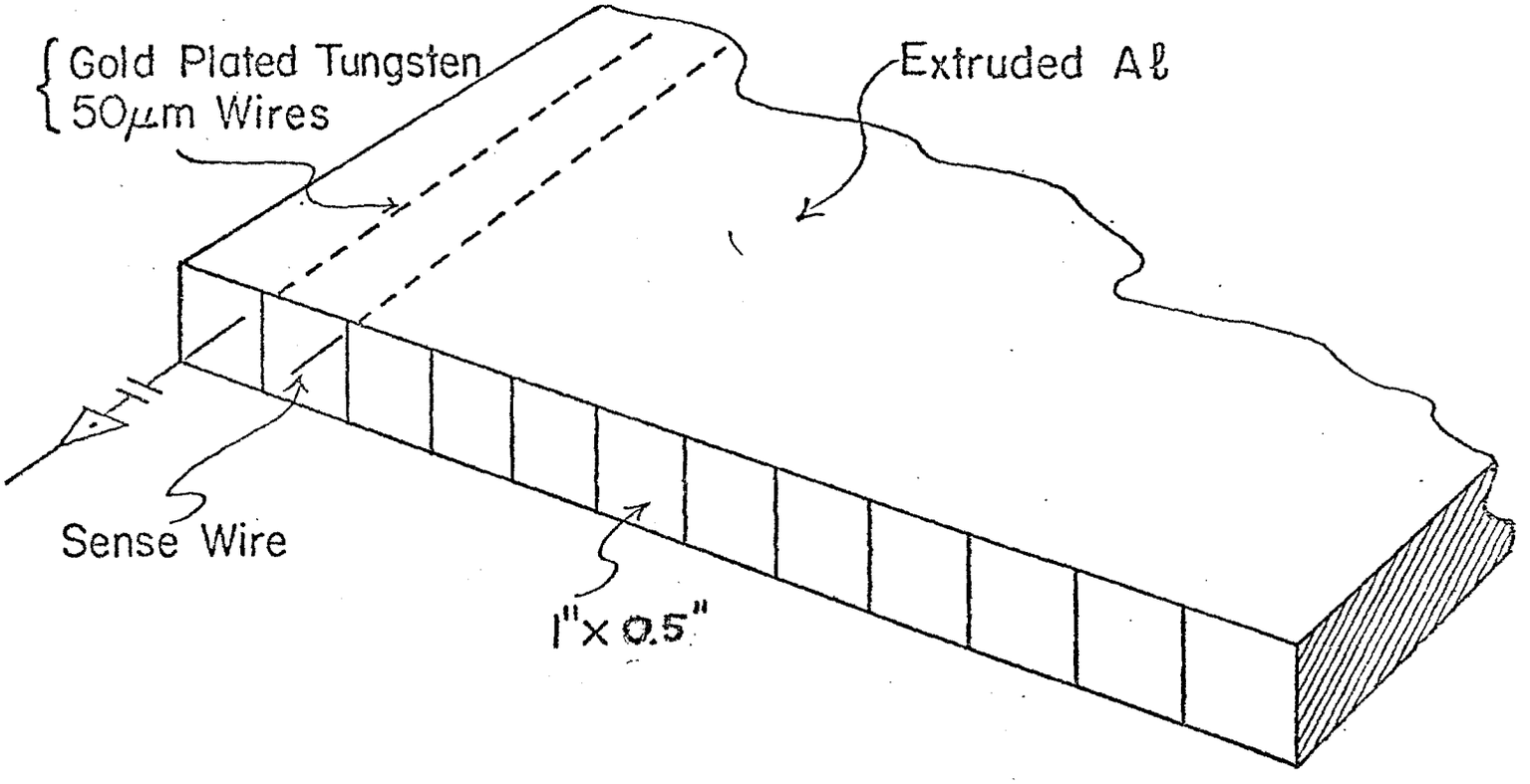

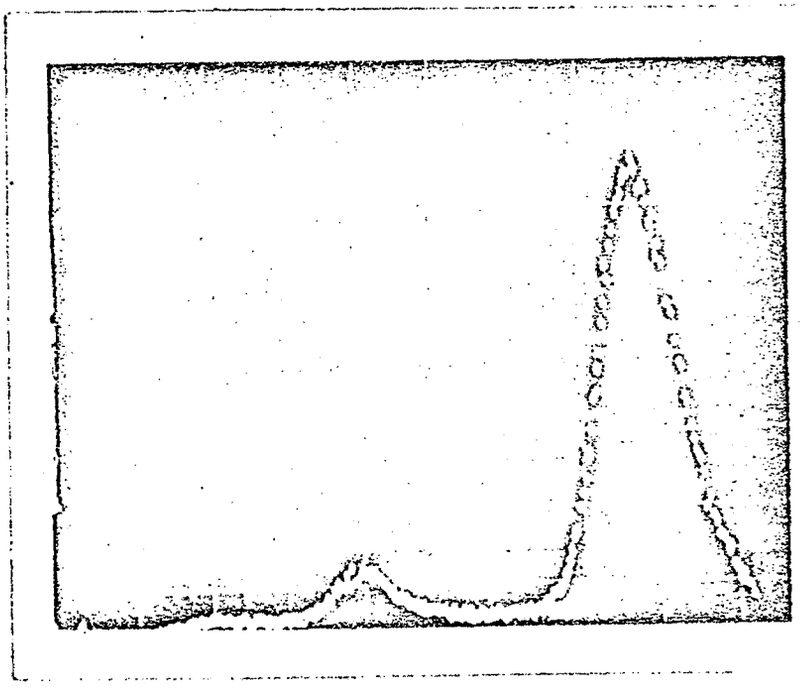

OBSERVED PULSE HT DISTRIBUTION
USING F_e 55 SOURCE

Fig. 5

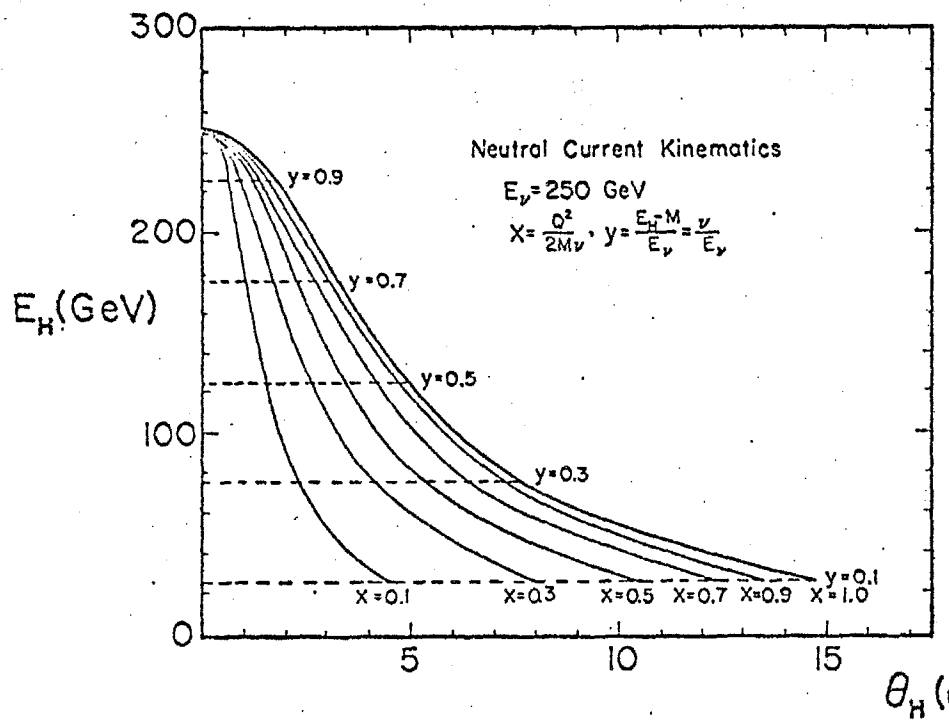
Neutral Current Kinematics
E_ν = 250 GeV
$X = \frac{Q^2}{2M\nu}$, $y = \frac{E_H - M}{E_\nu} = \frac{\nu}{E_\nu}$
E_H (GeV)
θ_H (degrees)
y = 0.9
y = 0.7
y = 0.5
y = 0.3
y = 0.1
X = 0.1
X = 0.3
X = 0.5
X = 0.7
X = 0.9
X = 1.0
300
200
100
0
5
10
15

Fig. 6a

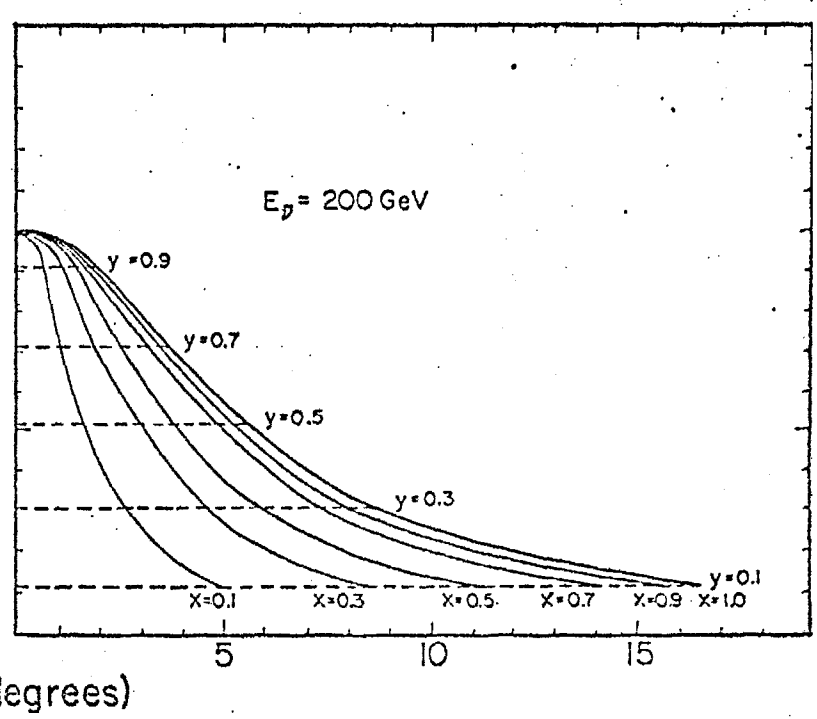
E_p = 200 GeV
y = 0.9
y = 0.7
y = 0.5
y = 0.3
y = 0.1
X = 0.1
X = 0.3
X = 0.5
X = 0.7
X = 0.9
X = 1.0
5
10
15

Fig. 6b

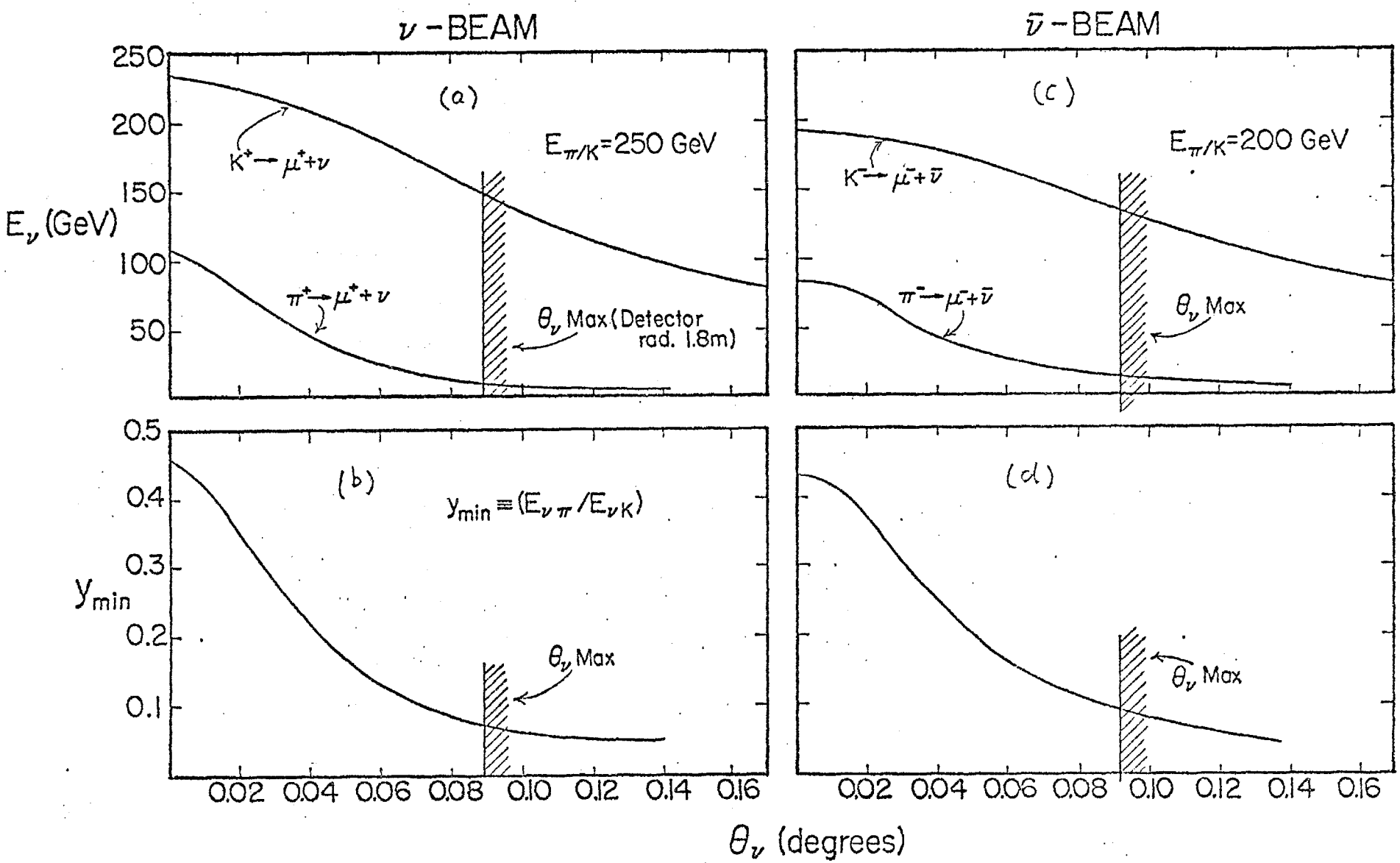
ν -BEAM
$\bar{\nu}$ -BEAM
(a)
(c)
(b)
(d)
$E_{\pi/K}$=250 GeV
$E_{\pi/K}$=200 GeV
$K^+ \rightarrow \mu^+ + \nu$
$K^- \rightarrow \mu^- + \bar{\nu}$
$\pi^+ \rightarrow \mu^+ + \nu$
$\pi^- \rightarrow \mu^- + \bar{\nu}$
θ_ν Max (Detector rad. 1.8m)
θ_ν Max
$y_{min} \equiv (E_{\nu\pi}/E_{\nu K})$
E_ν (GeV)
y_{min}
θ_ν (degrees)
250
200
150
100
50
0.5
0.4
0.3
0.2
0.1
0.02 0.04 0.06 0.08 0.10 0.12 0.14 0.16

FIG. 7

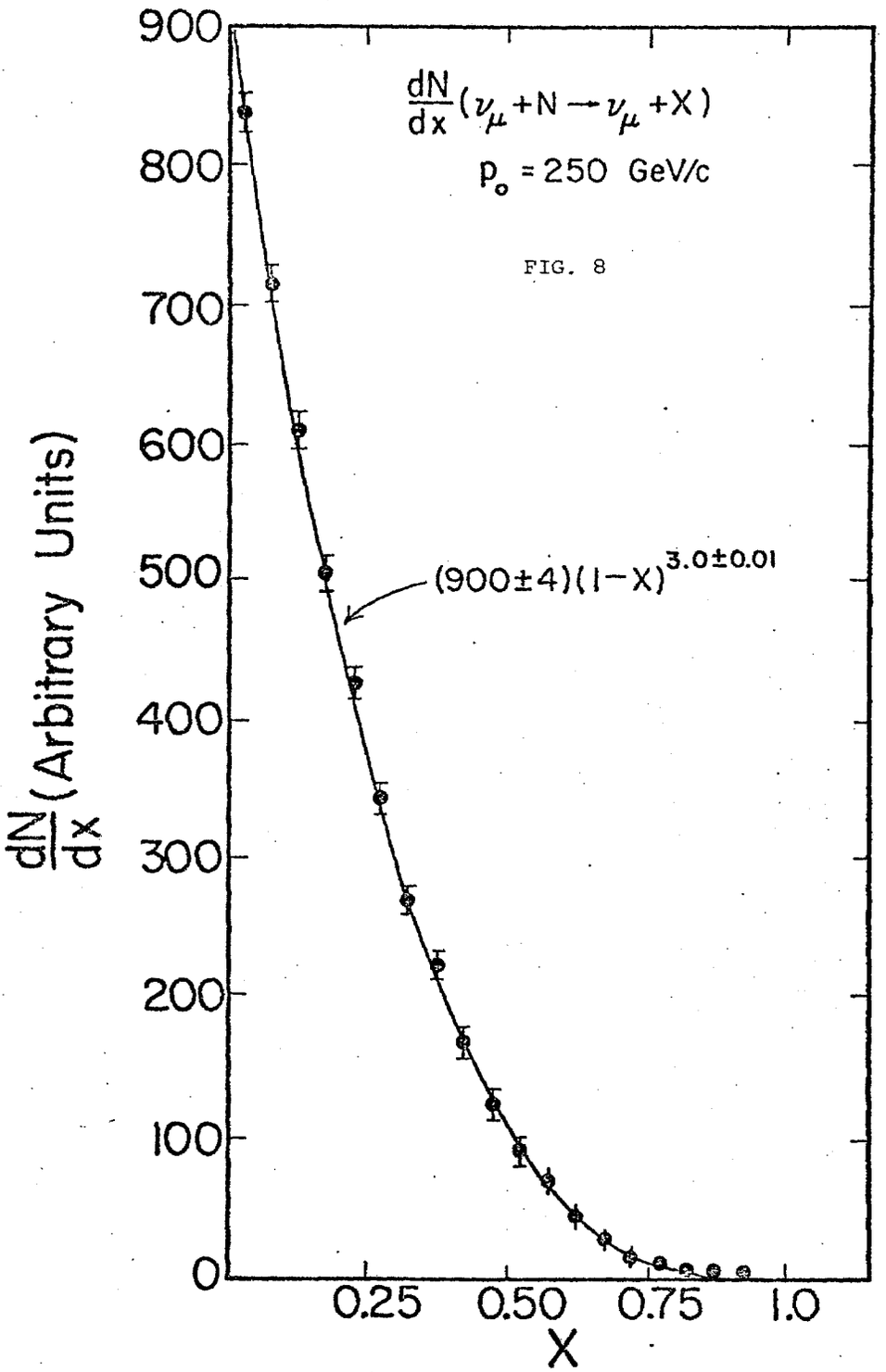
$\frac{dN}{dx}(\nu_\mu + N \rightarrow \nu_\mu + X)$
$p_o = 250$ GeV/c
$(900 \pm 4)(1-X)^{3.0 \pm 0.01}$
$\frac{dN}{dx}$ (Arbitrary Units)
X
900
800
700
600
500
400
300
200
100
0
0.25
0.50
0.75
1.0

FIG. 8

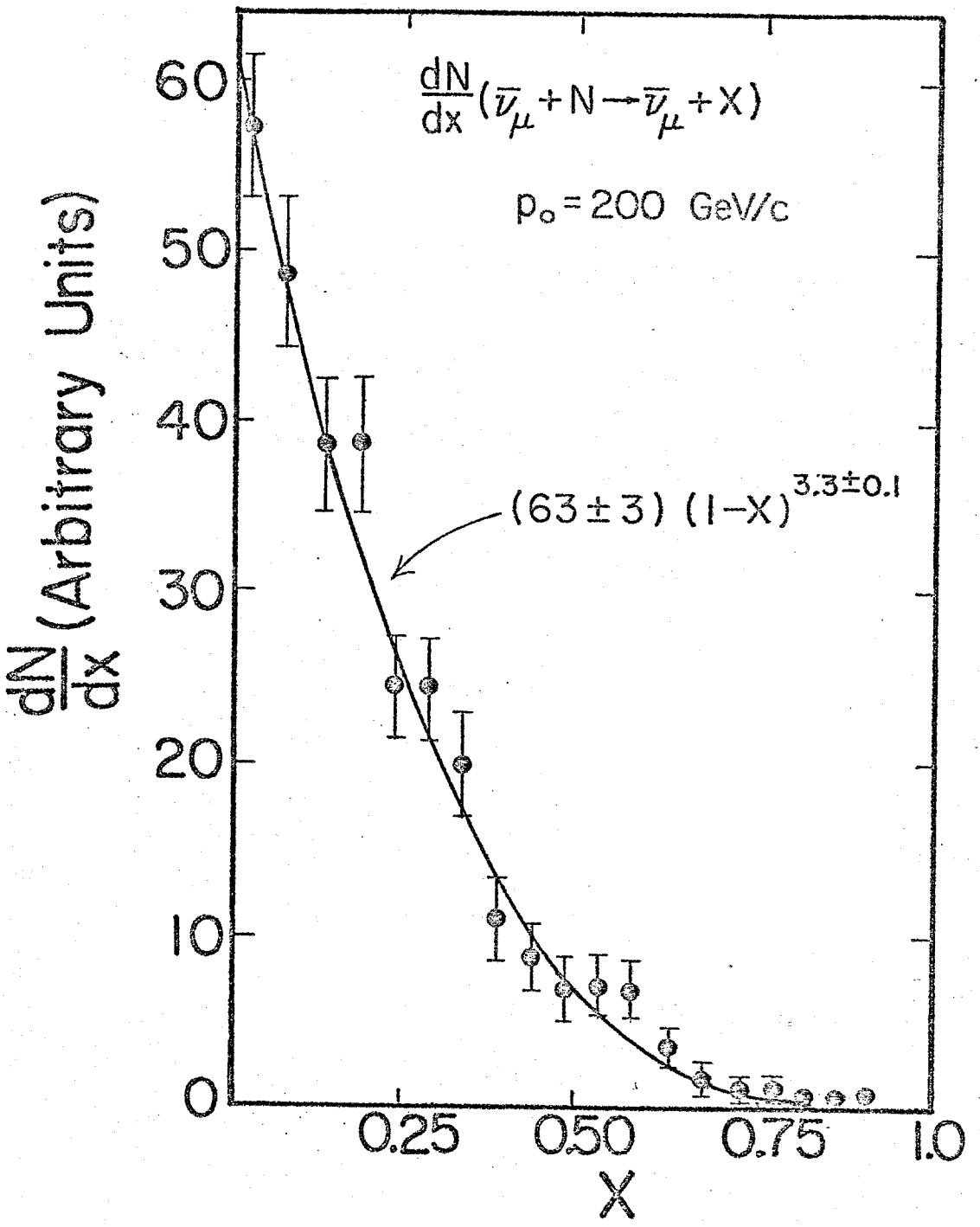
$\frac{dN}{dx}(\bar{\nu}_\mu + N \rightarrow \bar{\nu}_\mu + X)$
$p_o = 200$ GeV/c
$(63 \pm 3)(1-X)^{3.3\pm0.1}$
$\frac{dN}{dx}$ (Arbitrary Units)
60
50
40
30
20
10
0
0.25
0.50
0.75
1.0
X

FIG. 9

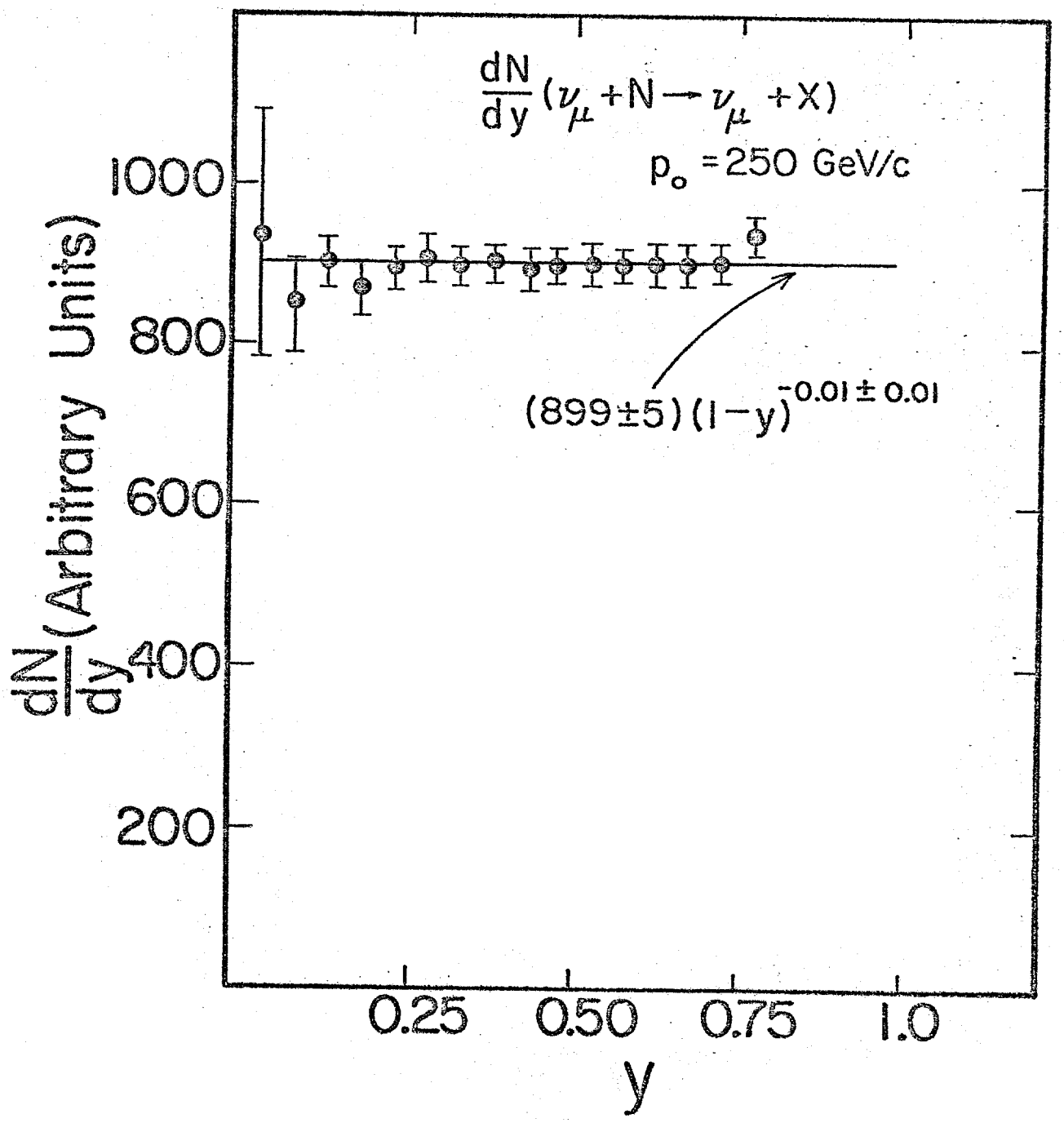
$\frac{dN}{dy}(\nu_\mu + N \rightarrow \nu_\mu + X)$
$p_o = 250$ GeV/c
$(899 \pm 5)(1-y)^{-0.01 \pm 0.01}$
$\frac{dN}{dy}$ (Arbitrary Units)
1000
800
600
400
200
0.25
0.50
0.75
1.0
y

FIG. 10

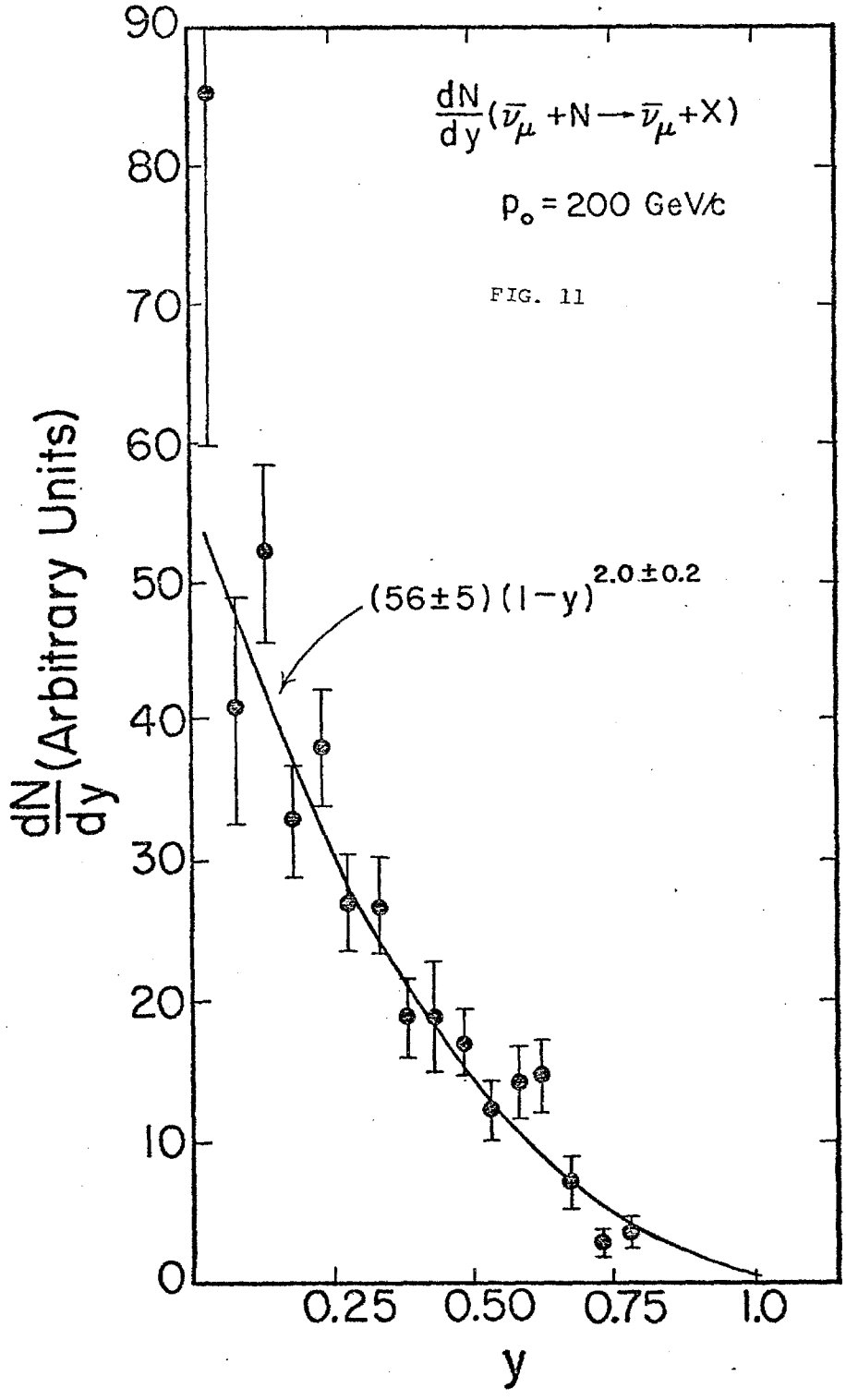
$\frac{dN}{dy}(\bar{\nu}_\mu + N \rightarrow \bar{\nu}_\mu + X)$
$p_o = 200$ GeV/c
$(56 \pm 5)(1-y)^{2.0 \pm 0.2}$
$\frac{dN}{dy}$(Arbitrary Units)
y
0
10
20
30
40
50
60
70
80
90
0.25
0.50
0.75
1.0

FIG. 11

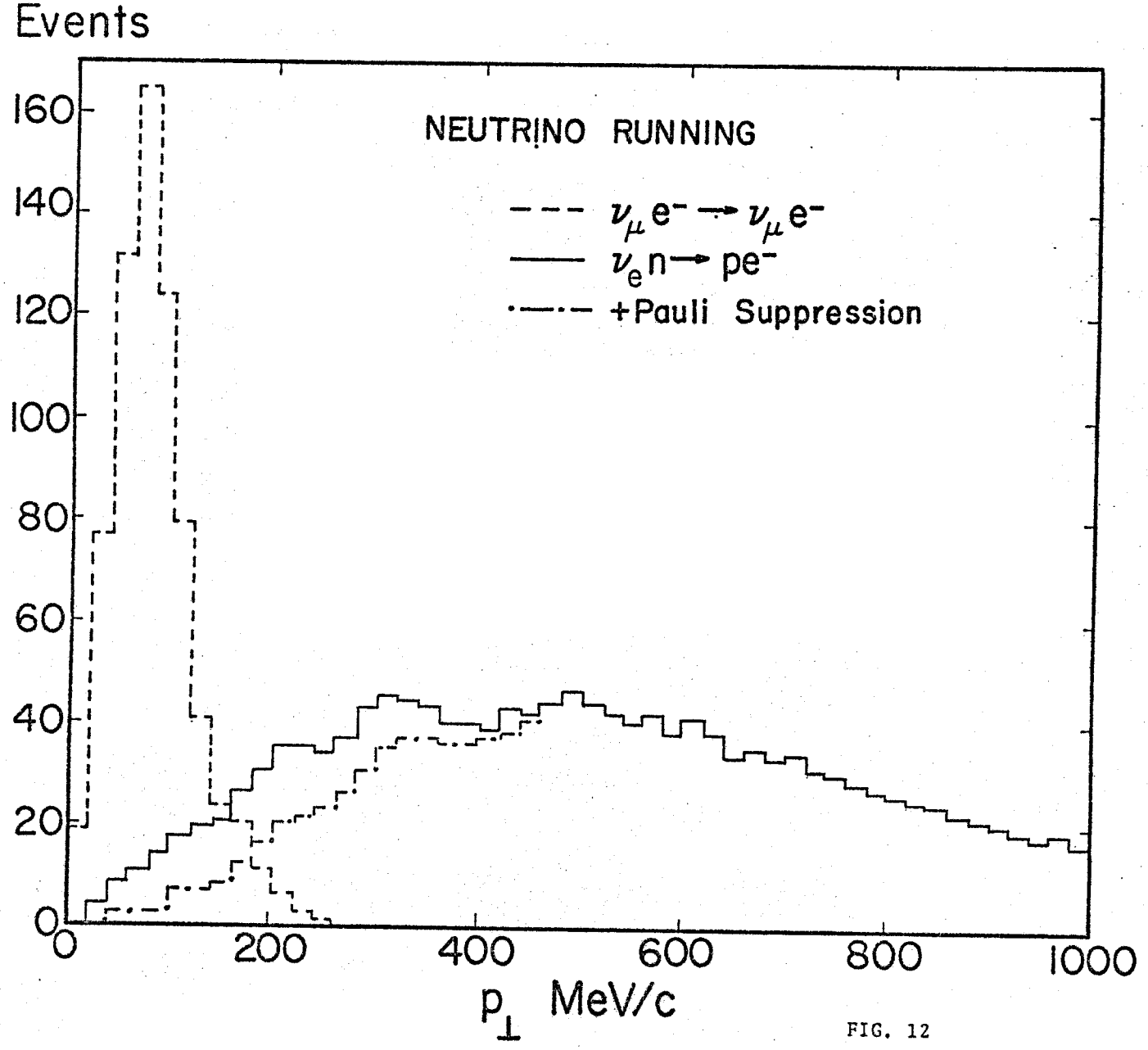
Events
NEUTRINO RUNNING
$\nu_\mu e^- \rightarrow \nu_\mu e^-$
$\nu_e n \rightarrow p e^-$
+Pauli Suppression
160
140
120
100
80
60
40
20
0
0
200
400
600
800
1000
$p_\perp$ MeV/c

FIG. 12

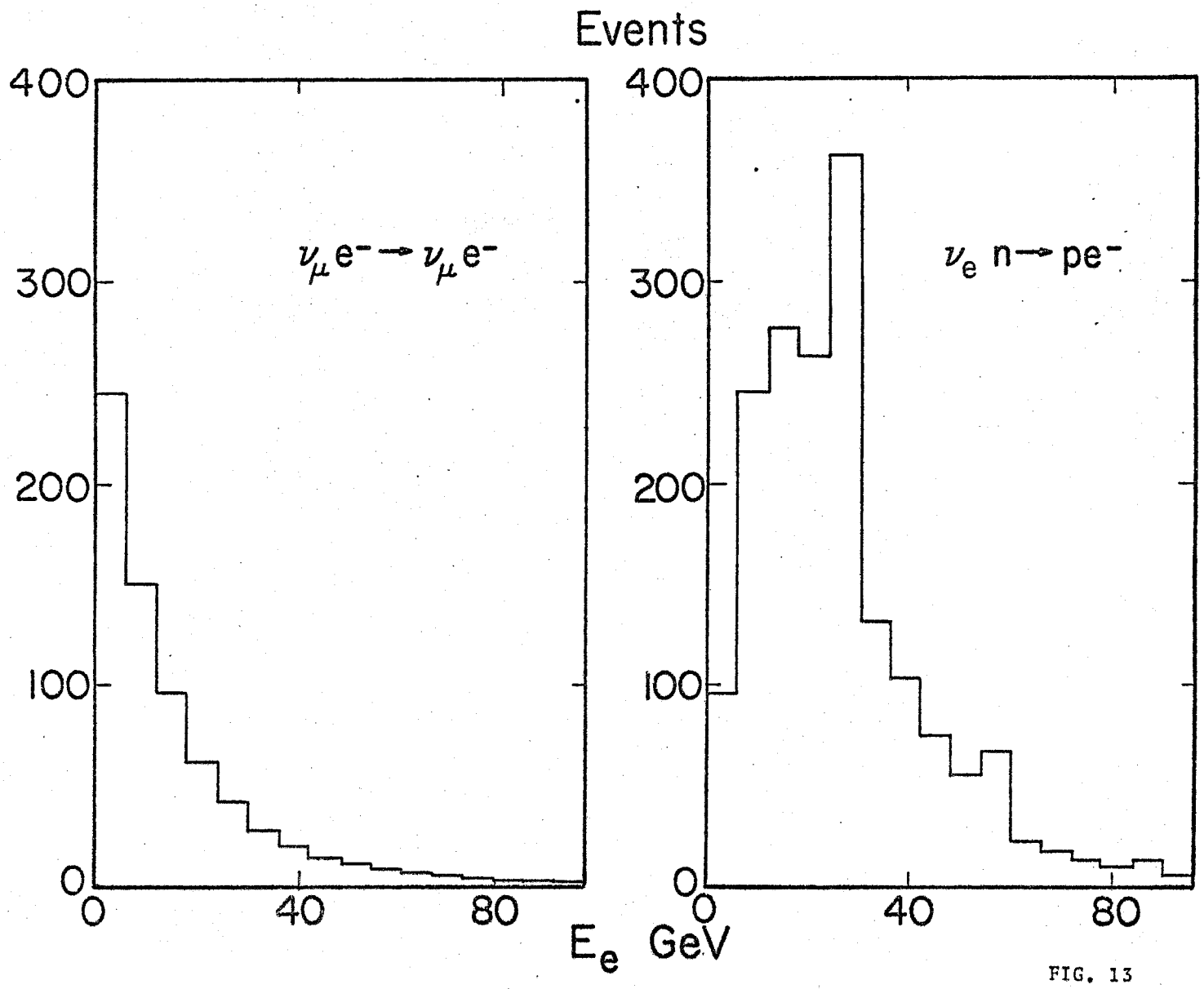
Events
400
300
200
100
0
$\nu_\mu e^- \rightarrow \nu_\mu e^-$
$\nu_e n \rightarrow pe^-$
0
40
80
E_e GeV

FIG. 13

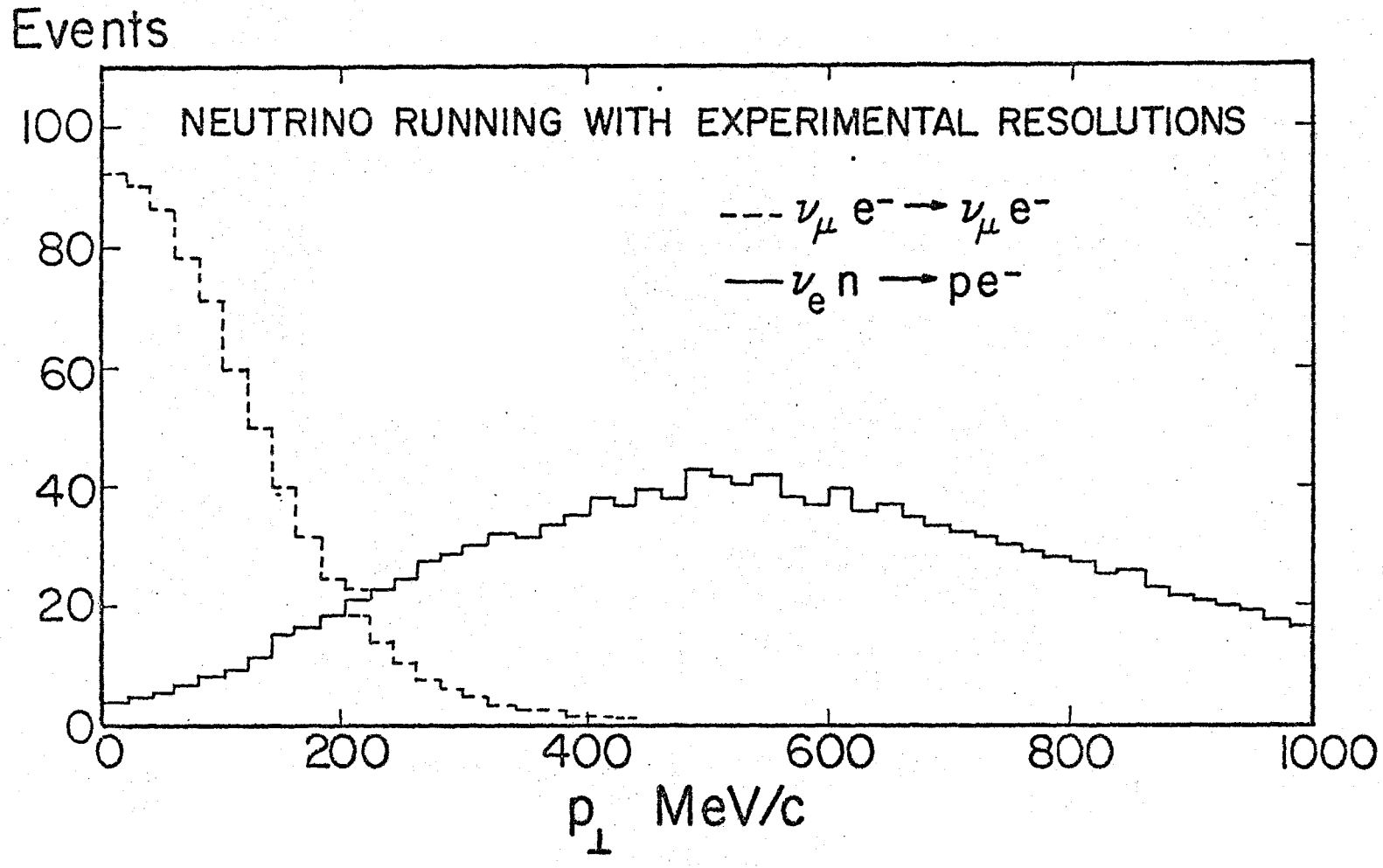
Events
NEUTRINO RUNNING WITH EXPERIMENTAL RESOLUTIONS
--- $\nu_\mu e^- \rightarrow \nu_\mu e^-$
— $\nu_e n \rightarrow p e^-$
100
80
60
40
20
0
0
200
400
600
800
1000
$p_\perp$ MeV/c

FIG. 14

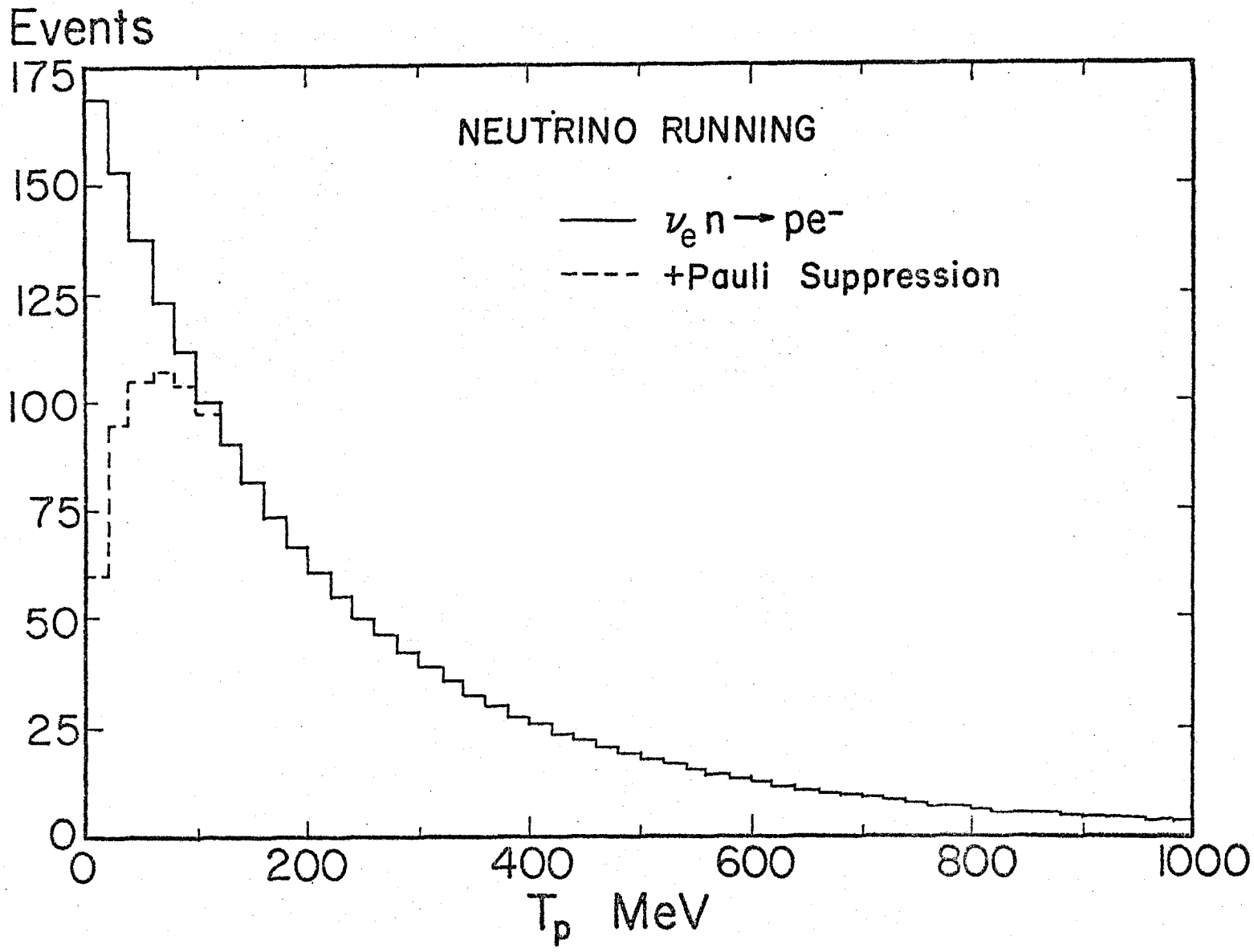
Events
175
150
125
100
75
50
25
0
NEUTRINO RUNNING
$\nu_e n \rightarrow pe^-$
+Pauli Suppression
0
200
400
600
800
1000
T_p MeV

FIG. 15

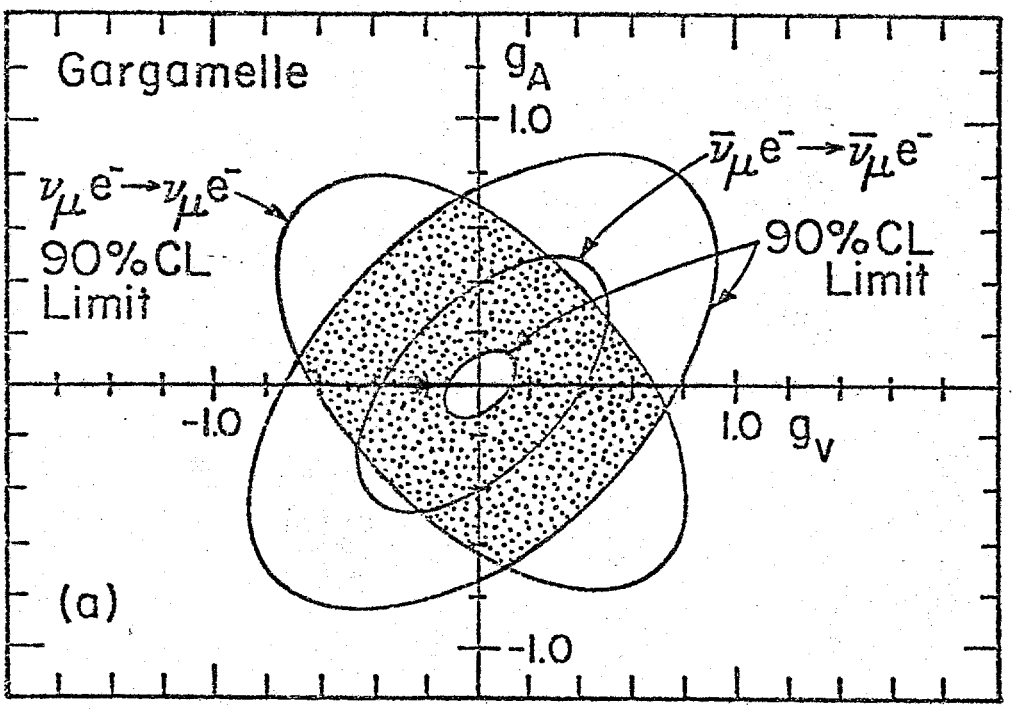
Gargamelle
g_A
1.0
$\bar{\nu}_\mu e^- \to \bar{\nu}_\mu e^-$
$\nu_\mu e^- \to \nu_\mu e^-$
90% CL
Limit
90% CL
Limit
-1.0
1.0 g_V
(a)
-1.0

Fig. 16

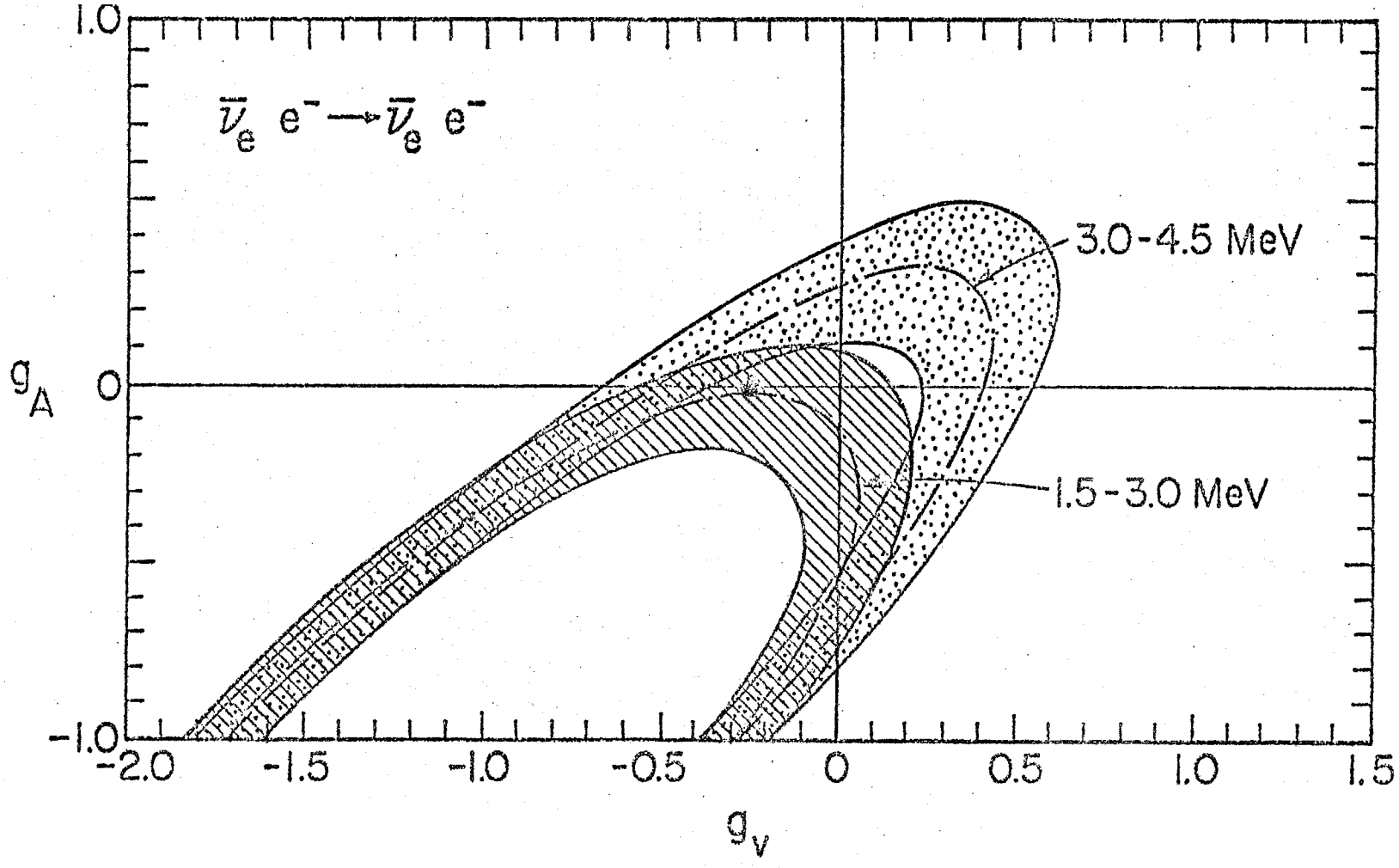
$\bar{\nu}_e\ e^- \rightarrow \bar{\nu}_e\ e^-$
3.0-4.5 MeV
1.5-3.0 MeV
g_A
g_V
1.0
0
-1.0
-2.0
-1.5
-1.0
-0.5
0
0.5
1.0
1.5

Fig. 17

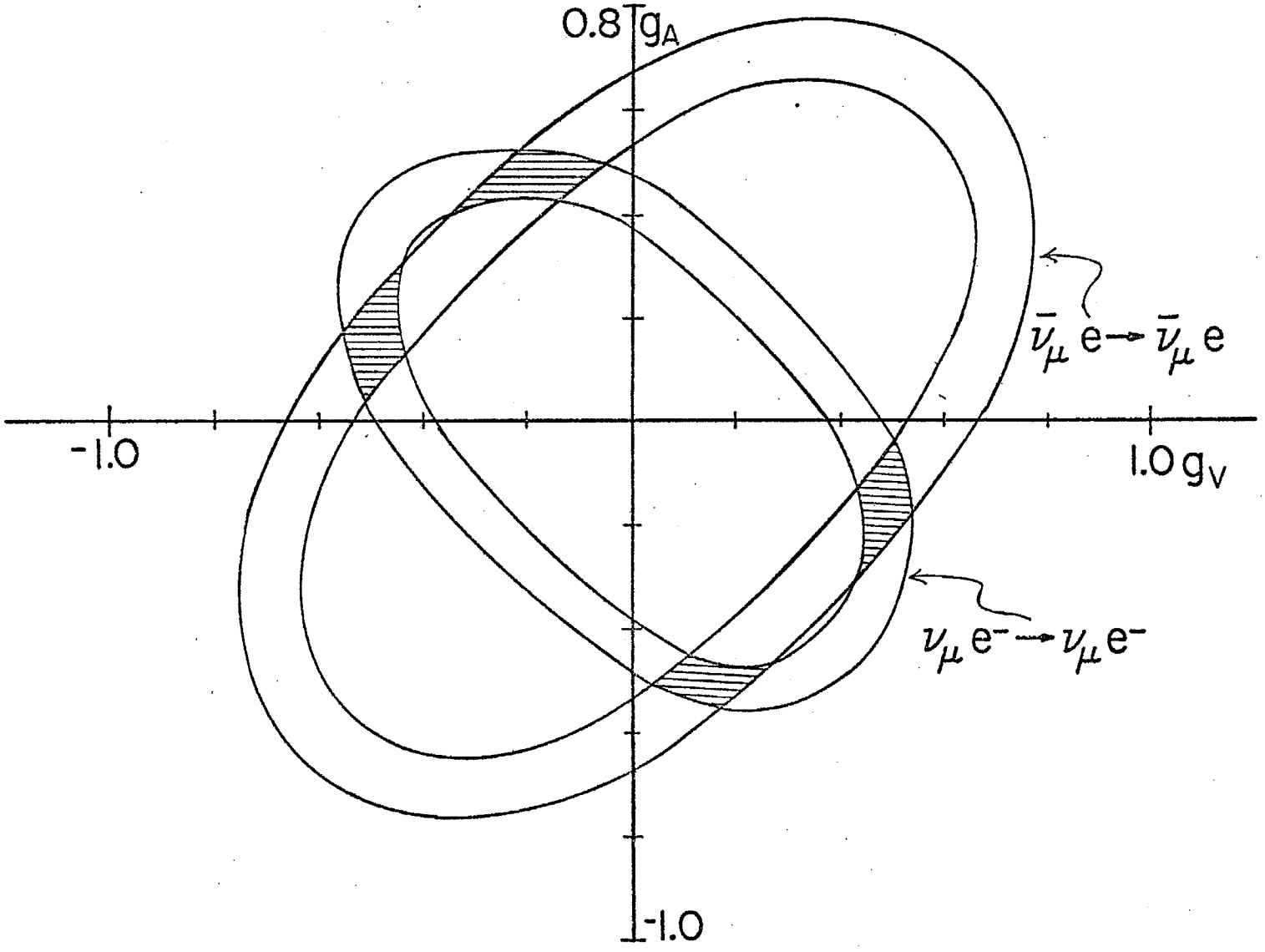
0.8 g_A
-1.0
1.0 g_V
-1.0
$\bar{\nu}_\mu e \rightarrow \bar{\nu}_\mu e$
$\nu_\mu e^- \rightarrow \nu_\mu e^-$

FIG. 18

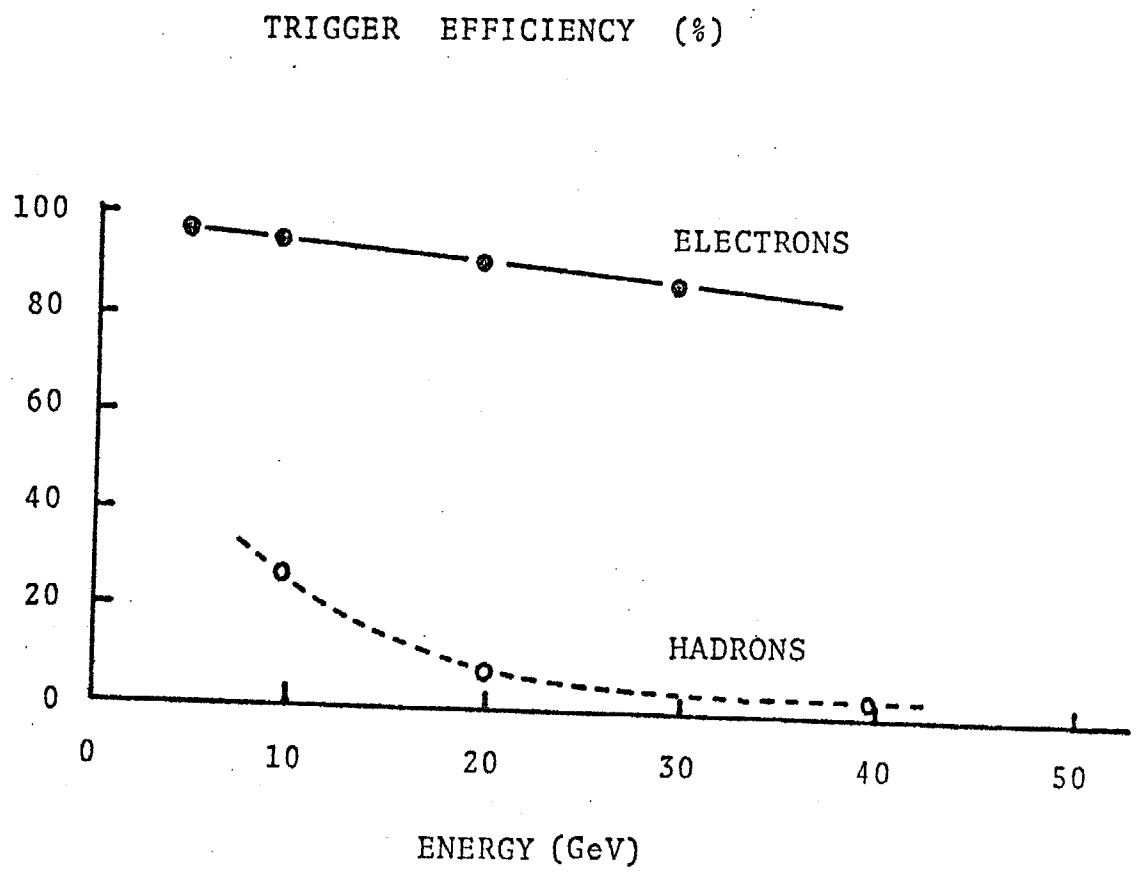
TRIGGER EFFICIENCY (%)
100
80
60
40
20
0
ELECTRONS
HADRONS
0
10
20
30
40
50
ENERGY (GeV)

Fig. 19

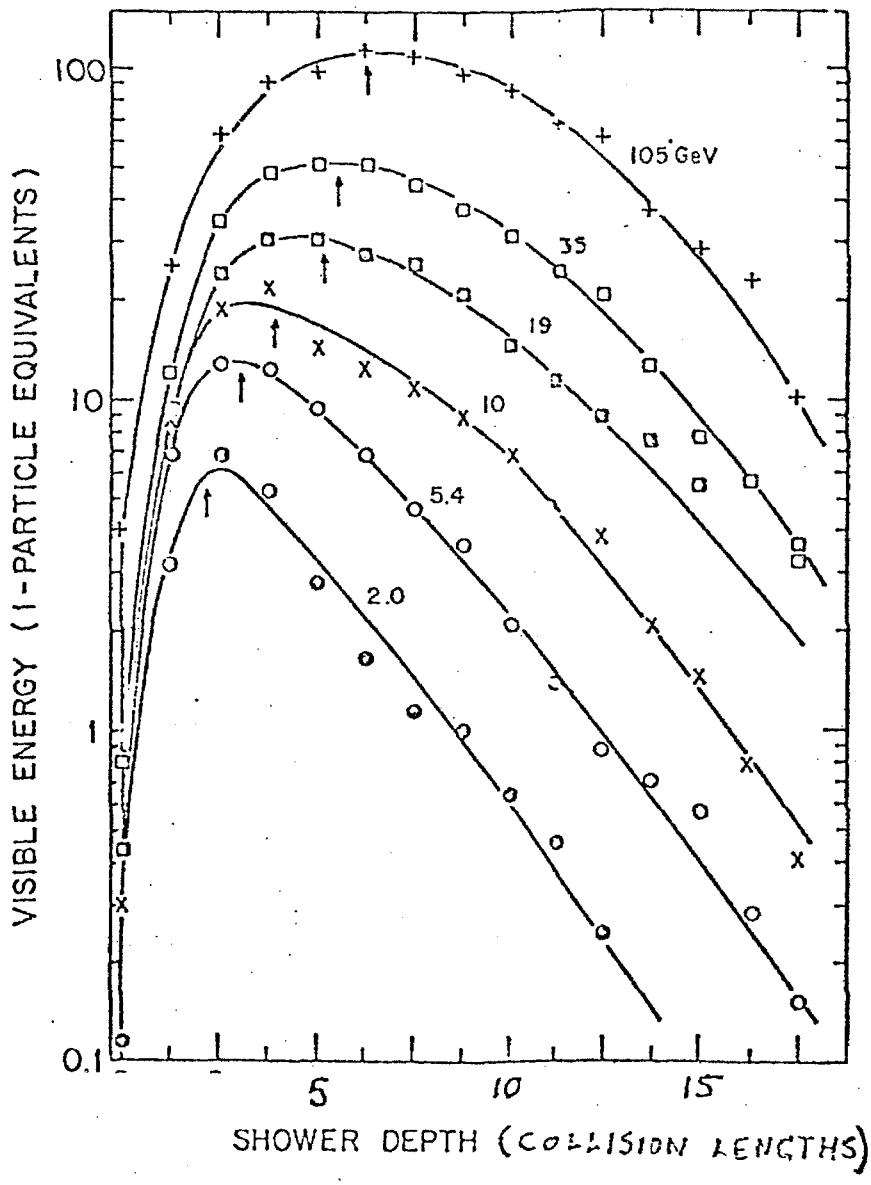
VISIBLE ENERGY (1-PARTICLE EQUIVALENTS)
100
10
1
0.1
5
10
15
SHOWER DEPTH (COLLISION LENGTHS)
105 GeV
35
19
10
5.4
2.0

Fig. 20

APPENDIX A

Detector Tests

I. Introduction

A test calorimeter of roughly 1/10 the linear scale of the proposed neutrino detector was constructed and tested in the Meson Lab M5 test beam and in the Neutrino Lab N3 beam. The M5 test beam furnished positive particles in the energy range of 5 to 40 GeV, and the N3 beam tests extended these measurements to 300 GeV. A summary of these tests is given in Table I. The M5 beam was composed of roughly 80% π^+, 20% p, and < 3% e^+. A 18m long gas Cerenkov counter provided a clean trigger on positrons. The N3 beam was roughly 60% π^+, 40%p, and < 1%e^+. Although this beam is equipped with cerenkov counters for particle identification, this capability has not been used to date.*

II. Construction of the Test Calorimeter

The test array consisted of 126 polypropylene planes 45cm x 45cm wide and 4mm thick with cells 4mm x 5mm. Every other polypropylene plane was fitted with a gas manifold to make a total of 63 operational flash chamber planes. A 5mm plate of lead and a 6.4mm thick scintillation counter were located every 20cm in the calorimeter. The total array had 15 radiation lengths and 3.5 collision lengths. The showers were sampled on the average every 24% of a radiation length and every 6% of a collision length.

*A summary of the M5 test beam results was presented at the Nuclear Science Symposium in "A Fine Grain Flash Chamber Calorimeter" by F.E. Taylor, T. Ohsugi, J.K. Walker, D. Buchholz, and D. Miller, to be published in Proceedings IEEE Nuclear Science Symposium, February, 1978.

The average density of the calorimeter was 1.7g/cm^3. The photograph shows the calorimeter layout (See Figure 1a).

The flash chambers were made from black polypropylene sheets available at a cost of $1.5/square meter. The polypropylene sheets were made by an extrusion process with a cell size of 4mm x 5mm. The cells were filled with standard Ne (90%) -He (10%) spark chamber gas mixture. Transparent gas manifolds were made from thermo-vacuum formed plastic and glued to the ends of the polypropylene sheets to form a gas tight chamber (Figure 1b). A triggered HV pulse of approximately 8KV, 100 nsec duration was applied across the 4mm thick chambers thereby causing a glow discharge in the Ne + He gas which propagates and fills the entire cell where the ionizing particle traversed the chamber. This glow discharge was easily photographed using an 80mm -f2.8 lens with 35mm SO143 film.

III. Electrical Characteristics

The main electrical characteristics of the flash chambers are: 1) each flash chamber cell is electrically insulated from each other cell, and 2) there is no D.C. path of stored energy of the triggered HV pulse through the chamber to ground. In other words, the region where the glow discharge takes place is insulated from the HV electrodes. Hence, the flash chamber is capable of detecting many tracks in a given event since there is little energy "robbing".

The glow discharge, which propagates and fills the cell traversed by the particle, is initiated by a triggered HV pulse. This HV pulse is applied across the 4mm dimension of the polypropylene sheets and is generated by a conventional spark gap capacitor discharge circuit.

We have experimented with various time constants of the HV pulse. We found that the best chamber operation is achieved for $\tau \sim 100$ nsec. In the early design of the flash chambers used in the test calorimeter, we found that for time constants longer than 200 nsec, adjacent cells begin to fire, spoiling the angular and energy resolution of the calorimeter. Later design efforts have completely eliminated this defect by cutting back the electric field electrodes 6" from the gas manifold of the flash chamber planes. Now. longer time high voltage pulses ($\tau \leq 600$ nsec) may be applied, giving brighter flashes without adjacent cells firing.

In Figure 2 we have plotted a typical HV plateau curve for a flash chamber in the test calorimeter. These data were taken by using 10 GeV muons supplied by the M5 test beam at Fermilab. The event rate was determined by the camera film transport which allowed only 1 trigger every beam spill, hence 1 event every 15 seconds. We see that the chamber plateaus at roughly 8 kV ($E \approx 20$kV/cm) at an 80% single track efficiency. We expect the multitrack efficiency to be essentially the same as the single track efficiency since there is little energy robbing. We have observed tracks with good efficiency up to 80° to the normal.

We have measured the flash chamber sensitivity time by

inserting delay in the trigger pulse to the master spark gap. In Figure 3, we have plotted the chamber efficiency as a function of this delay. We see that the chamber efficiency drops roughly linearly by 20% out to $\sim$ 1 μsec delay. In addition, we have found that the sensitive time is a function of the Ne + He gas flow rate. In the data of Figure 3, the flow rate was 1.5% of the chamber gas volume/min. We have experimented with other flow rates and find that shorter sensitive times can be achieved by reducing the gas flow rate. The chamber recovery time after pulsing is $\sim$100 msec. However, no clearing field was used which can shorten this time.*

IV. Performance

The response of the test calorimeter to positrons and positive hadrons has been measured in the energy range of 5 to 40 GeV. A set of typical electromagnetic showers is shown in Figure 4a and typical hadron showers are shown in Figure 4b. It is apparent from Figure 4 that the multi-track efficiency is high and that there is little track "robbing". Furthermore, the track efficiency appears to be independent of the angle of traversal through the polypropylene cells. In fact we have observed tracks with good efficiency at up to 80 degrees to the normal.

*This recovery time may be reduced to $\lesssim$ 10 millisec. by mixing a small amount of electronegative gas (CH_4) with the Ne + He mixture. See J.E. Chaney, et. al., Nucl Inst. and Methods, 124, 161 (1975).

1. Positrons

a. The Energy Response

The number of cells which fire at a given electromagnetic shower depth for various incident energies is shown in Figure 5. This figure shows the increase of the number of cells with increasing incident energy as well as the slow increase in the depth at the shower maximum. The average total number of cells versus the energy of the incident electron is shown in Figure 6. We find the energy response to be roughly linear up to 20 GeV. For electron energies above 20 GeV the number of electron-positron pairs at the shower maximum is too large to distinguish individual particles with the cell size of 4mm x 5mm, and thus the energy response of the calorimeter becomes nonlinear. Even with this non-linear energy response above 20 GeV, useful measurements may be made up to 40 GeV.

b. Electron Energy Resolution

In Figure 7 we show a histogram of the number of cells which fire for incident electrons of 20 GeV. A gaussian adequately fits the data with σ/mean $\approx$ 5.5%. The electron energy resolution is then computed by accounting for the non-linear energy response shown in Figure 6.

The energy resolution versus the incident electron energy is shown in Figure 8. We see that the energy resolution is roughly constant and is given

by $\sigma(E)/E \tilde{\sim} 10\%$ for $5 \leq E_e \leq 40$ GeV. The proposed calorimeter will have a sampling every 14% of X_o instead of every 24% of X_o and, hence, perhaps the energy resolution will improve somewhat. We do not require this improvement however.

c. Electron Angular Resolution

The electron angular resolution of the calorimeter has been determined by digitizing the x-y coordinates of every firing cell in a sample of electromagnetic shower events. (x is perpendicular to the incident electron direction, y is parallel to this direction.) From these coordinates we have computed the lateral position (x) of the center of gravity of the firing cells for a given shower depth (y). In Figure 9a we show the center of gravity coordinates of a typical 30 GeV electromagnetic shower. (The x-y coordinates in Figure 9 are in arbitrary units.) The central axis of the shower is quite evident, but we notice a considerable scattering of the center of gravity positions about the central axis due to the statistical nature of the shower.

Careful treatment of these shower fluctuations is necessary to obtain good angular resolution. Hence, we have adopted a two pass fitting procedure to determine the shower direction. In the first pass, a straight line is fitted to the center of gravity of the data by assigning equal weights to each center of gravity coordinate. The first pass fit is shown by the solid line in Figure 9a.

The first pass fit is then used to define a "road" to cut out data which show large fluctuations about the first pass line. This road is made narrow at the front end of the shower and linearily broadens as the beam direction coordinate (y) is increased. The space between the dashed lines in Figure 9a is the road. This recipe accounts for the expected increase in the lateral fluctuations of the shower as the shower depth is increased but eliminates spurious fluctuations. Typically $\lesssim$ 10% of the coordinate data for a given event are eliminated by this cut. The surviving data are then refit, but this time the coordinates at the beginning of the shower are weighted more heavily than the coordinates at the end of the shower. This differential weighting is performed by allowing the uncertainty of each center of gravity coordinate to increase linearily with increasing y. This second pass fit of the event of Figure 9a is shown in Figure 9b.

In Figure 10 we show the resulting electron projected angle resolution determined by this two pass procedure for $5 \leq E_e \leq 30$ GeV. We see that the electron angular resolution decreases with increasing energy and can be described by $\sigma(E_e) = (2 + 70/E_e$ (GeV)) mrad. For comparison we show the angular resolution for 10 GeV muons. The data suggest that in the high energy limit, the angular resolution of electrons approaches that of muons. We have also shown on Figure 10 the angle

resolution obtained by Baltay for the three clean neutrino elastic scattering events observed in the 15' Ne filled B.C. The two resolutions are comparable.

We may also compare the electron energy resolutions in the two cases. We show in the table below the energies and resolutions of the same three events observed in the B.C. compared to the measured resolutions in the proposed detector.

E_e(GeV)	Resolution σ(GeV)	Resolution in Proposed Detector σ(GeV)
9	$\pm$ 1	$\pm$ 0.9
31	$\pm$ 9	$\pm$ 3.1
38	$^{+\ 53}_{-\ 18}$	$\pm$ 3.8

The resolution of the proposed detector is significantly better than that obtained in the bubble chamber.

In Figure 11 we show the electromagnetic shower angular resolution versus the shower sampling interval. We see that the angular resolution of a 10 GeV electron is degraded by roughly a factor of 2 when the sampling interval is increased from 0.25 X_o to 1.0 X_o. The resolution degradation for 30 GeV showers on the other hand is less severe. Hence, to obtain good angular resolution at low energies, it is important to have a fine-grain sampling of the shower.

2. Hadrons

Hadron showers have been measured in the energy range, 5 to 300 GeV. Due to the small number of collision lengths (3.5) in the test array, the hadron shower could not be fully contained. However, the most important feature of the hadron response, namely energy flow angle resolution of the calorimeter could be determined.

a. Hadron Energy Flow Angle Resolution

We have used the first interaction of hadronic cascades to simulate the hadrons produced in neutrino interactions. The hadron energy flow direction of the particles emerging from this interaction point is determined by a least squares fit to the primary vertex position and the center of gravity coordinates of the hadron cascade versus shower depth. Since our calorimeter was only 3.5 interaction lengths long, we have only analyzed hadron showers which have interacted in the first 9 plates of the calorimeter. We have used the same two pass procedure as was used for electrons, but in this case we have made the road much broader at the back of the calorimeter and have increased the errors associated with each center of gravity coordinate to be 4 times larger than in the case of electromagnetic showers. This was necessary since the shower fluctuations are considerably larger in hadron showers than in electromagnetic showers.

In addition to the road cuts and differential weighting of the center of gravity coordinates, we have found an increase in the angular resolution could be obtained

at 100 and 200 GeV by computing the center of gravity coordinates by a weighted average rather than a straight average. The weights are determined by a gaussian fit to the lateral spread of the shower at a given shower depth. This new algorithm using this gaussian weighting procedure gave no improvement in the hadron energy flow angle resolution for $E_H \leq 40$ GeV but improved the 100 and 200 GeV angle resolution data by 20%. The angular resolutions for 100 and 200 GeV are shown in Figures 12a and 12b respectively. These resolutions, however, do not represent the resolutions of the neutrino calorimeter since the hadron shower is not contained.

Special care is necessary for predicting the angle resolution for 100 and 200 GeV hadron showers in the proposed calorimeter since the 3.5 interaction lengths of the test calorimeter contained only 40 to 50% of the hadronic shower. To compensate for this poor longitudinal containment, the angular resolution versus the longitudinal length of the shower was determined by cutting the shower after 12, 24, 40, and 55 chambers from the primary interaction vertex. The resulting angular resolution versus the allowed longitudinal size of the hadron shower for 100 and 200 GeV averaged together is shown in Figure 13. We have extrapolated the angular resolution to 6mrad based on a Monte Carlo Simulation at 100 GeV.

In Figure 14, we show the energy flow projected angle resolution versus $1/E_H$. We see that the angle

resolution becomes better with increasing energy as in the case of electromagnetic showers and has an energy dependence of roughly $\sigma(\theta_H) = (4 + 360/E_H\ (GeV))$ mrad. For comparison, we show the angular resolution of the CERN WA-18 experiment . In this experiment the hadronic showers are sampled every 44 gm/cm^2 versus 8 gm/cm^2 (one view) for this proposal.

We see that the hadron energy flow angular resolution of our proposal is almost twice as good as the CERN-WA-18 experiment. Good angular resolution is critical in the measurements of the x-distributions of semi-leptonic neutral currents.

b. Electron/Hadron Discrimination

Hadron showers are readily distinguishable from electron showers because of the larger average $p_\perp$ in a hadron collision and the somewhat different shower development curve of the hadron showers. We have checked this electron/hadron discrimination by taking data with no selection on the incident particle type and attempting to identify electrons in the data. A simple criterion was used to identify hadrons. If an event downstream of two radiation lengths contained at least one track, defined as at least nine cells forming a line without adjacent firing cells, then the incident particle was called a hadron. Otherwise it was identified as an electron. These measured electron/hadron (e/h) ratios for various incident energies were compared with the measured e/h ratios determined by the gas Cerenkov counter. The electron/hadron ratios determined by the flash chamber detector and the Cerenkov counter were consistent

with each other. We conclude that the hadron rejection is at least 100:1 at 30 and 40 GeV. Taking $\pi^+ + n \rightarrow \pi^0 + p$ charge exchange with at least one of the π° decay γ's converting in the first lead plate to represent the limit of the e/h discrimination, we estimate the e/h discrimination to be at least 1,000/1.

We have studied the average properties of hadronic and electromagnetic showers. This information is useful in designing particle selective triggers. In figure 15 we plot the total number of cells firing in each type of shower versus the energy of the shower. These data have been corrected for the energy loss out the back of the calorimeter. We see that hadronic and electromagnetic showers have roughly the same number of firing cells up to 40 GeV. (This is the upper energy measured so far for electrons.) This graph suggests that hadron energy as well as electromagnetic energy can be measured by the cell converting technique. We do not, however, require that hadron energy be measured this way since we have the proportional tubes for this.

In Figure 16 we compare the average number of cells which fire at a given shower depth for different energies for hadronic showers. This figure is to be compared with Figure 5. We see the increase of the number of cells with increasing energy as well as the expected slow increase in the depth of the shower maximum for both types of showers. For the same energy, electron showers peak at a slightly greater depth than hadron showers.

The lateral distributions for 10 and 30 GeV electromagnetic showers versus shower depth are shown in Figure 17. We see that for $E_e \leq 30$ GeV electromagnetic showers are contained in a cylinder of roughly $\leq$ 20 cm diameter.

The lateral distribution of hadronic showers for various different energies is shown in Figure 18. We see that the lateral spread of hadronic showers is greater than that of electromagnetic showers. For example, a 40 GeV hadron shown is contained in a cylinder of 30cm diameter (less than the lateral size of the calorimeter), whereas an electron shower of this energy requires only 20cm for containment. This different lateral spread is very useful in designing a selective trigger for electromagnetic showers.

V. Summary

We have measured the response of the test calorimeter to electrons in the range 5 to 300 GeV. The electron (and perhaps the hadron) energy can be measured by counting the number of cells firing in the shower. The electron energy resolution obtained by this technique is $\frac{\sigma(E)}{E} \leq 10\%$ and is independent of energy. The electron projected angle resolution is $\sigma(\theta e) = 2 + \frac{70}{E_e}$ (mrad). The muon angular resolution is 1.8 mrad at 10 GeV. The hadron energy flow projected angular resolution is $\sigma(\Theta_H) = 4.0 + 360/E_H$ (mrad). This is roughly a factor of 2 better than the resolution obtained by the WA-18 CERN experiment.

TABLE I.

Summary of Flash Chamber Tests

Number of Analyzed Events

M5 Beam

Beam Momentum	Hadrons	Electrons	Muons
5 GeV/c	(20)	20	
10	21	17	25
20	35	43	
30	(30)	21	
40	28	(30)	

N3 Beam

50 GeV/c	(80)		
100	80		
200	25 + (55)		
300	(80)		

(...) data taken but not yet analyzed.

APPENDIX A

FIGURE CAPTIONS

Photograph: Pictured is the test apparatus used in the M5 beam. The tubes at the bottom of photograph are for the gas input. The boxes on the top are 7 spark gaps, each of which is used to pulse 9 flash chambers. Visible are the six scintillation counters placed behind the 5 mm lead sheets. The chambers are viewed from the left.

Fig. 1a: Layout of the test apparatus showing placement of lead, scintillation counters and arrangement of the polypropylene sheets.

Fig. 1b: Details of one flash chamber gap showing the 6.4 mm aluminum electrodes, the polypropylene sheet and the gas manifold.

Fig. 2: A typical HV plateau curve for a flash chamber in the test calorimeter is shown.

Fig. 3. The flash chamber efficiency versus delay of the HV pulse is shown.

Fig. 4a: A set of typical electromagnetic showers at various energies is shown.

Fig. 4b: A set of typical hadronic showers.

Fig. 5: The average number of cells which fire at a given shower depth for several incident electron energies.

Fig. 6: The average number of firing cells versus the energy of the incident electron.

Fig. 7: Histogram of the number of cells which fire for 20 GeV electrons.

Fig. 8: The energy resolution σ/mean in percent versus the incident electron energy (left hand scale). The corresponding fluctuations of the number of firing cells in percent are shown on the right hand scale.

Fig. 9: An example of the two pass fitting procedure of a 30 GeV electromagnetic shower. The lateral center of gravity coordinates x are plotted against the shower depth y. a) The first pass fit to the shower is denoted by the solid line. The space between dotted lines is the "road". b) The second pass fit is shown. Note the increase of the error flags as the shower depth y is increased.

Fig. 10: Projected (1 view) electron angle resolution versus the reciprocal of the electron energy. The angle resolution for 10 GeV muons is shown for comparison.

Fig. 11: Electron angular resolution versus the shower sampling step for 10 GeV showers and 30 GeV showers.

Fig. 12: Measured hadron angular resolution. These are not corrected for the longitudinal containment. a) 100 GeV, b) 200 GeV.

Fig. 13: The hadron angular resolution for 100 GeV and 200 GeV (averaged) hadron showers versus the length of the allowed containment. The "theoretical" limit is computed by a Monte Carlo simulation.

Fig. 14: The hadron energy flow projected angle resolution is plotted against the reciprocal of the incident

hadron energy. The measured resolutions of this proposal and those of the WA-18 experiment at CERN are shown.

Fig. 15: The number of firing cells versus the energy for hadron showers and electron showers.

Fig. 16: The average number of cells which fire at a given shower depth for various incident hadron energies. This figure is to be compared to Fig. 5 which displays the same thing for electrons.

Fig. 17: a) The lateral distributions of 10 GeV electromagnetic showers at various shower depths. b) The lateral distributions of 30 GeV electromagnetic showers versus shower depth.

Fig. 18: The lateral distribution of hadronic cascades versus shower depth. a) 10 GeV incident hadrons, b) 40 GeV incident hadrons, c) 100 GeV incident hadrons and d) 200 GeV incident hadrons.

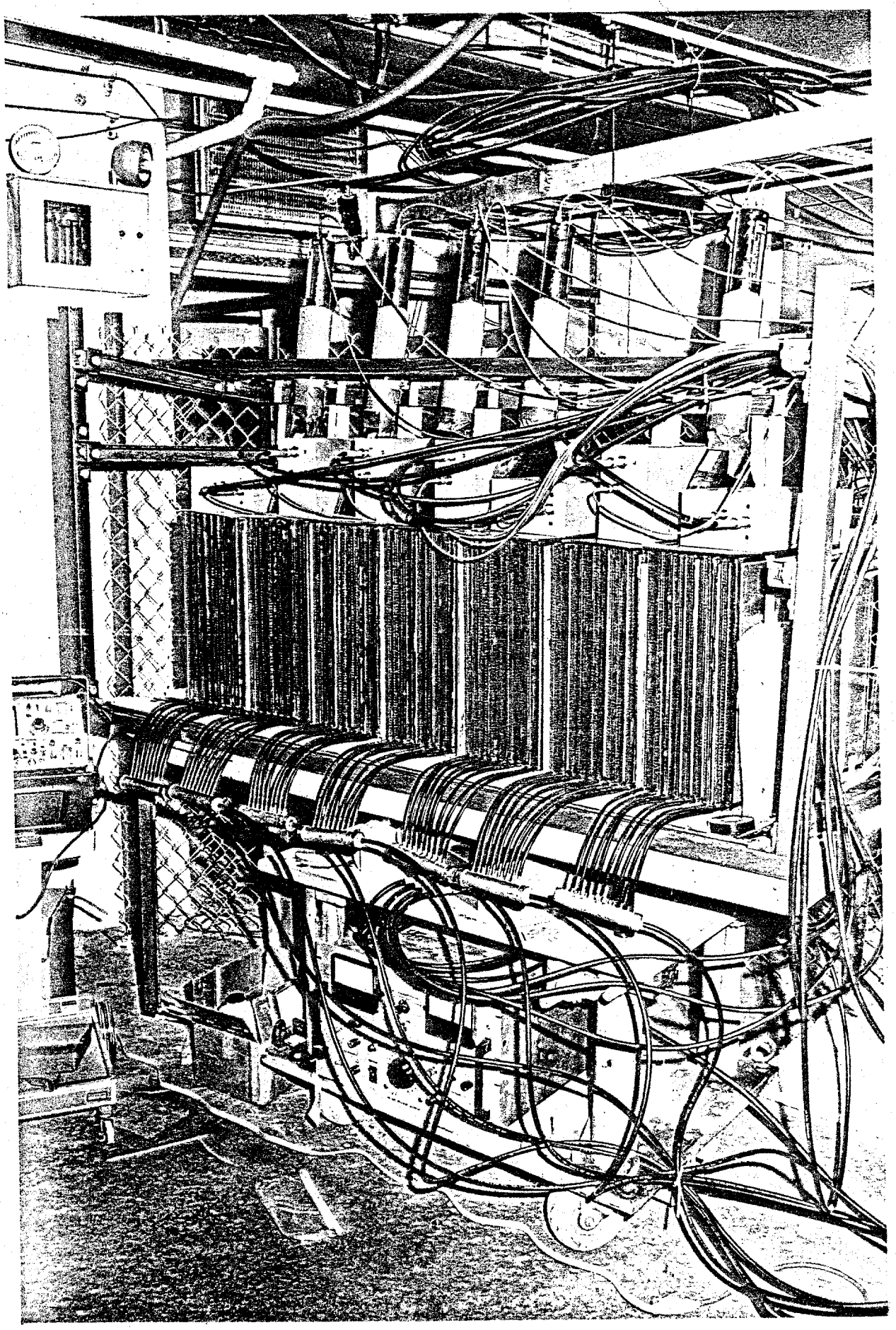

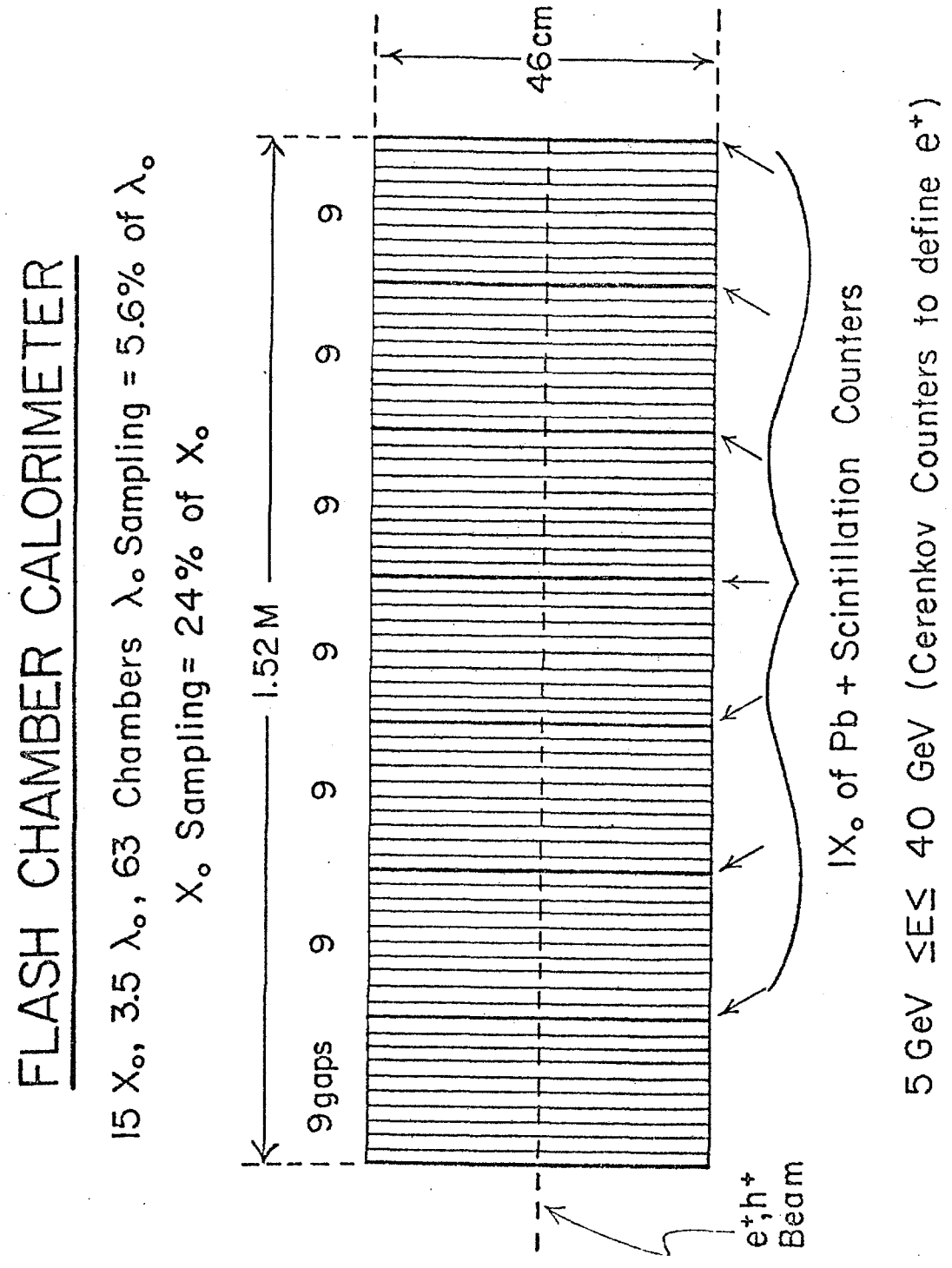
FLASH CHAMBER CALORIMETER
15 X_o, 3.5 λ_o, 63 Chambers λ_o Sampling = 5.6% of λ_o
X_o Sampling = 24% of X_o
1.52 M
9 gaps
9
9
9
9
9
46cm
$1X_o$ of Pb + Scintillation Counters
5 GeV $\leq E \leq$ 40 GeV (Cerenkov Counters to define e^+)
e^+, h^+ Beam

Fig. 1a

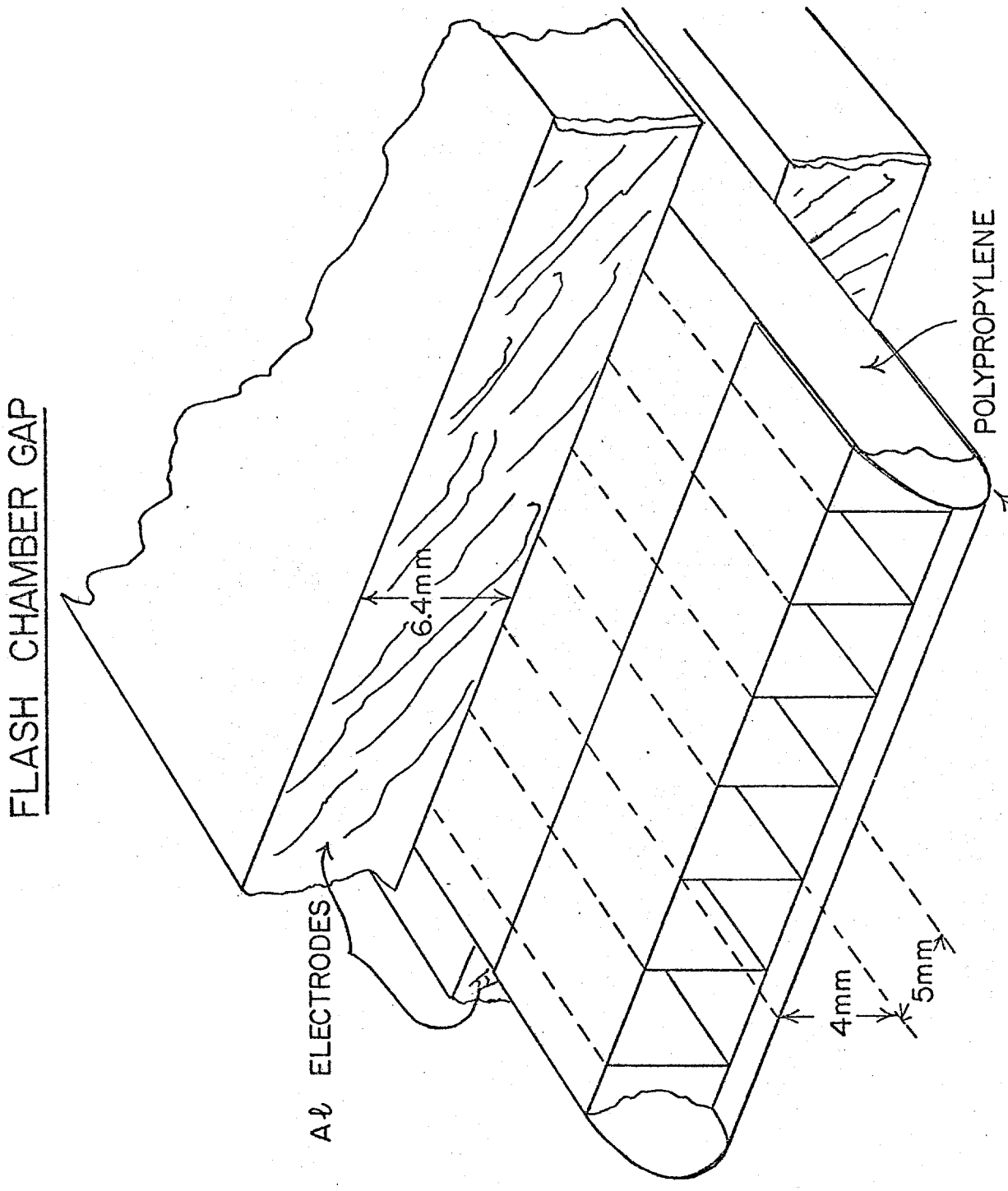
FLASH CHAMBER GAP
Al ELECTRODES
6.4mm
4mm
5mm
POLYPROPYLENE
GAS MANIFOLD

Fig. 1b

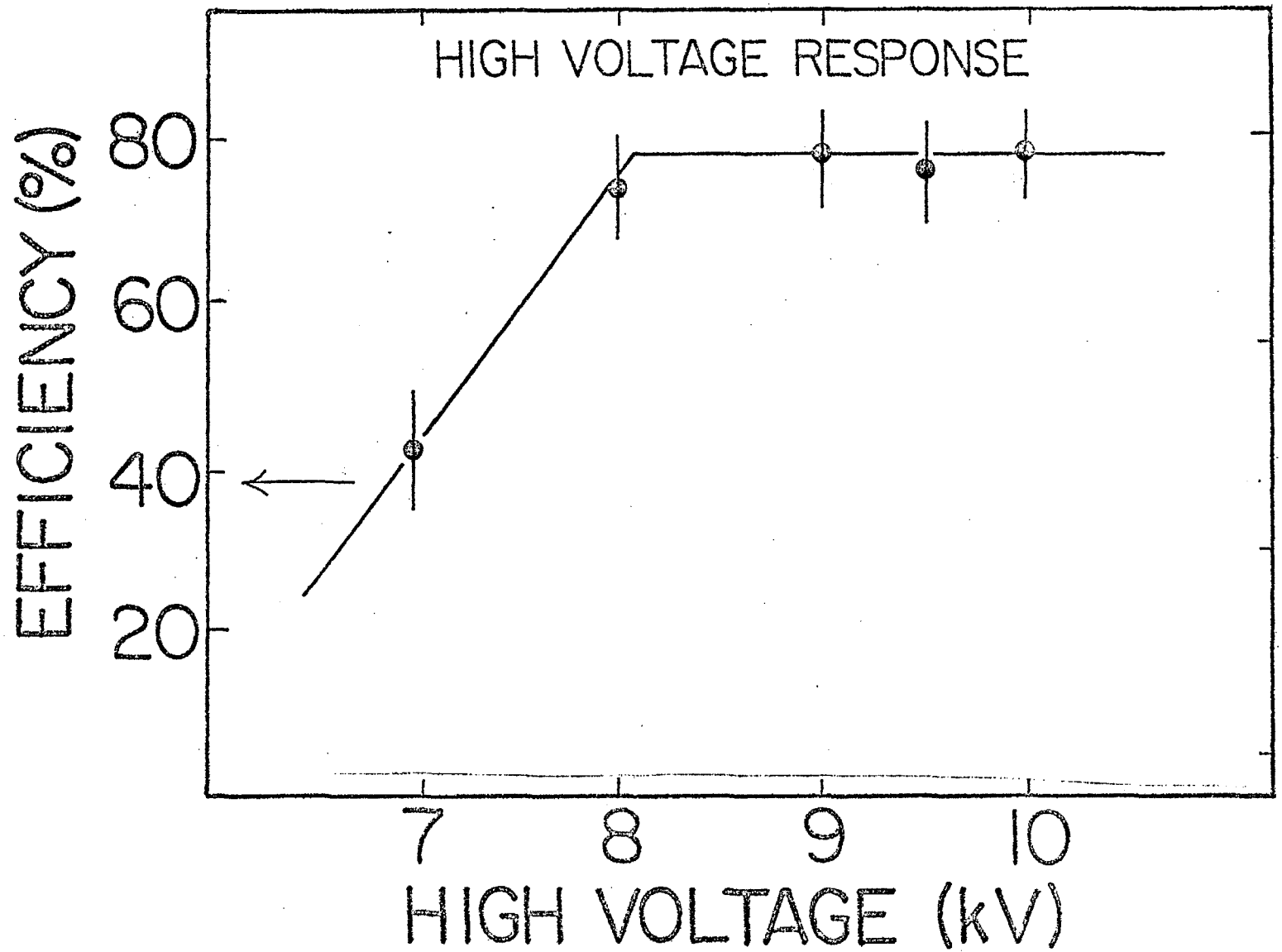
HIGH VOLTAGE RESPONSE
EFFICIENCY (%)
80
60
40
20
7
8
9
10
HIGH VOLTAGE (kV)

Fig. 2

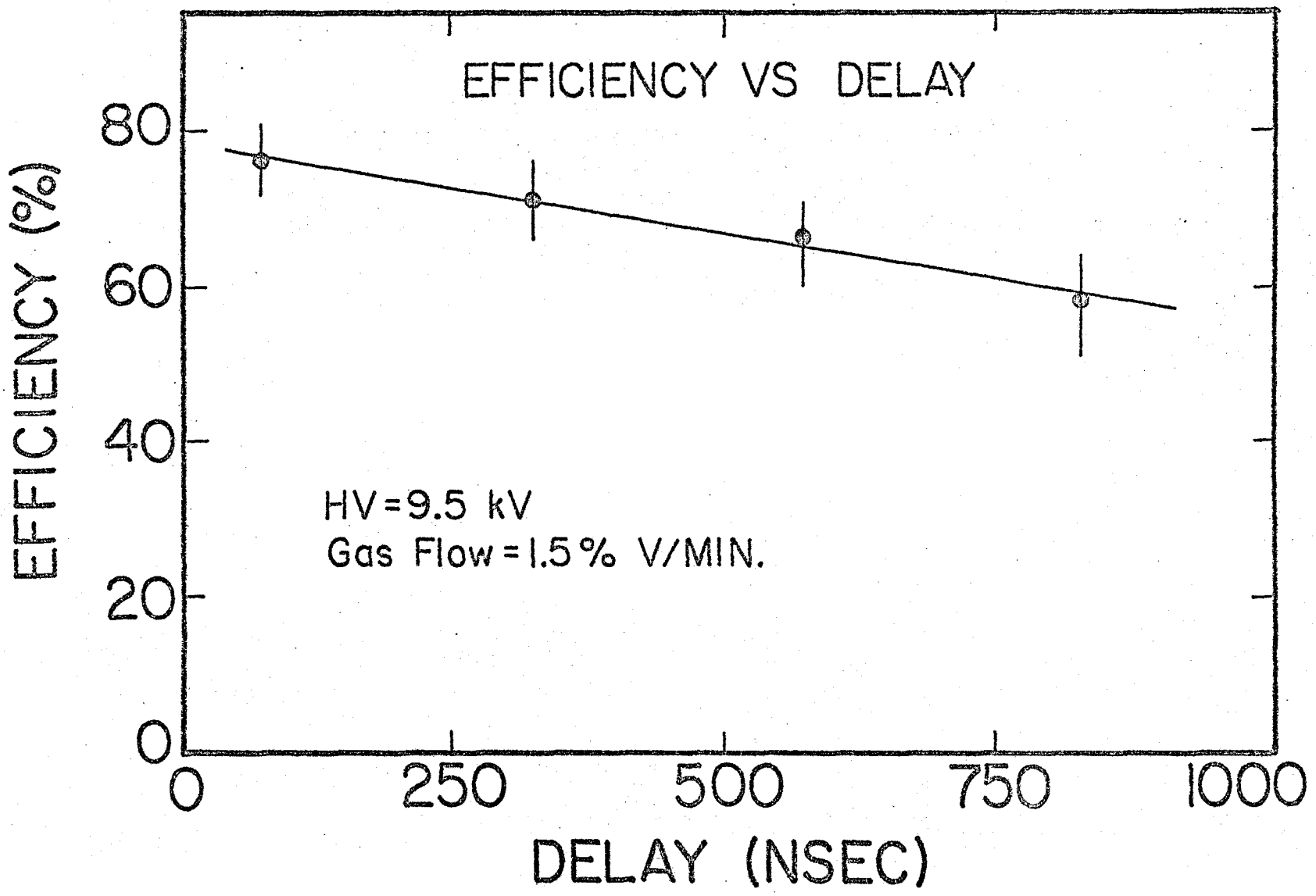
EFFICIENCY VS DELAY
EFFICIENCY (%)
80
60
40
20
0
HV=9.5 kV
Gas Flow=1.5% V/MIN.
0
250
500
750
1000
DELAY (NSEC)

Fig. 3

ELECTRON SHOWERS

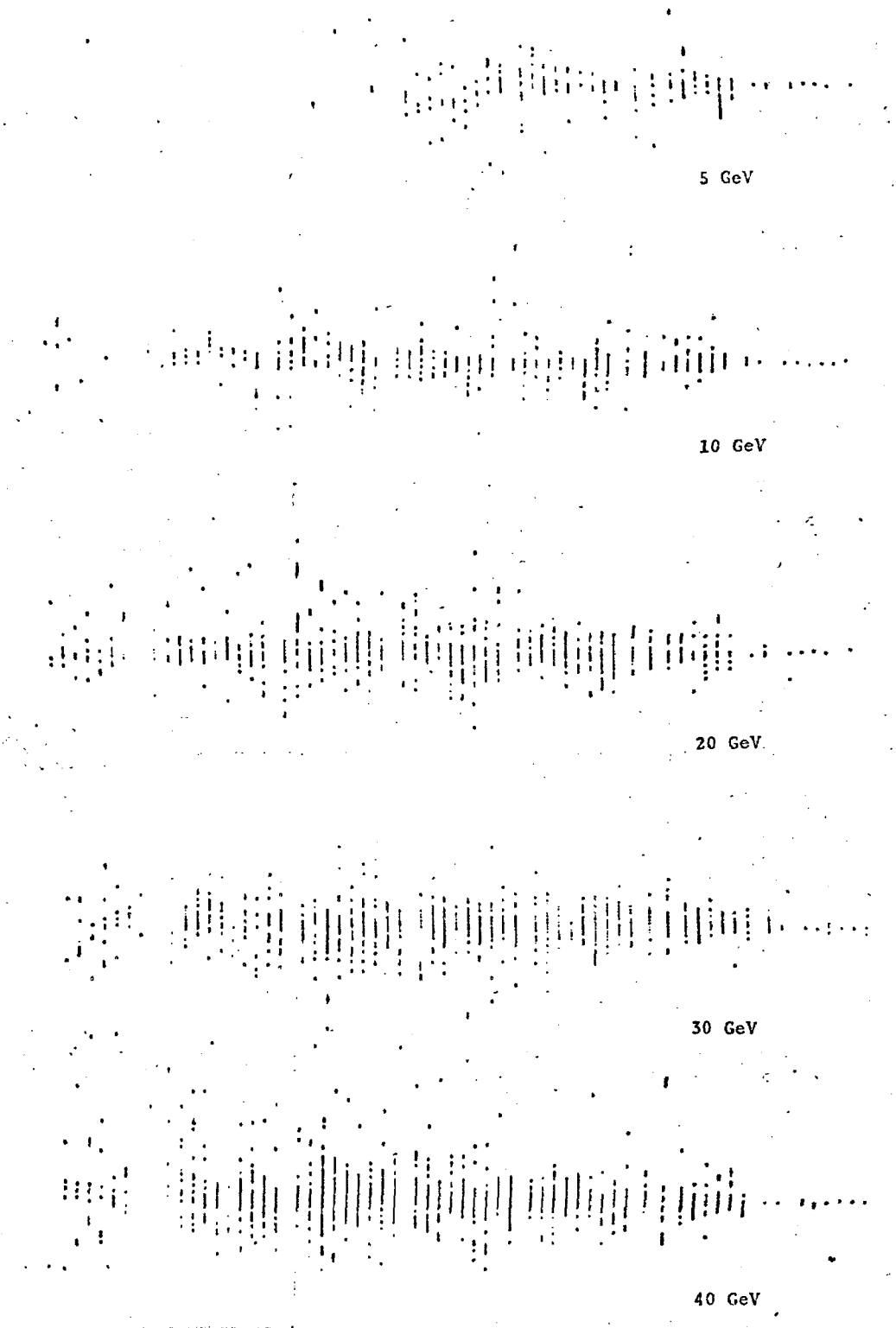

Fig. 4a

HADRON SHOWERS

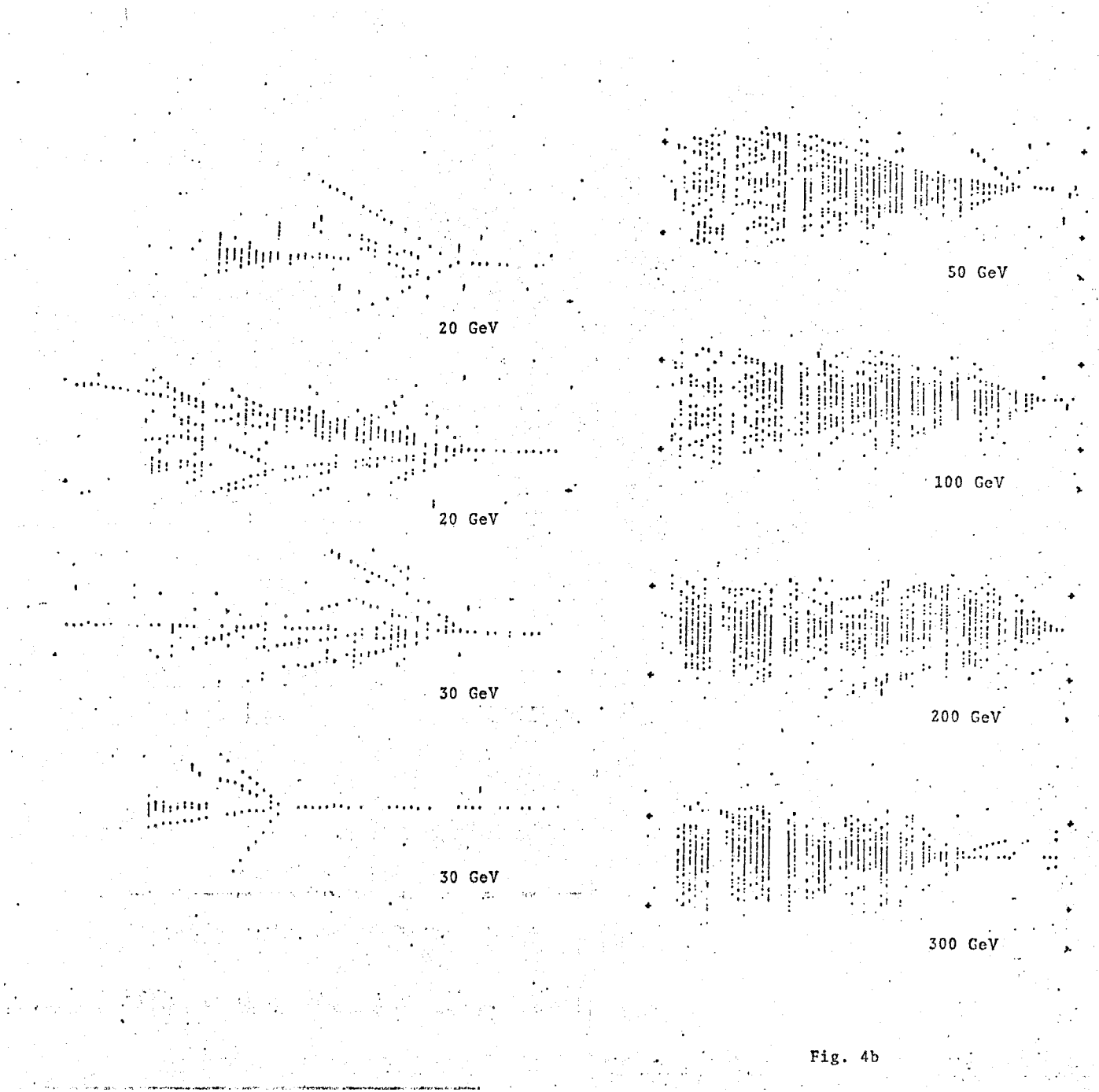

Fig. 4b

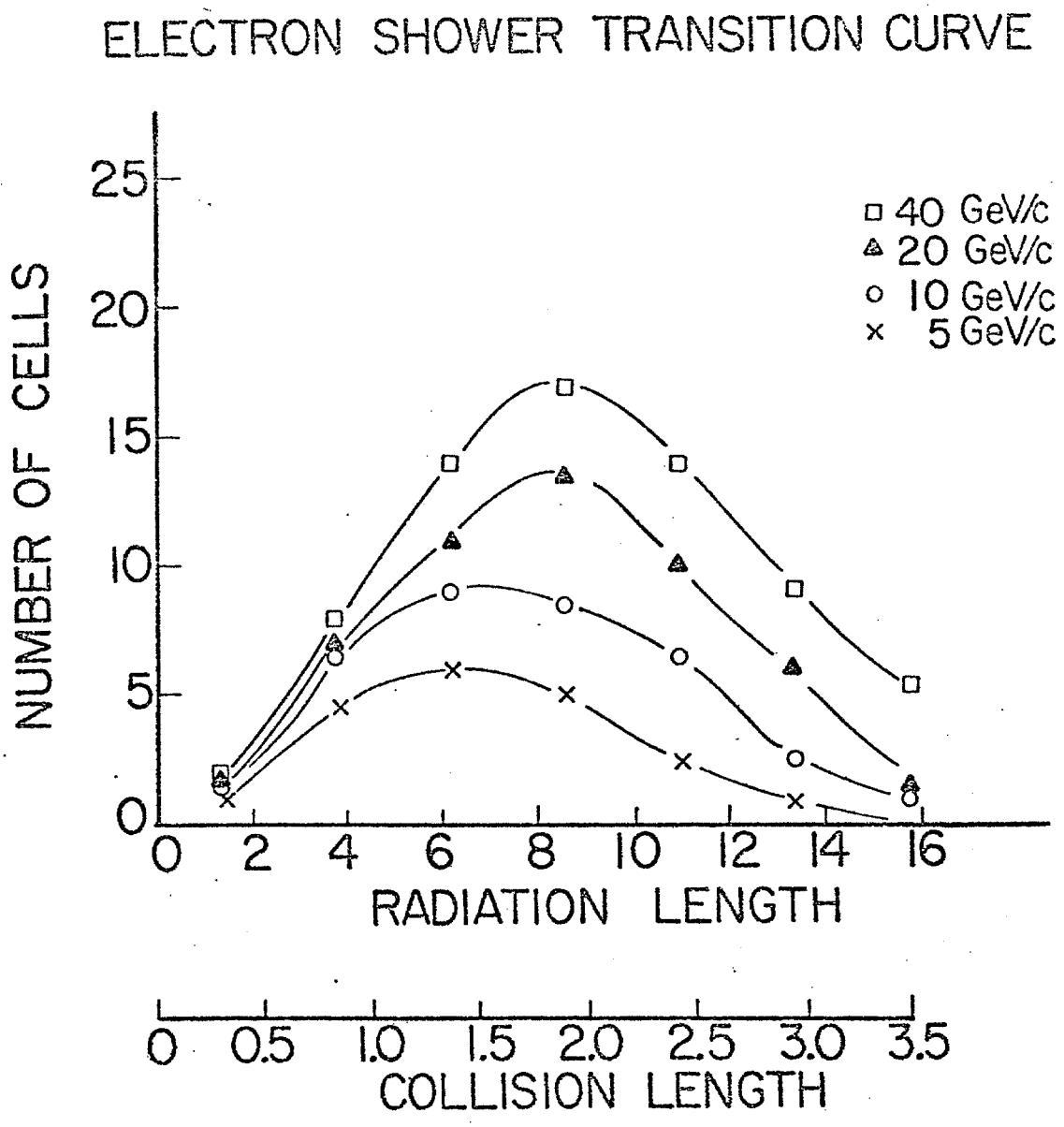
ELECTRON SHOWER TRANSITION CURVE
NUMBER OF CELLS
25
20
15
10
5
0
40 GeV/c
20 GeV/c
10 GeV/c
5 GeV/c
0 2 4 6 8 10 12 14 16
RADIATION LENGTH
0 0.5 1.0 1.5 2.0 2.5 3.0 3.5
COLLISION LENGTH

Fig. 5

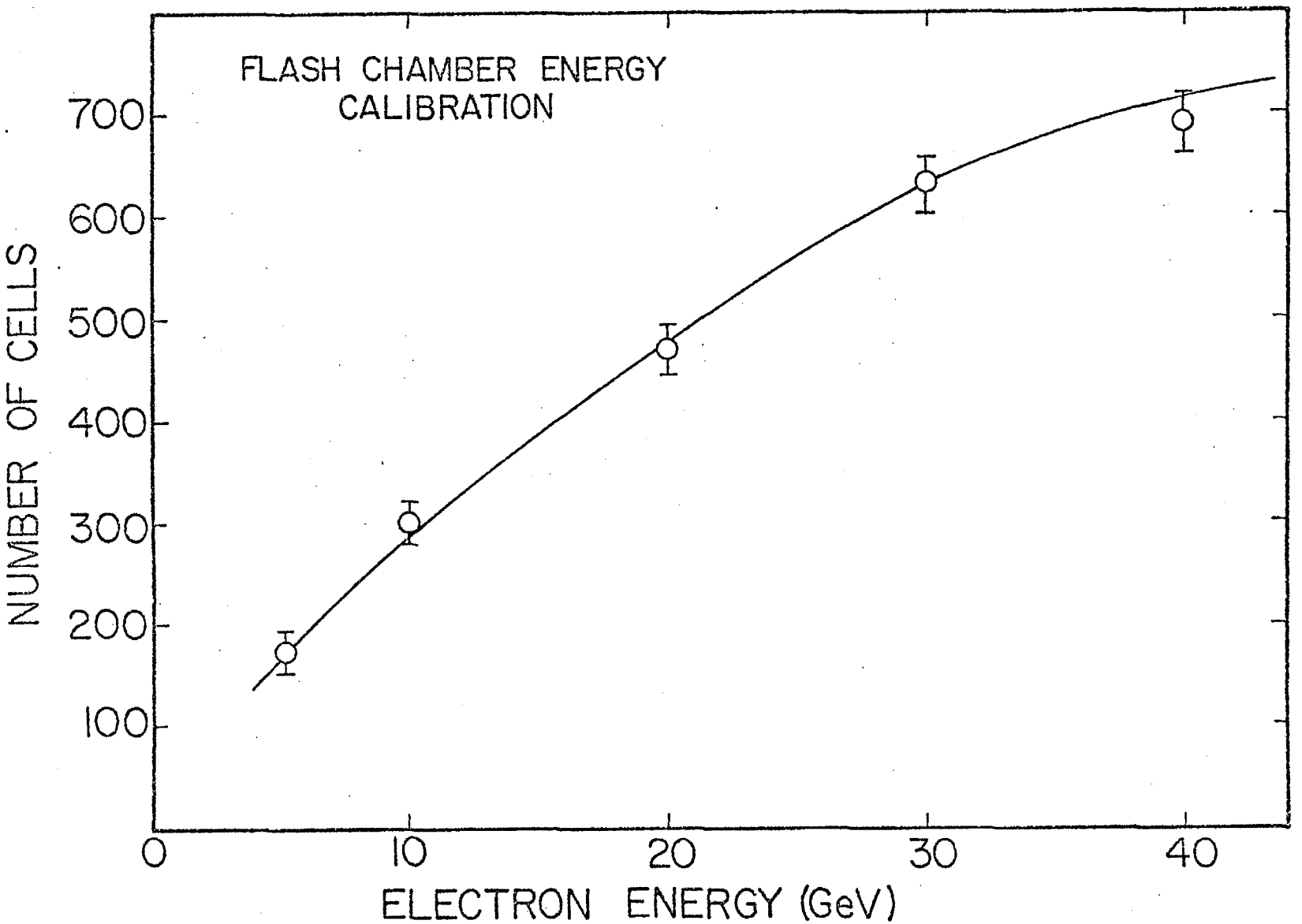
FLASH CHAMBER ENERGY
CALIBRATION
NUMBER OF CELLS
700
600
500
400
300
200
100
0
10
20
30
40
ELECTRON ENERGY (GeV)

Fig. 6

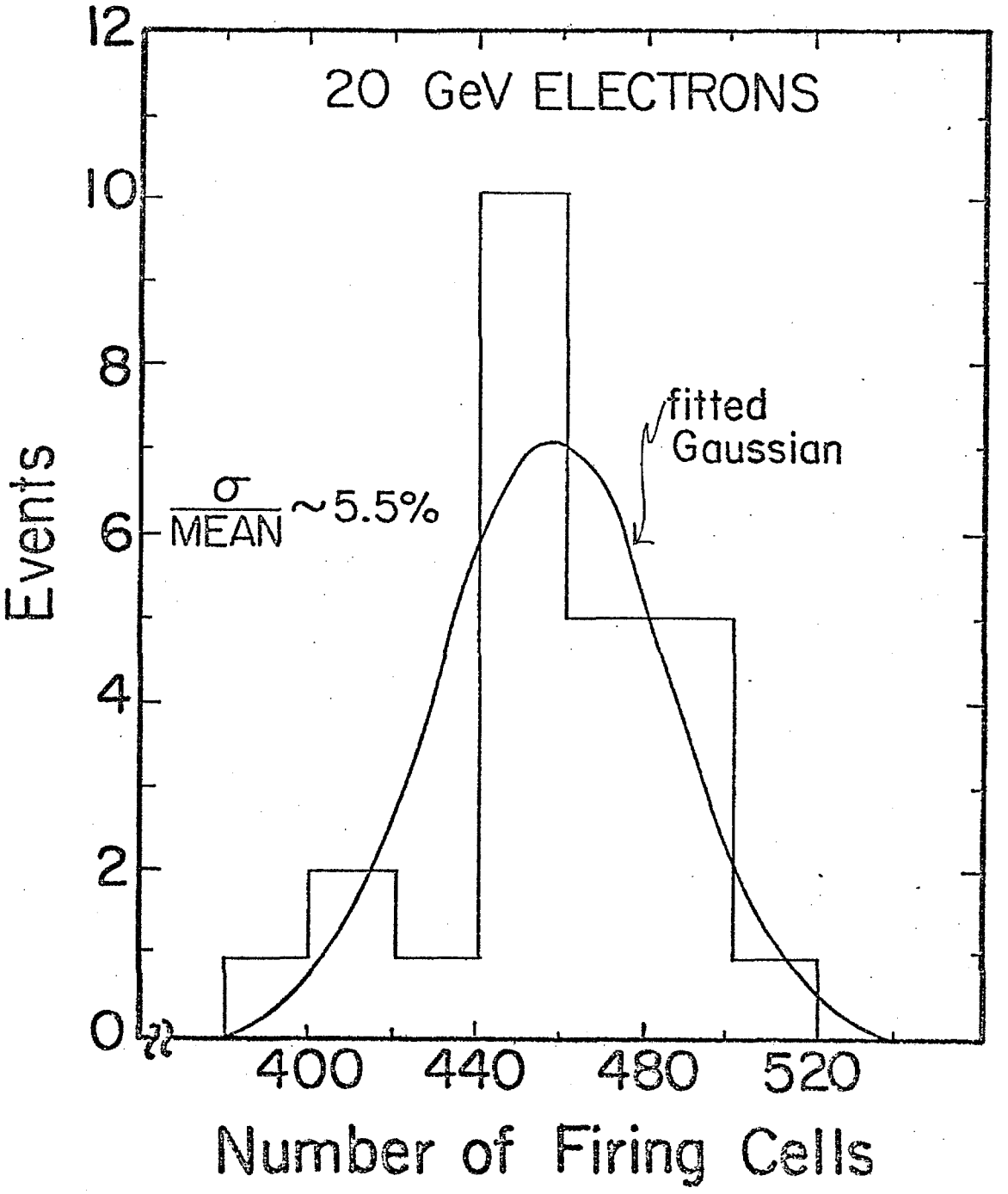
20 GeV ELECTRONS
Events
Number of Firing Cells
fitted Gaussian
σ/MEAN ~5.5%
0
2
4
6
8
10
12
400
440
480
520

Fig. 7

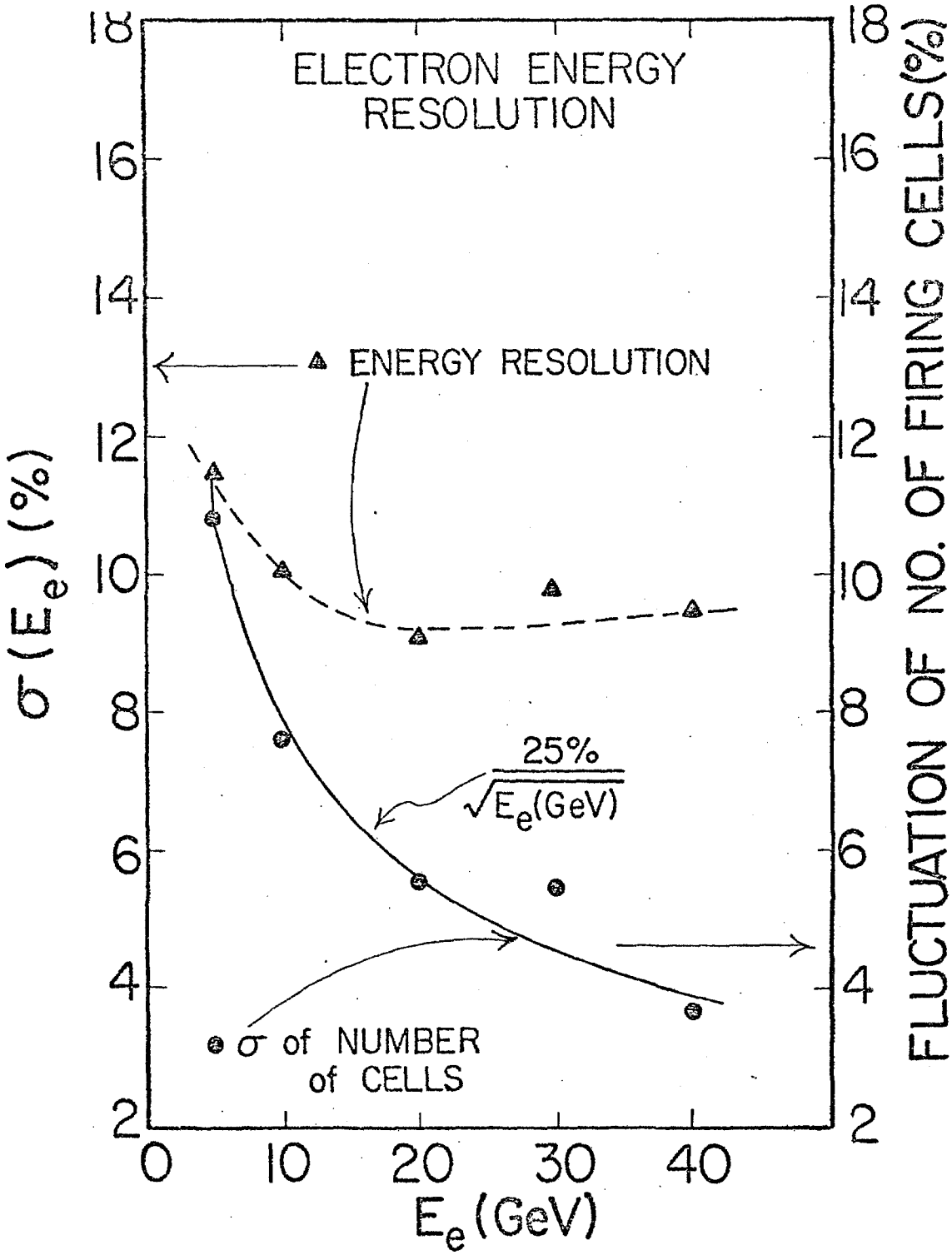
ELECTRON ENERGY RESOLUTION
ENERGY RESOLUTION
25%
√Ee(GeV)
σ of NUMBER of CELLS
σ (Ee) (%)
FLUCTUATION OF NO. OF FIRING CELLS(%)
Ee (GeV)
0
10
20
30
40
2
4
6
8
10
12
14
16
18

Fig. 8

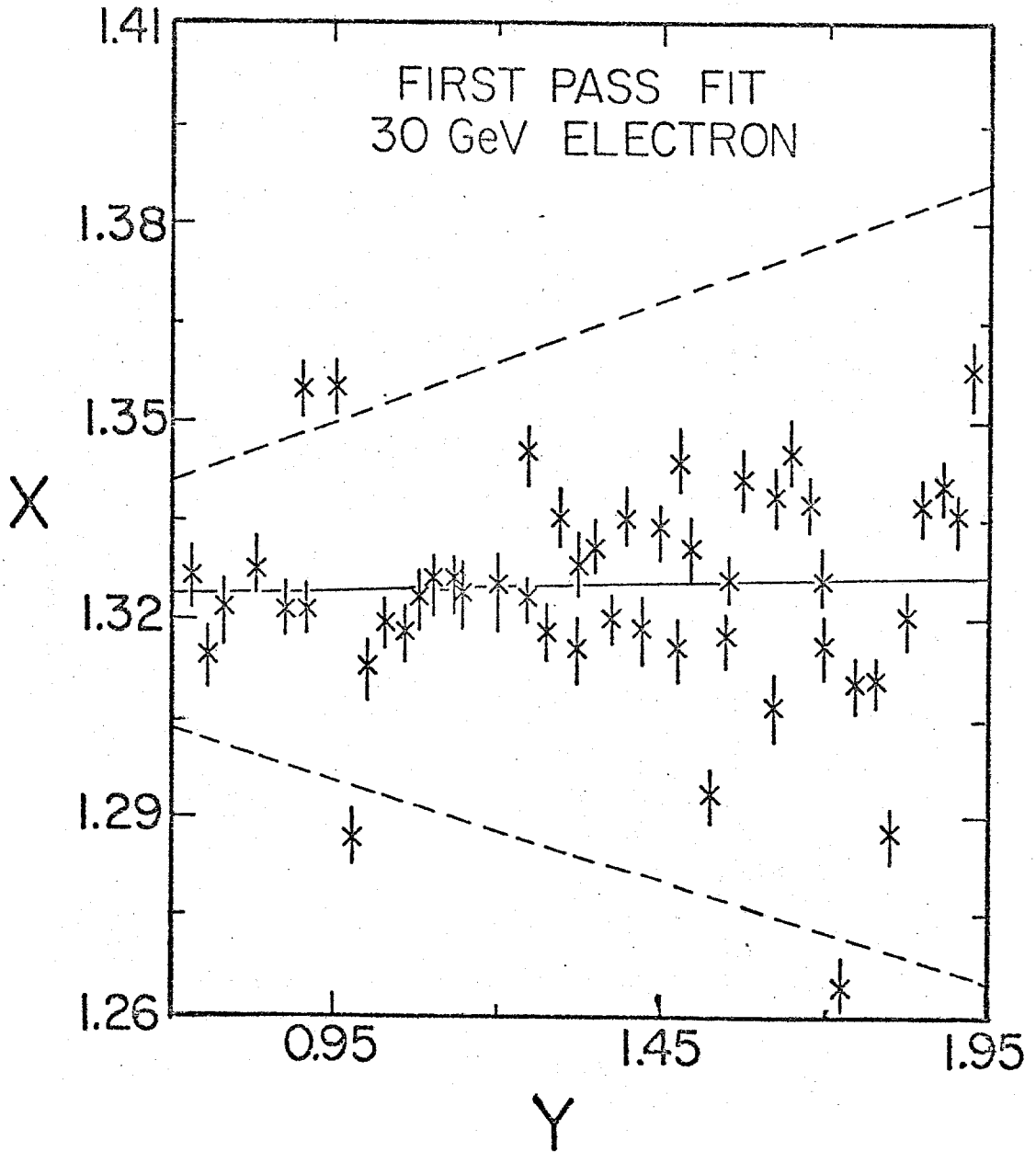
FIRST PASS FIT
30 GeV ELECTRON
1.41
1.38
1.35
1.32
1.29
1.26
X
0.95
1.45
1.95
Y

Fig. 9a

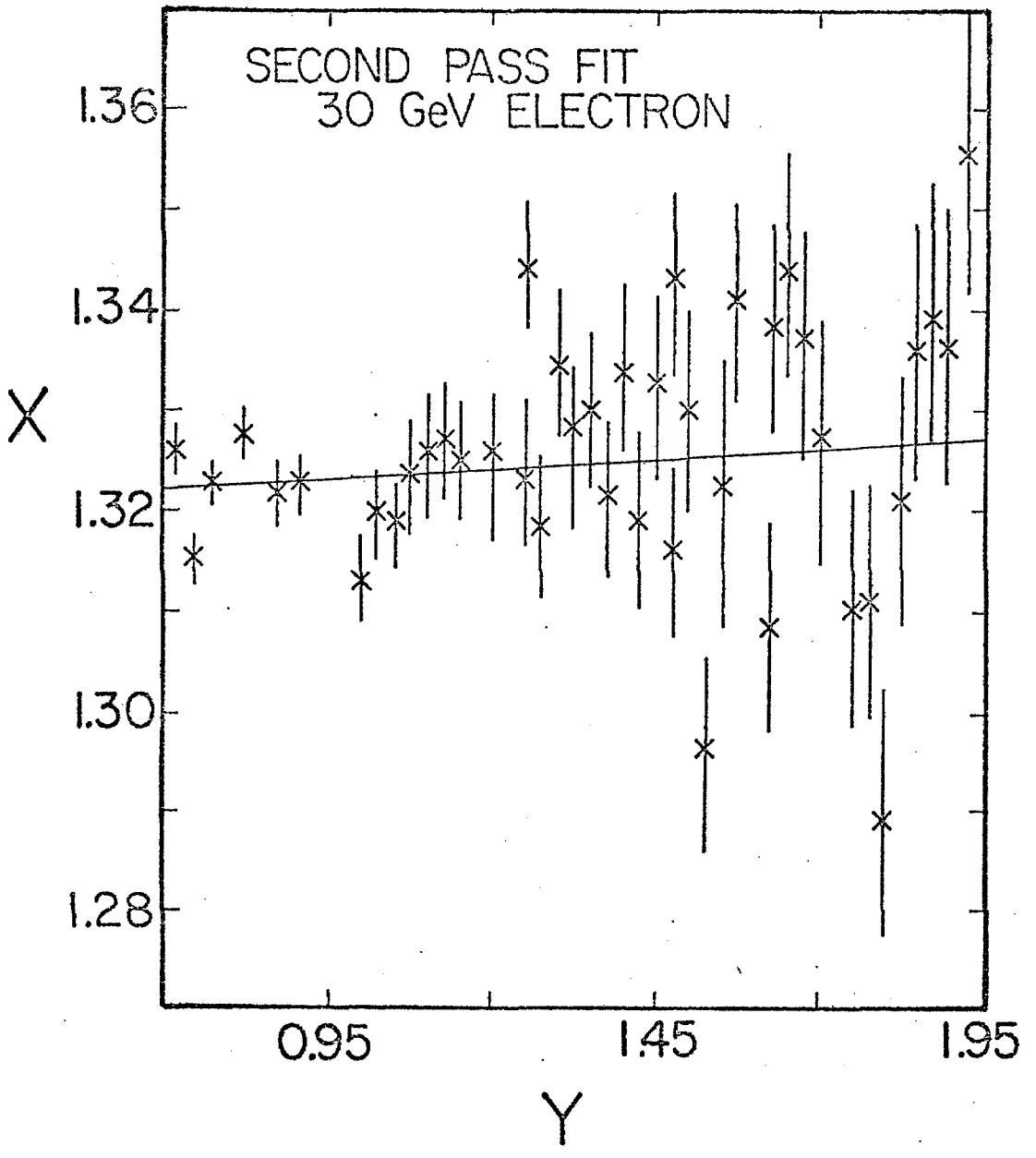
SECOND PASS FIT
30 GeV ELECTRON
1.36
1.34
1.32
1.30
1.28
X
0.95
1.45
1.95
Y

Fig. 9b

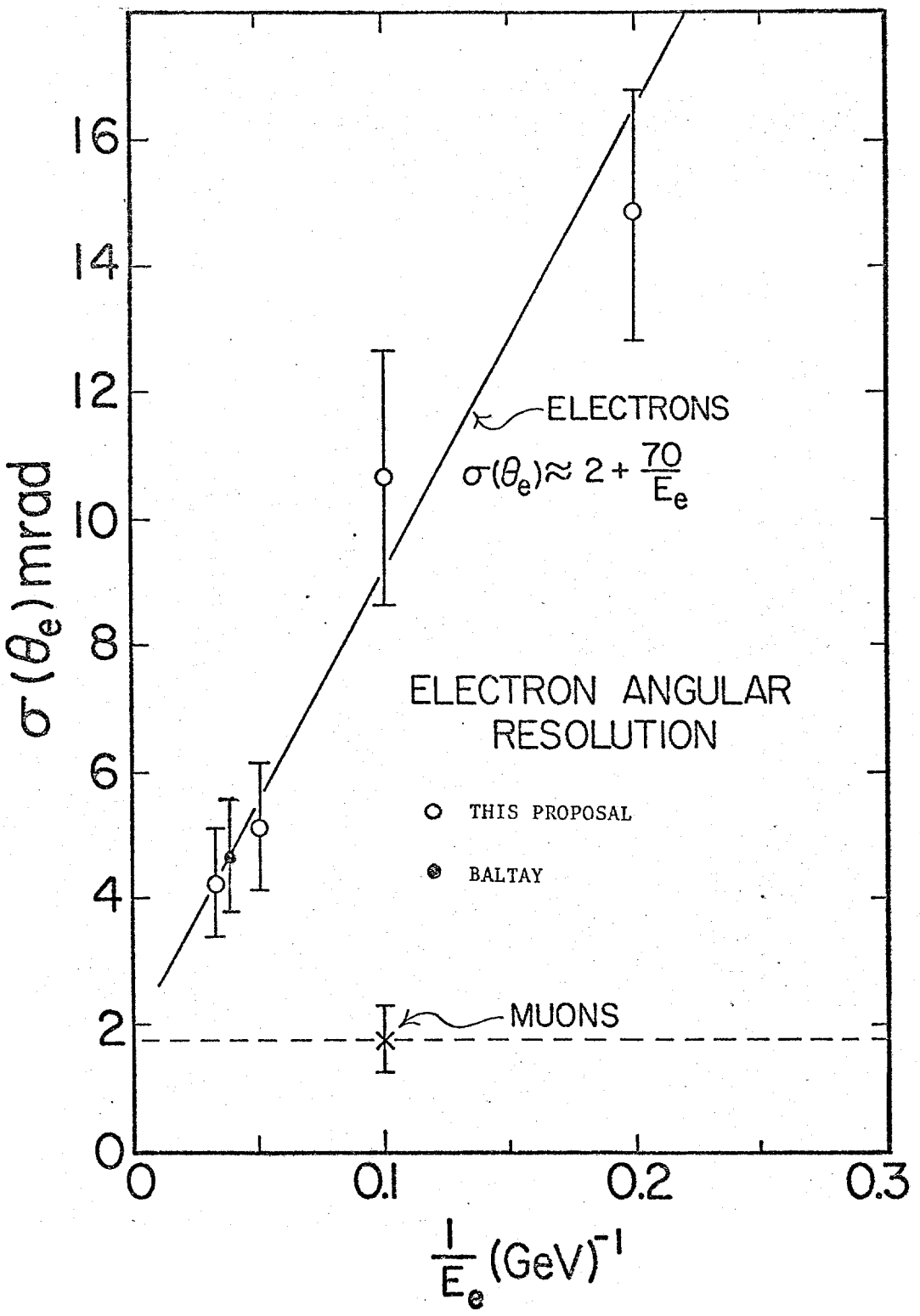
16
14
12
10
8
6
4
2
0
0
0.1
0.2
0.3
σ(θe) mrad
1/Ee (GeV)⁻¹
ELECTRONS
σ(θe)≈ 2 + 70/Ee
ELECTRON ANGULAR RESOLUTION
THIS PROPOSAL
BALTAY
MUONS

Fig. 10

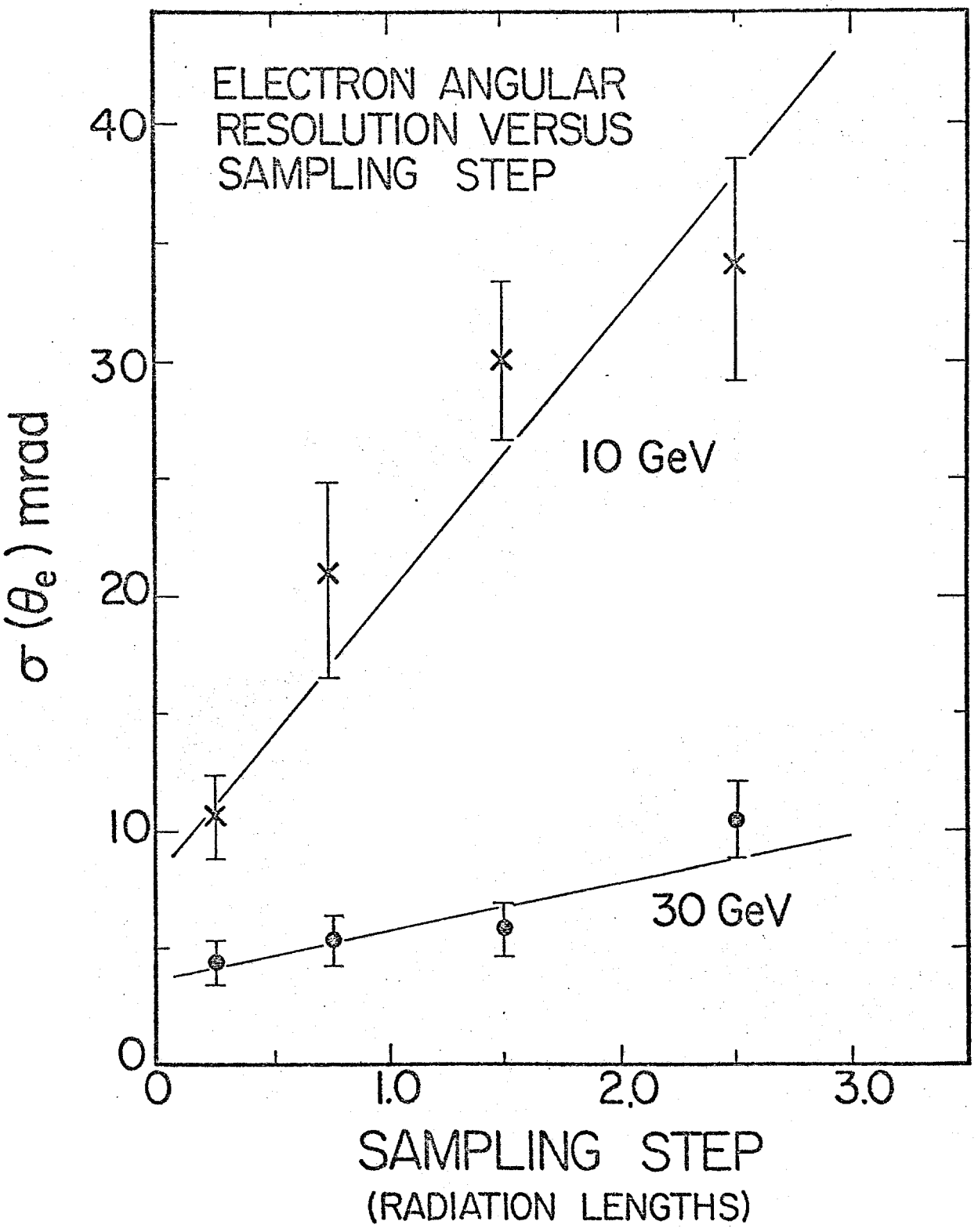
ELECTRON ANGULAR
RESOLUTION VERSUS
SAMPLING STEP
10 GeV
30 GeV
σ (θe) mrad
0
10
20
30
40
0
1.0
2.0
3.0
SAMPLING STEP
(RADIATION LENGTHS)

Fig. 11

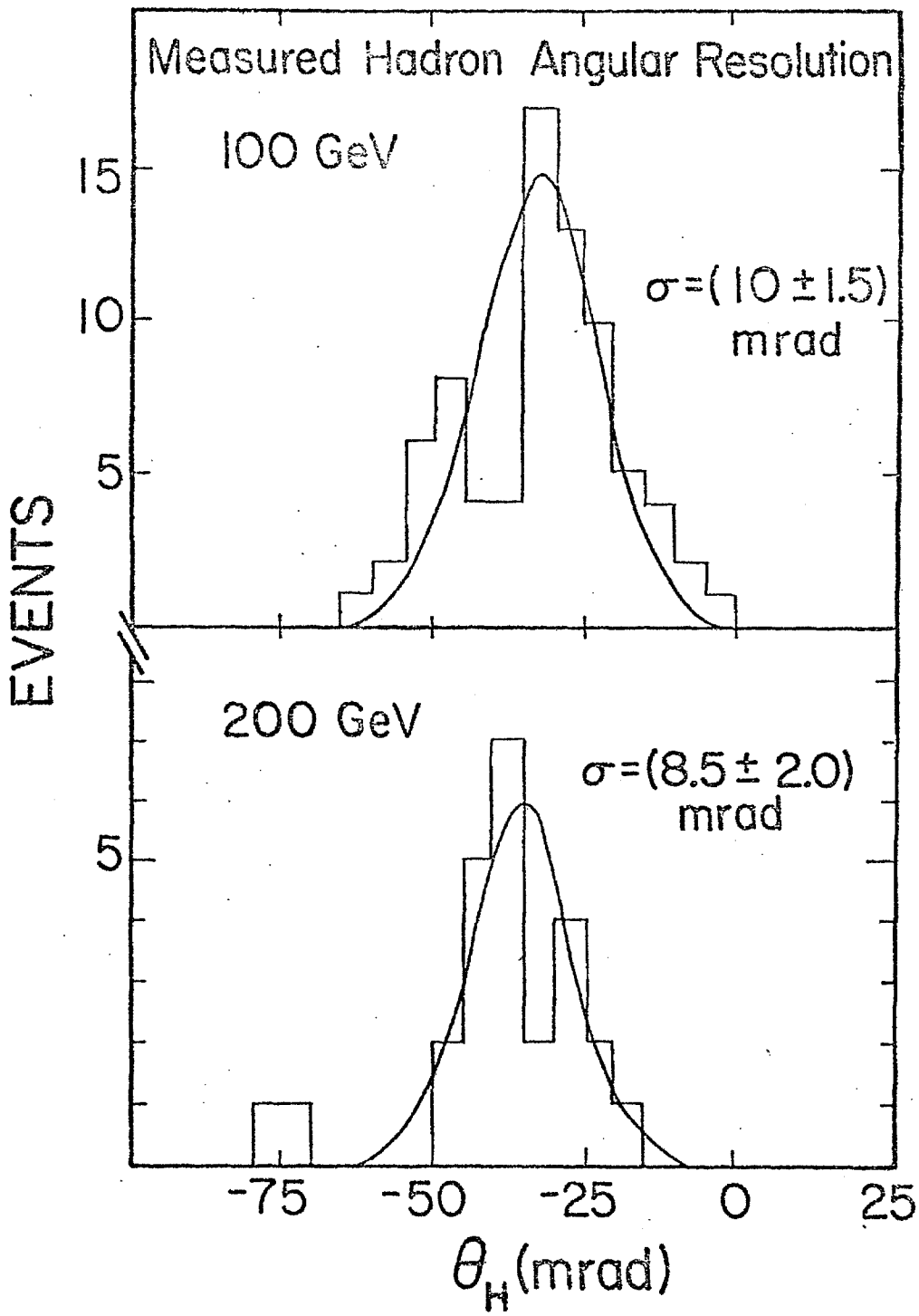

Fig. 12a

Fig. 12b

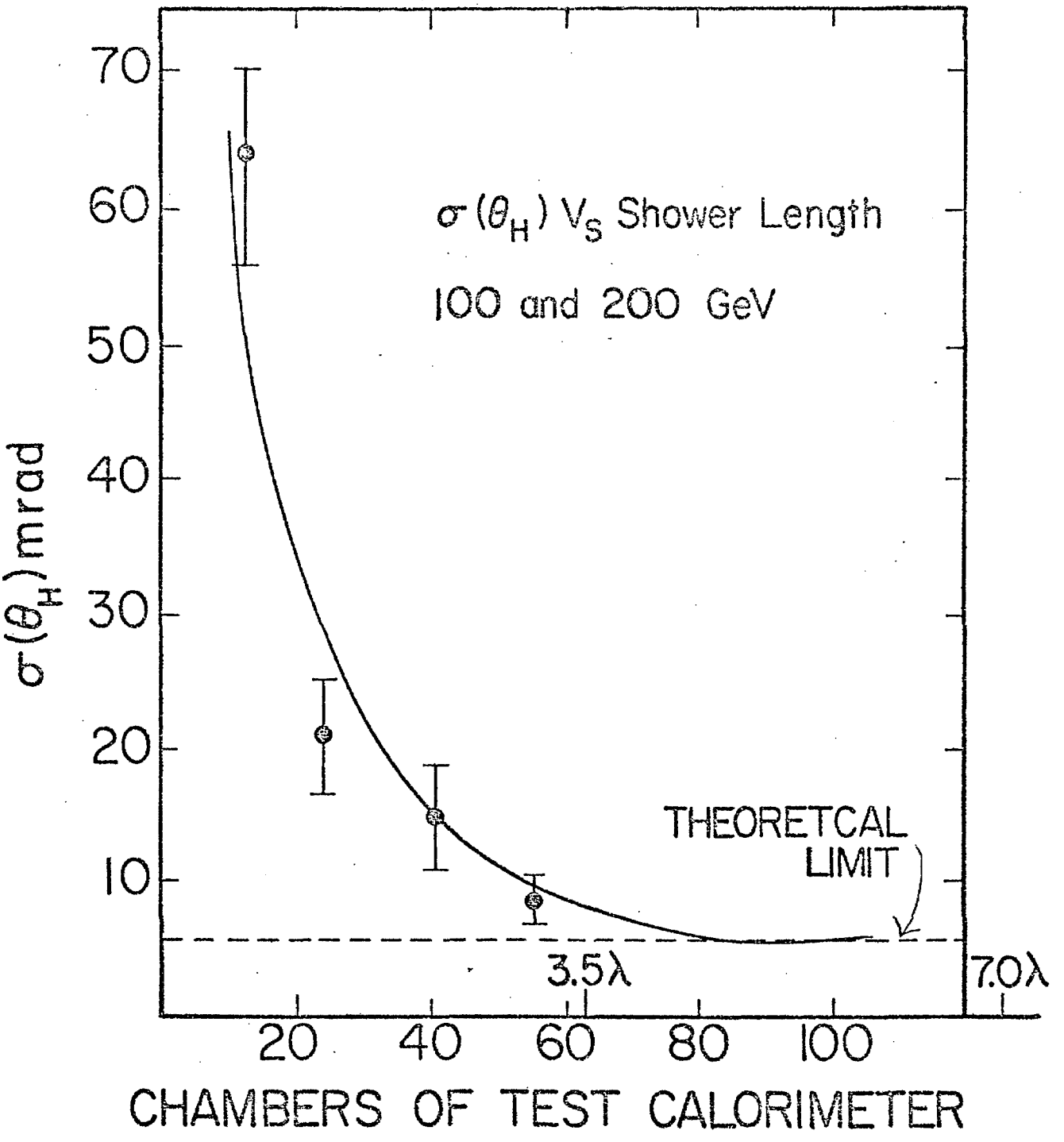
70
60
50
40
30
20
10
σ(θH) mrad
σ(θH) Vs Shower Length
100 and 200 GeV
THEORETCAL
LIMIT
3.5λ
7.0λ
20
40
60
80
100
CHAMBERS OF TEST CALORIMETER

Fig. 13

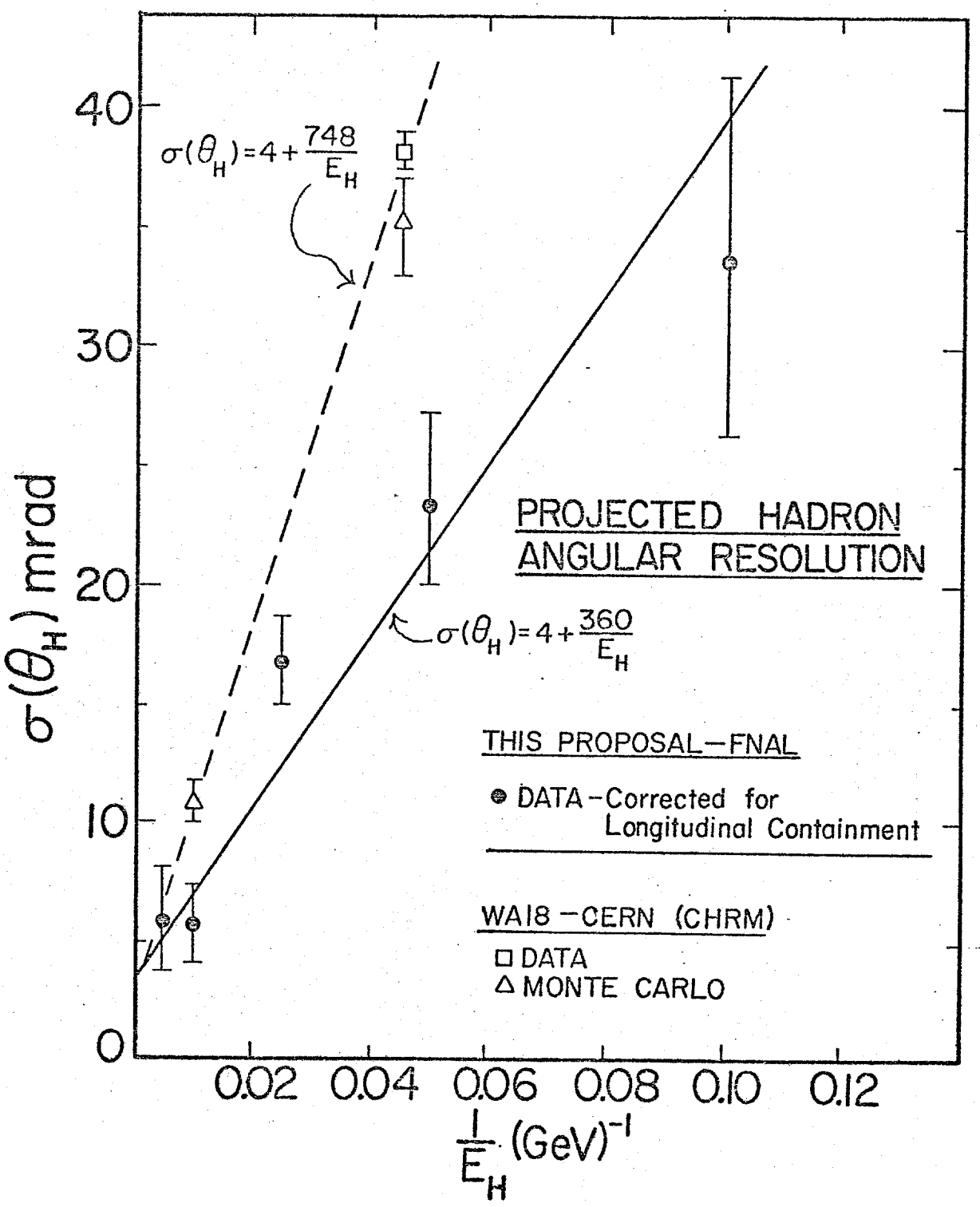
$\sigma(\theta_H)=4+\frac{748}{E_H}$
$\sigma(\theta_H)=4+\frac{360}{E_H}$
PROJECTED HADRON ANGULAR RESOLUTION
THIS PROPOSAL—FNAL
DATA—Corrected for Longitudinal Containment
WA18—CERN (CHRM)
DATA
MONTE CARLO
$\sigma(\theta_H)$ mrad
$\frac{1}{E_H}$ (GeV)$^{-1}$
0
10
20
30
40
0.02
0.04
0.06
0.08
0.10
0.12

Fig. 14

figure 15

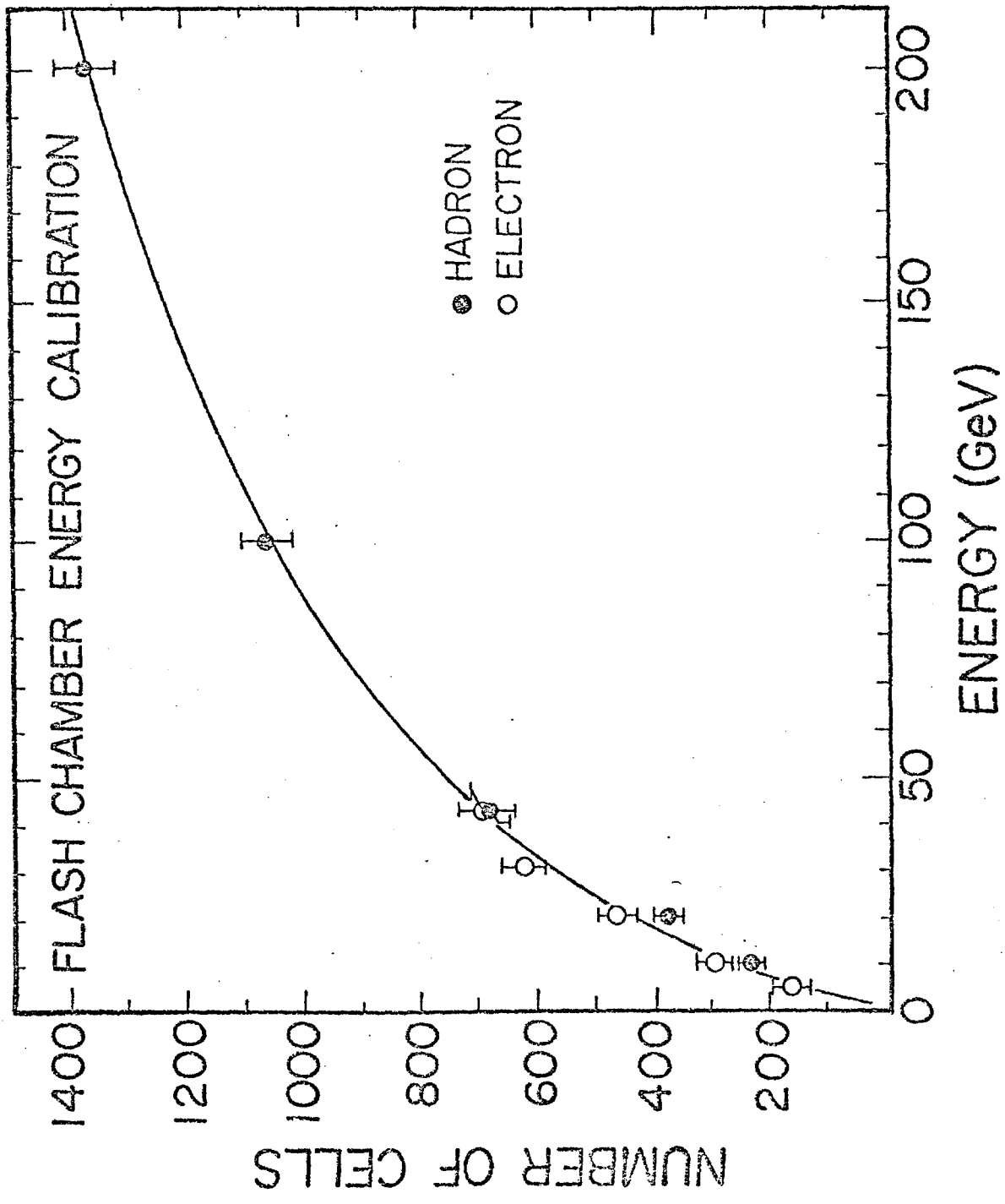
FLASH CHAMBER ENERGY CALIBRATION
HADRON
ELECTRON
NUMBER OF CELLS
ENERGY (GeV)
1400
1200
1000
800
600
400
200
0
50
100
150
200

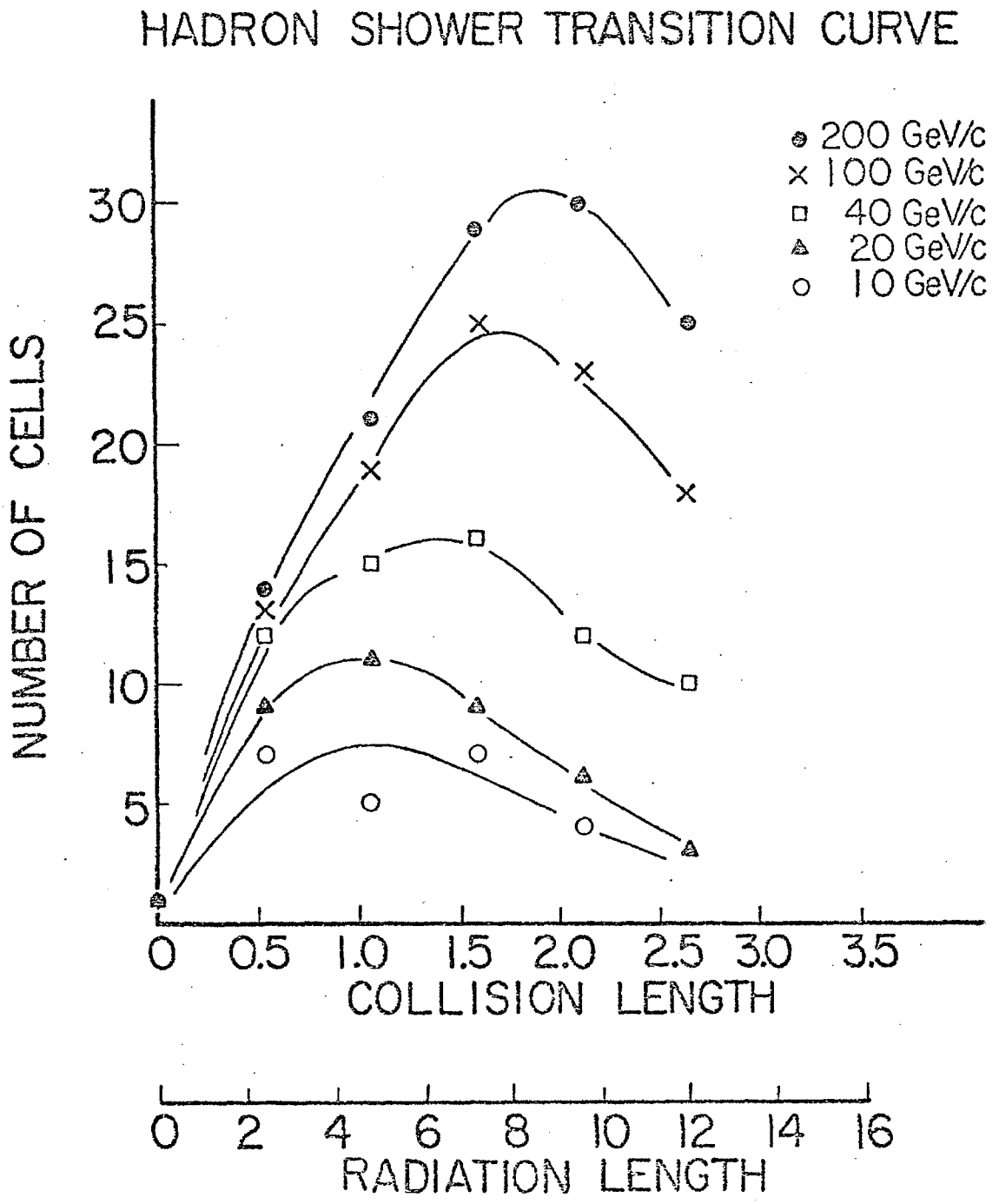
HADRON SHOWER TRANSITION CURVE
200 GeV/c
100 GeV/c
40 GeV/c
20 GeV/c
10 GeV/c
NUMBER OF CELLS
30
25
20
15
10
5
0
0.5
1.0
1.5
2.0
2.5
3.0
3.5
COLLISION LENGTH
0
2
4
6
8
10
12
14
16
RADIATION LENGTH

Fig. 16

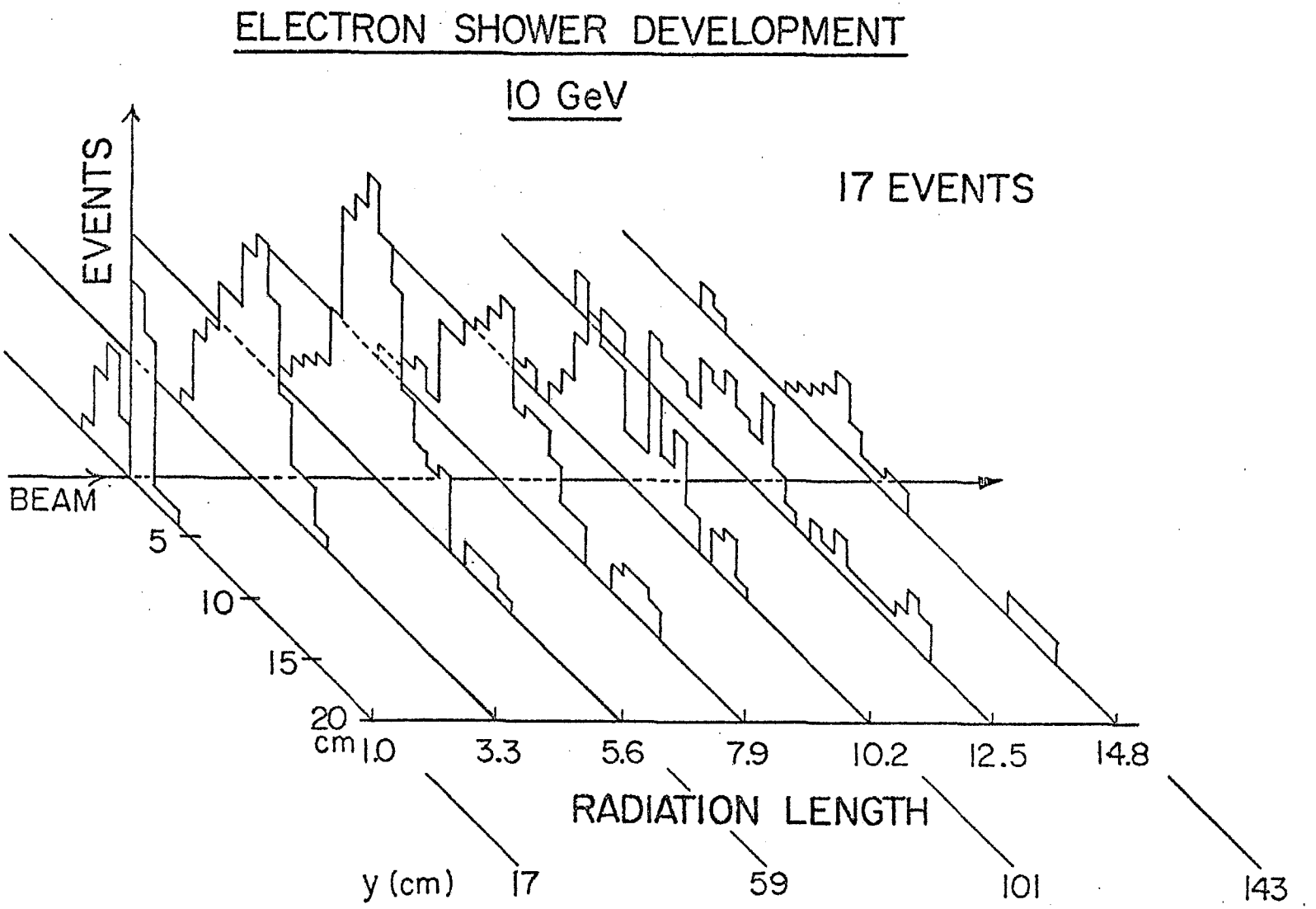
ELECTRON SHOWER DEVELOPMENT
10 GeV
17 EVENTS
EVENTS
BEAM
5
10
15
20
cm
1.0
3.3
5.6
7.9
10.2
12.5
14.8
RADIATION LENGTH
y (cm)
17
59
101
143

Fig. 17a

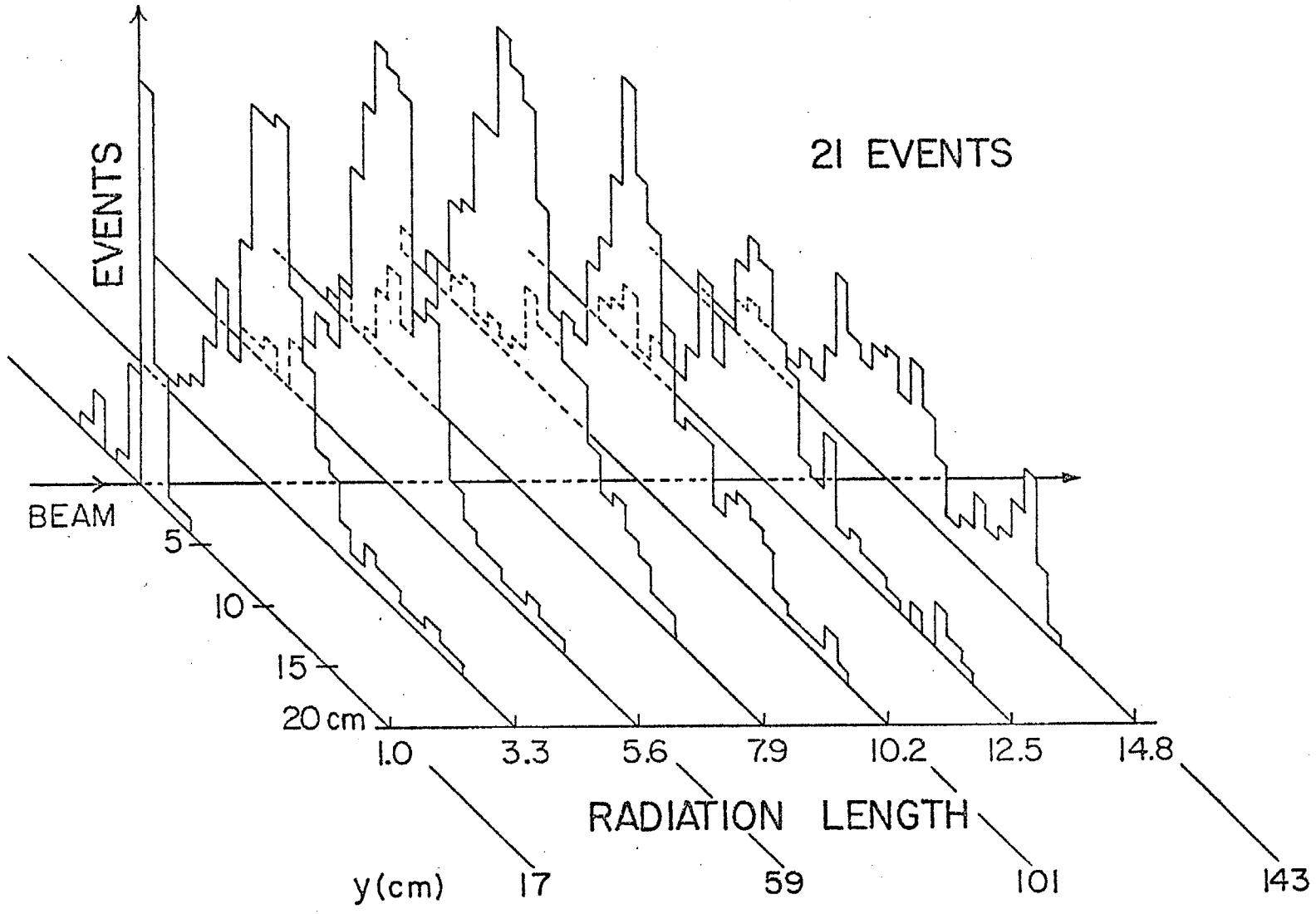
ELECTRON SHOWER DEVELOPMENT
30 GeV
EVENTS
21 EVENTS
BEAM
5
10
15
20 cm
1.0
3.3
5.6
7.9
10.2
12.5
14.8
RADIATION LENGTH
y(cm)
17
59
101
143

Fig. 17b

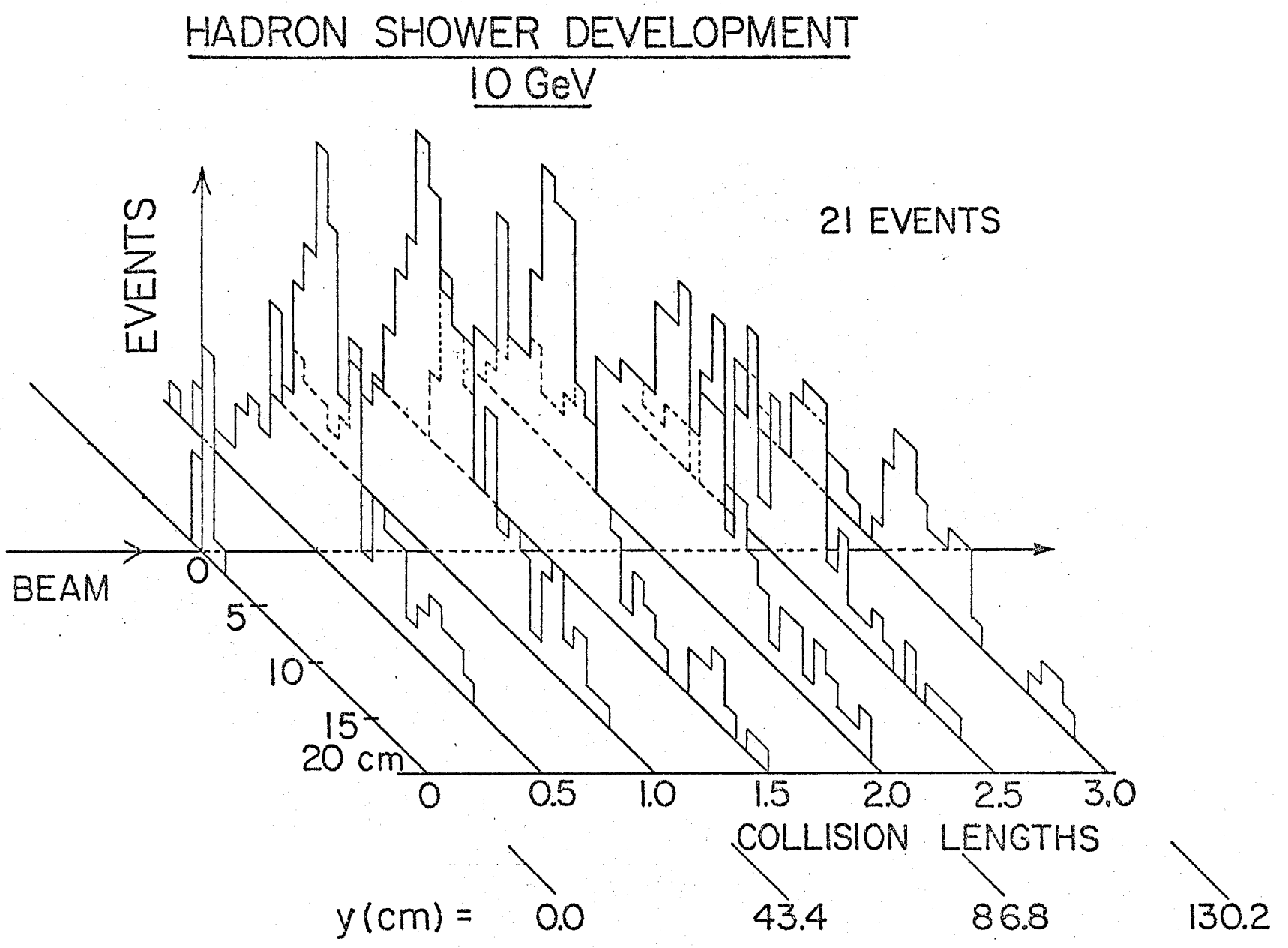
HADRON SHOWER DEVELOPMENT
10 GeV
EVENTS
21 EVENTS
BEAM
0
5
10
15
20 cm
0
0.5
1.0
1.5
2.0
2.5
3.0
COLLISION LENGTHS
y(cm) =
0.0
43.4
86.8
130.2

Fig. 18a

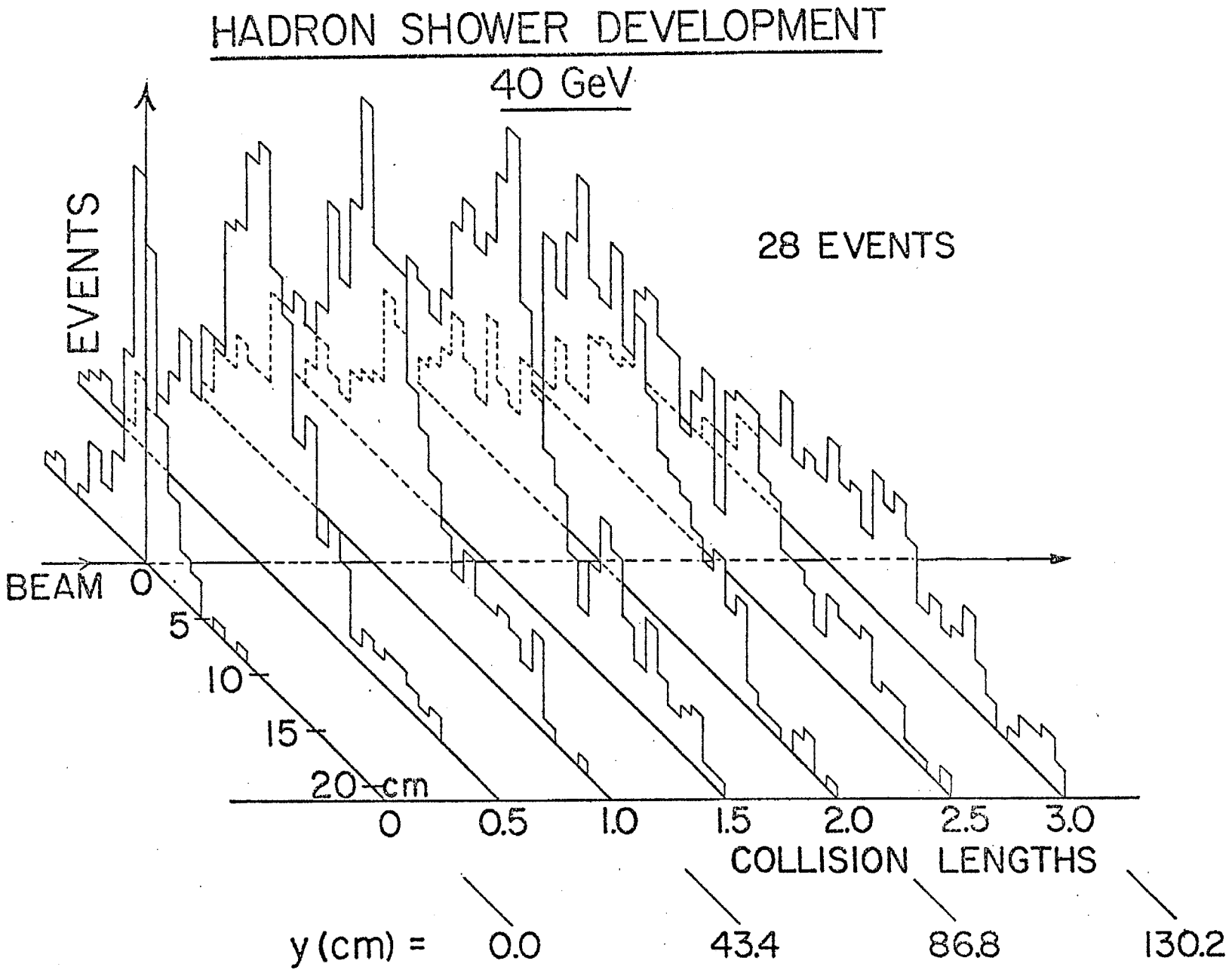
HADRON SHOWER DEVELOPMENT
40 GeV
28 EVENTS
EVENTS
BEAM
0
5
10
15
20 cm
0
0.5
1.0
1.5
2.0
2.5
3.0
COLLISION LENGTHS
y (cm) =
0.0
43.4
86.8
130.2

Fig. 18b

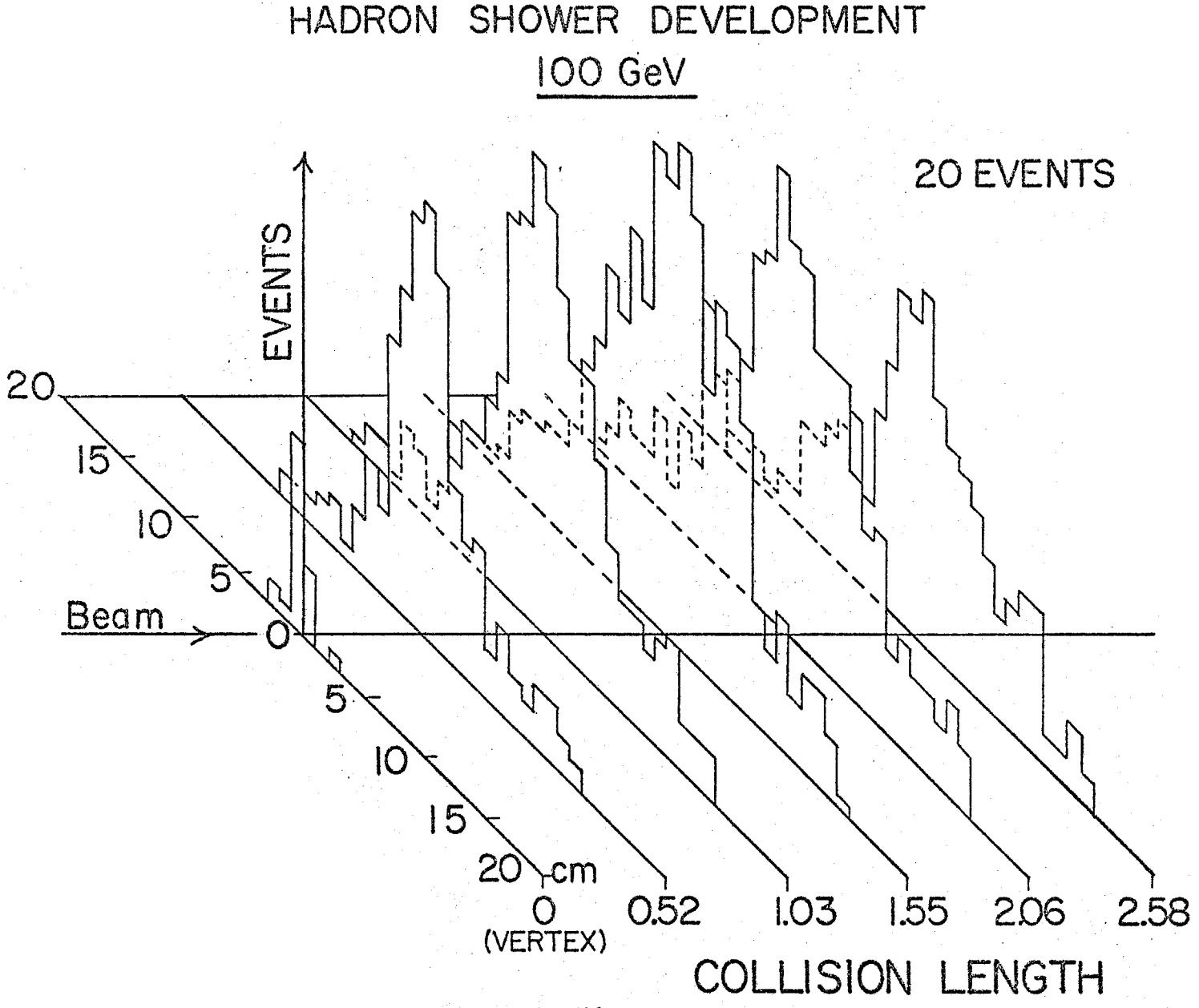
HADRON SHOWER DEVELOPMENT
100 GeV
20 EVENTS
EVENTS
20
15
10
5
Beam
0
5
10
15
20 cm
0
(VERTEX)
0.52
1.03
1.55
2.06
2.58
COLLISION LENGTH

Fig. 18c

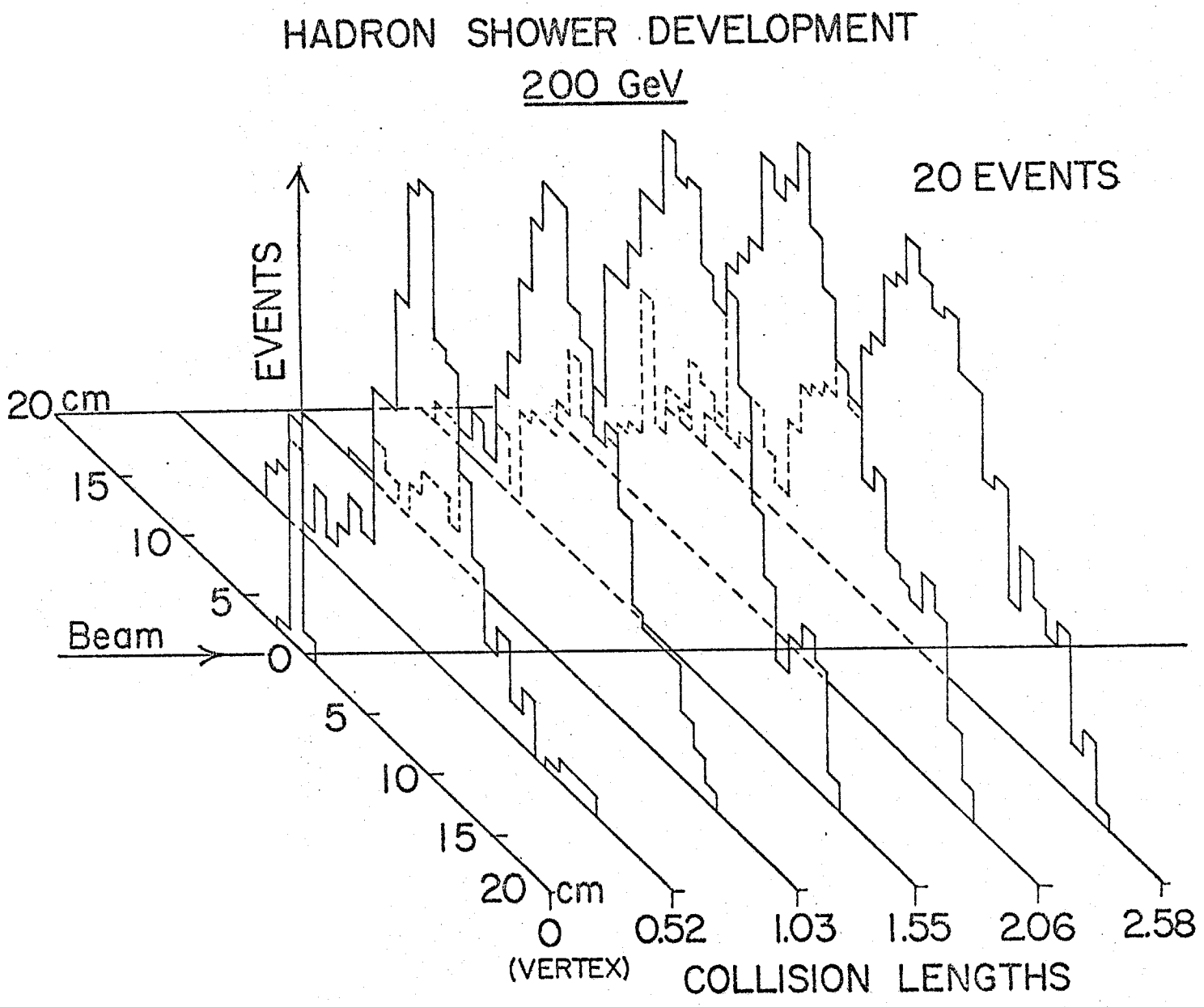
HADRON SHOWER DEVELOPMENT
200 GeV
20 EVENTS
EVENTS
20 cm
15
10
5
Beam
0
5
10
15
20 cm
0
(VERTEX)
0.52
1.03
1.55
2.06
2.58
COLLISION LENGTHS

Fig. 18d

APPENDIX B

Magnetostrictive Read Out System

We have studied the possibility of reading out the flash chambers using conventional magnetostrictive lines. Figure 1 shows the most successful method employing this technique thus far. For several inches the normal ground electrode is replaced by a series of narrow copper strips connected to ground via narrow "sense" wires. The strips, wires, and common ground are made by an etching process using copper clad mylar. Figure 2 shows the shape of a portion of the etched mylar. Small 3mm diameter holes in the polypropelene below the copper strips allow direct contact between the plasma in a struck cell and the copper. The magnetostrictive line is placed on the narrow "sense" wires. We have found that currents of several Amperes can be made to flow from the plasma to ground. This is adequate for detection of the glow discharge via magnetostrictive line.

Figure 3a shows some typical pulses observed at the output of the preamplifier connected to the pick up coil at the end of the magnetostrictive line. Single pulses of 0.8 volt amplitude are seen with the amplifier noise level at around 0.015 volts. When two adjacent cells fire, due to a delta ray knock on or the development of a shower, the typical observed pulse pattern is shown in Figure 3b. The two pulses at the output of the wire amplifier are well separated. The output of the wire amplifiers have been fed into a discriminator to produce separated pulses.
Figure 3c shows the pulse pattern when many adjacent cells have fired. The pulses are well separated and can be treated in a digital fashion after firing the discriminator

We have investigated the uniformity of the preamplifier output pulses. Figure 4 shows these distributions for cases of:

a. Firing of a single cell.

b. The second pulse of an adjacent double cell firing.

c. The third pulse of an adjacent triple cell firing.

These distributions are shown by the solid histogram and are seen to be consistent with one another. These events were initiated by a particle traversing the flash chamber 0.5m from the magnetostrictive line. The measurements were repeated with the triggering particle now 2m from the magnetostrictive line. In this case, the plasma propagates down the cell for the full 2m distance. The pulse height distributions are shown by the dashed histogram and are consistent with the measurements at 0.5m. We conclude that the flash chamber and magnetostrictive read out provides a uniformly sensitive detector.

We have studied the output pulse height from a given cell versus high voltage applied to the chamber. Figure 5 shows that there is a smooth increase in output pulse height over a wide range of high voltage. The previous results were obtained at 9 KV.

To maxmize the output pulse for a given high voltage we have studied the dependence on number and spatial distribution of holes in the polypropelene. Figure 6 shows some data for four holes with varying interhole distance. The density of the plasma can not sustain small interhole distance. Figure 7 shows that for an interhole distance of 8 cms the output pulse increases roughly linearly with number of holes. In this manner, approximately 1.5 ampere/hole is obtained from the plasma.

All of the above tests were performed with sense wires and preamplifier separated by roughly 0.6m. We have extended these measurements to 2.3m ($\approx$ maximum required distance) and find the pulse attenuation is a factor of 2 to 4 depending on the wire,but the dispersion is small enough to still cleanly separate the adjacent cells. Some ringing after the initial pulse is observed for the "standard" 4 x 20 mill wire used for all of the previous work (see Figure 3). Depending on the discriminator level and distance of the sense wire from the preamplifier this ringing may cause the refiring of the discriminator after the initial pulse. This effect is worse for longer lengths of magnetostrictive line as seen in Figure 8 . However, we have found that for wire which has an aspect ratio of 5 mil x 12 mil or even round wire the ringing is totally suppressed. This is shown in Figure 9.

In conclusion, we have developed a stable, reliable, technically straightforward and inexpensive magnetostrictive readout from the flash chambers.

We have designed and begun to build the electronic read out system which records only the hit cells in the neutrino target. The system is fully modular. One read out module is connected to each sub-module of flash chambers (as defined elsewhere). A cost estimate for the total read out system is $100K.

CHAMBER CONSTRUCTION FOR MAGNETOSTRICTIVE READOUT

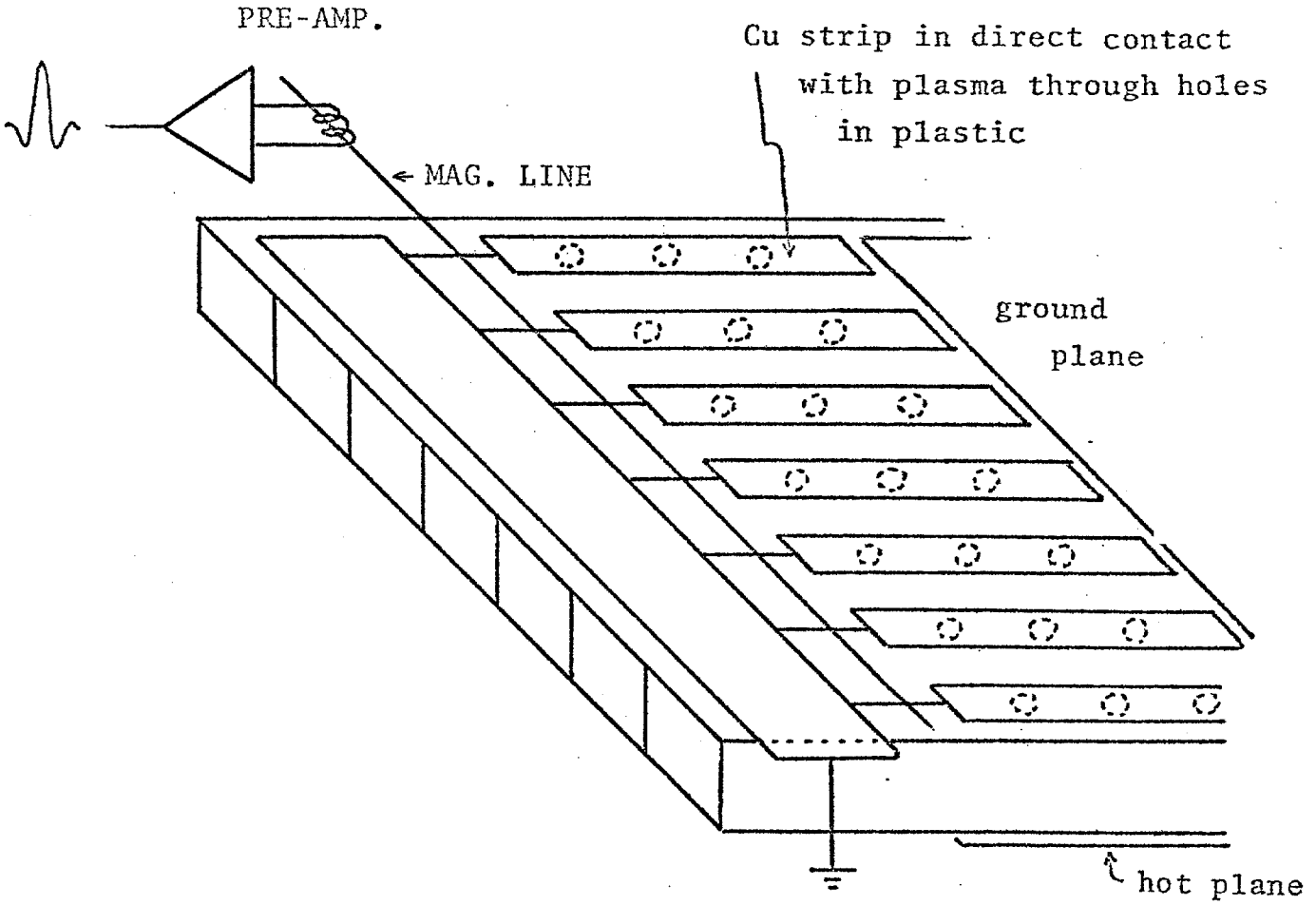

Fig. 1

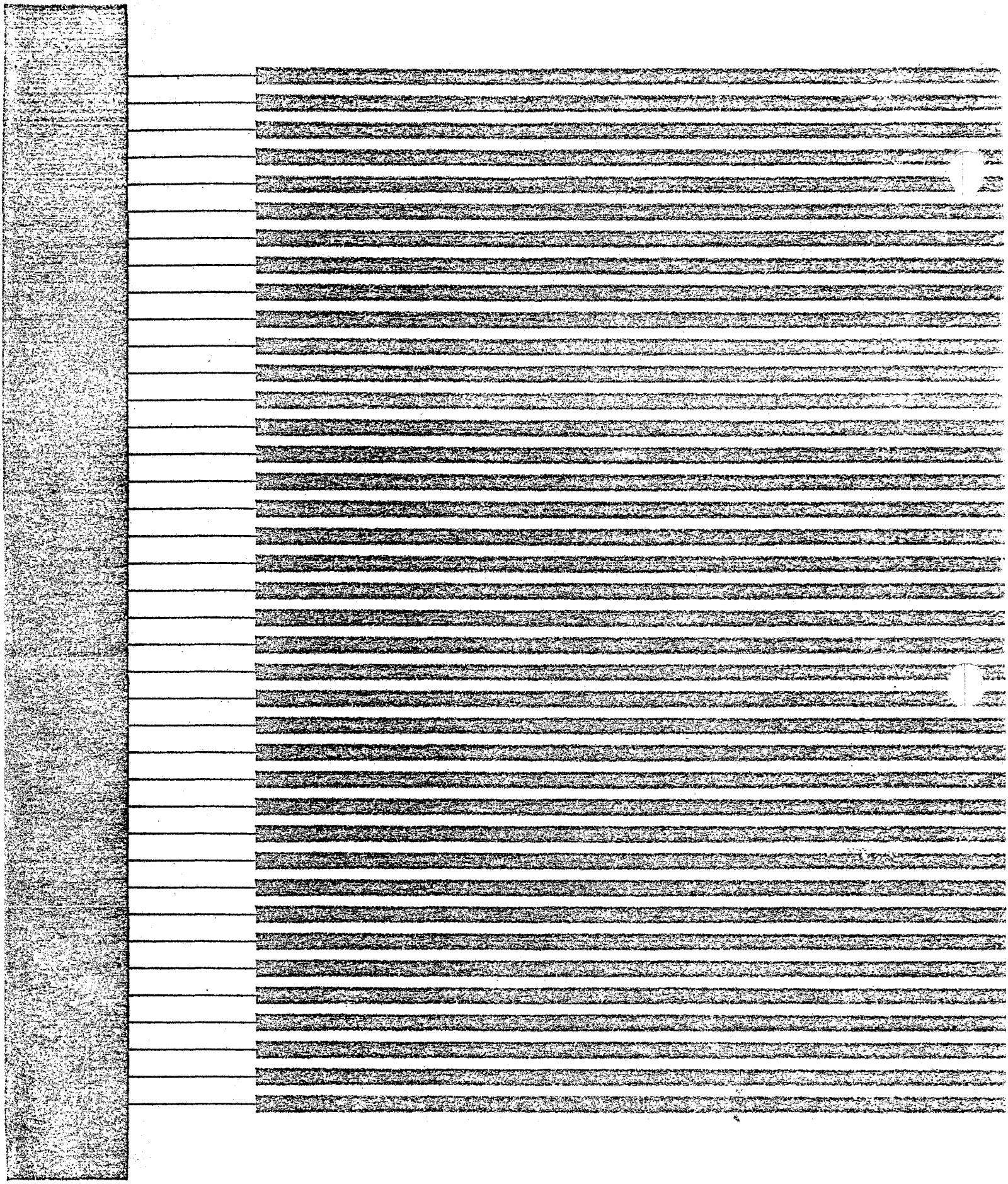

Fig. 2

OUTPUT OF MAG. LINE PRE-AMP.

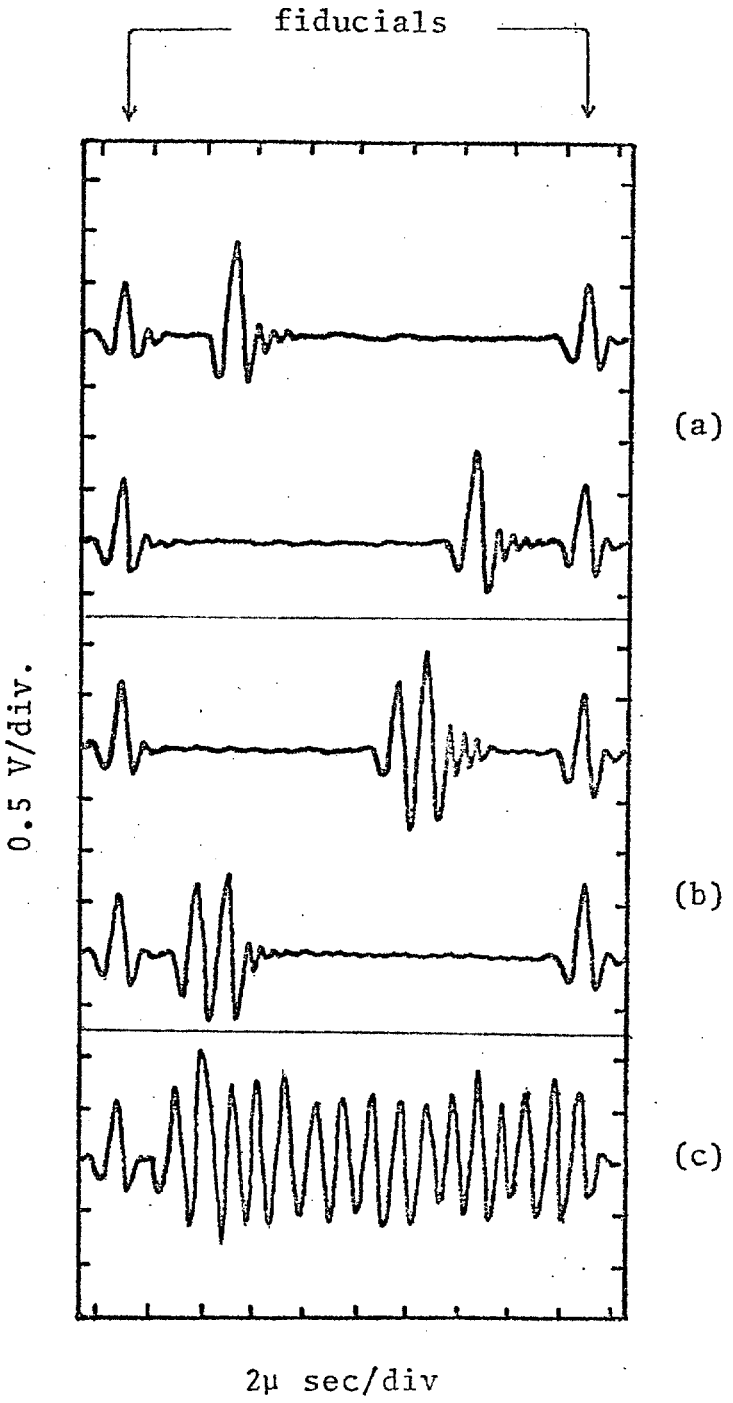

Fig. 3

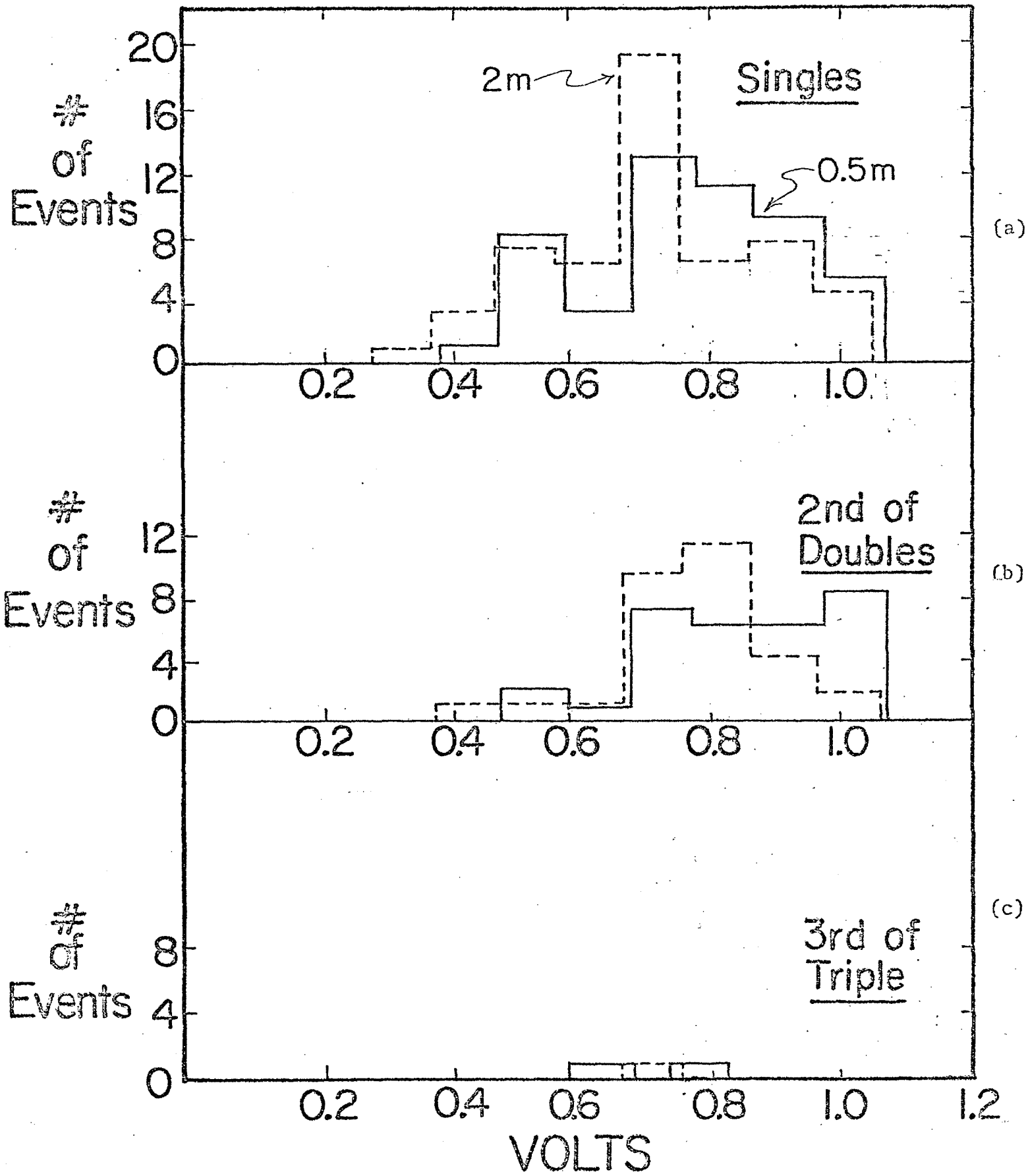
20
16
12
8
4
0
# of Events
2m
Singles
0.5m
(a)
0.2
0.4
0.6
0.8
1.0
12
8
4
0
# of Events
2nd of Doubles
(b)
0.2
0.4
0.6
0.8
1.0
8
4
0
# of Events
3rd of Triple
(c)
0.2
0.4
0.6
0.8
1.0
1.2
VOLTS

Fig. 4

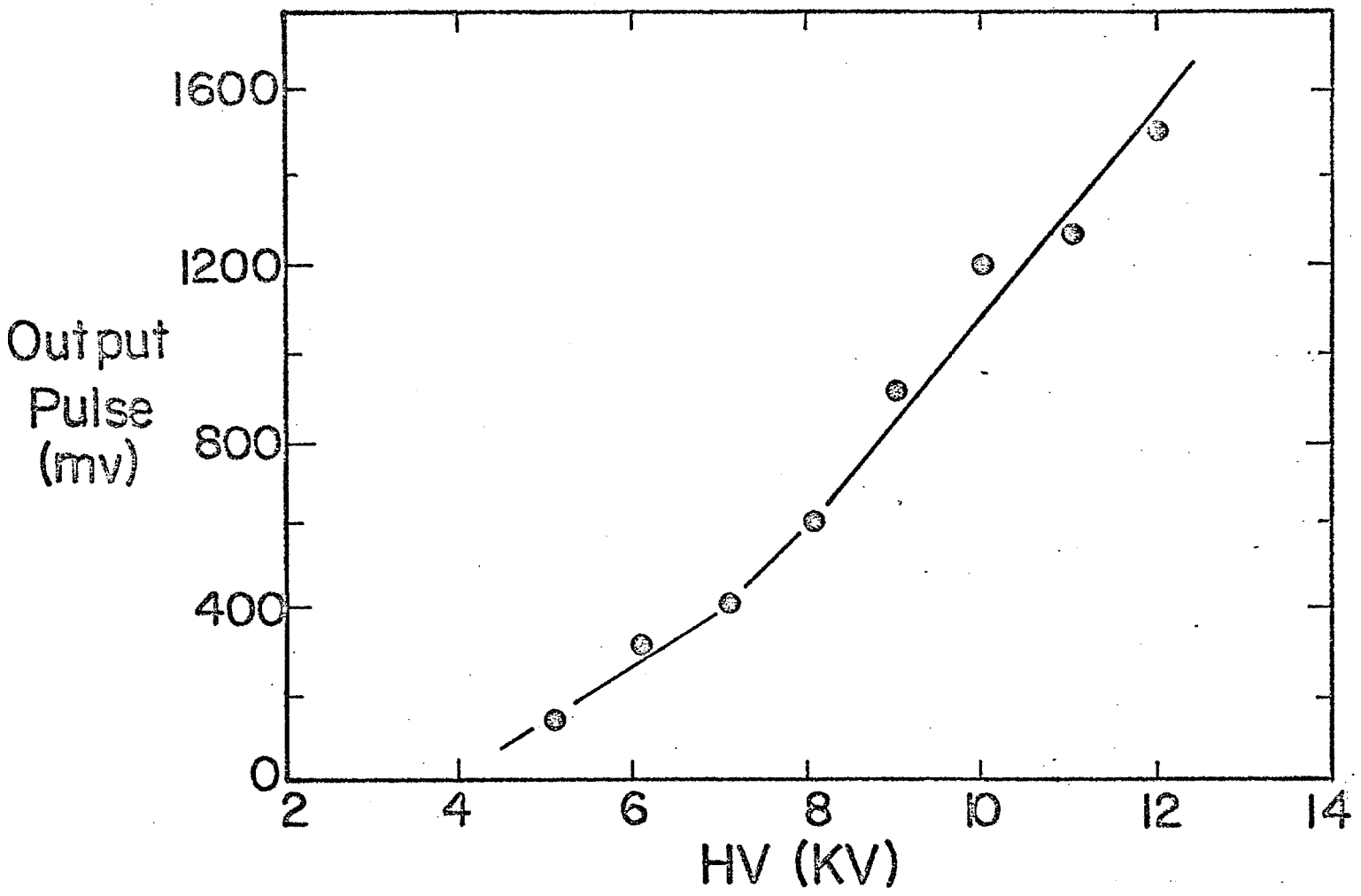

Fig. 5

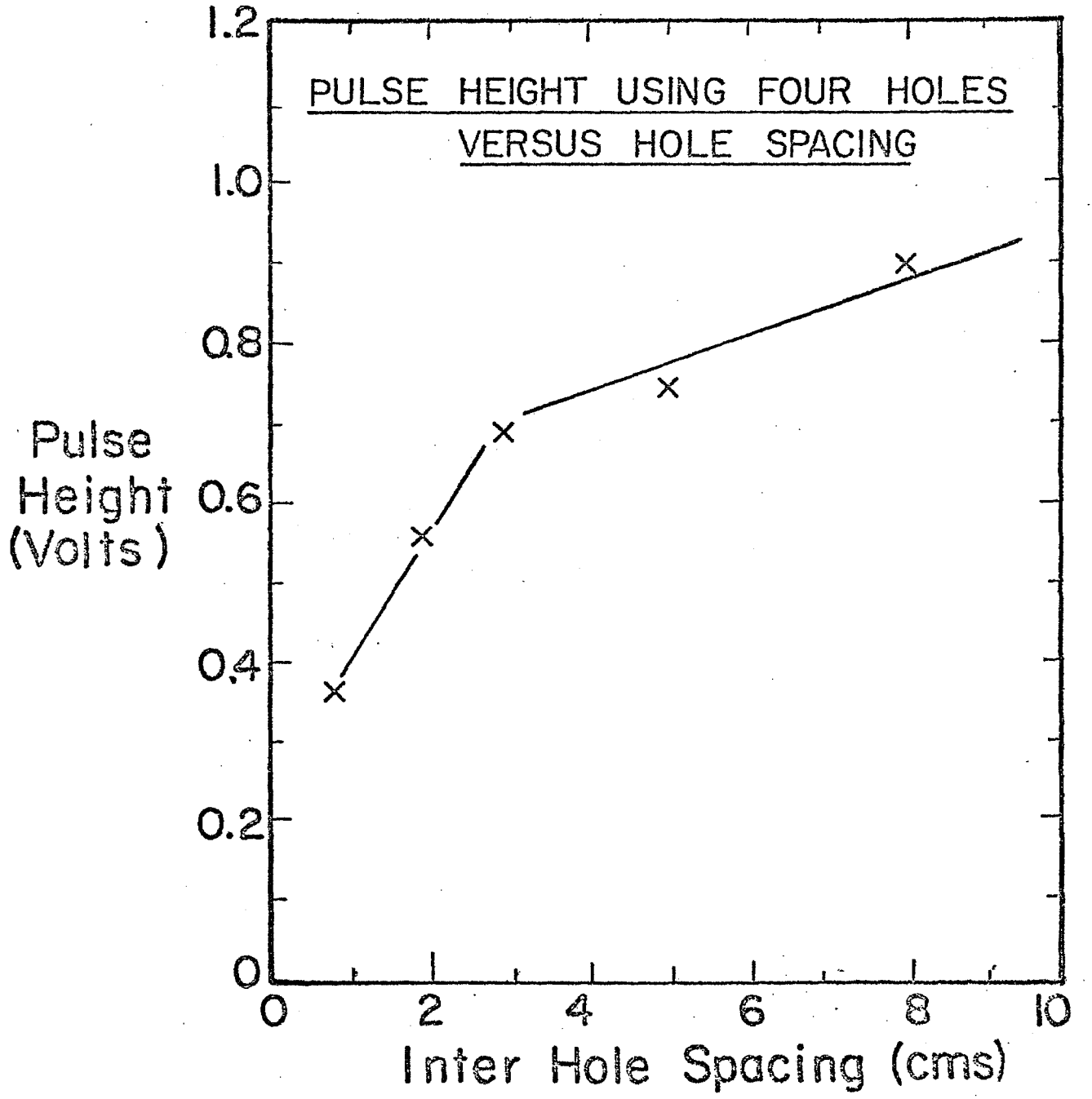
PULSE HEIGHT USING FOUR HOLES
VERSUS HOLE SPACING
Pulse Height (Volts)
1.2
1.0
0.8
0.6
0.4
0.2
0
0
2
4
6
8
10
Inter Hole Spacing (cms)

Fig. 6

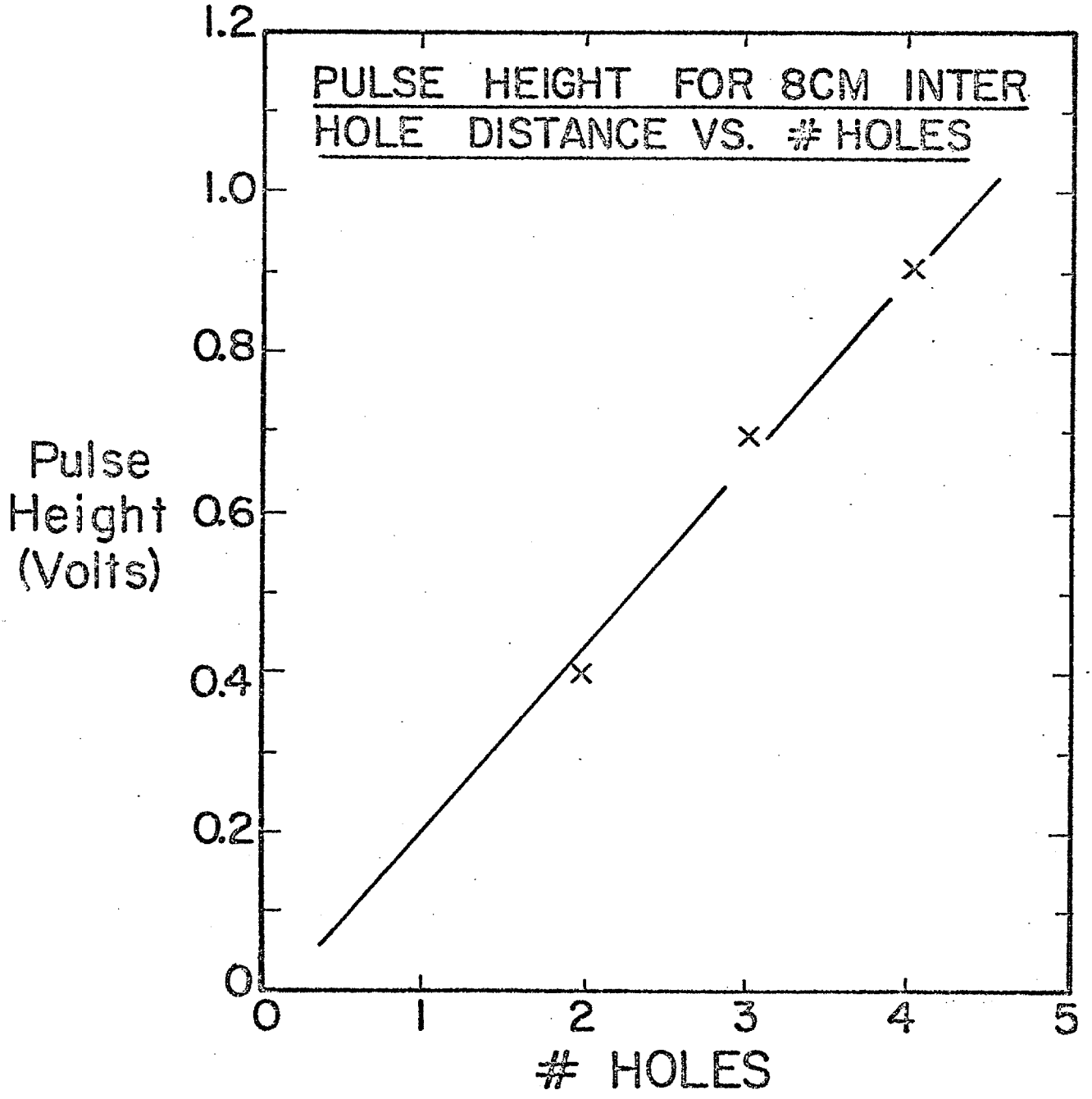
PULSE HEIGHT FOR 8CM INTER
HOLE DISTANCE VS. # HOLES
Pulse
Height
(Volts)
1.2
1.0
0.8
0.6
0.4
0.2
0
0
1
2
3
4
5
HOLES

Fig. 7

MAGNETOSTRICTIVE PULSES

LINE 4 x 20 MILL

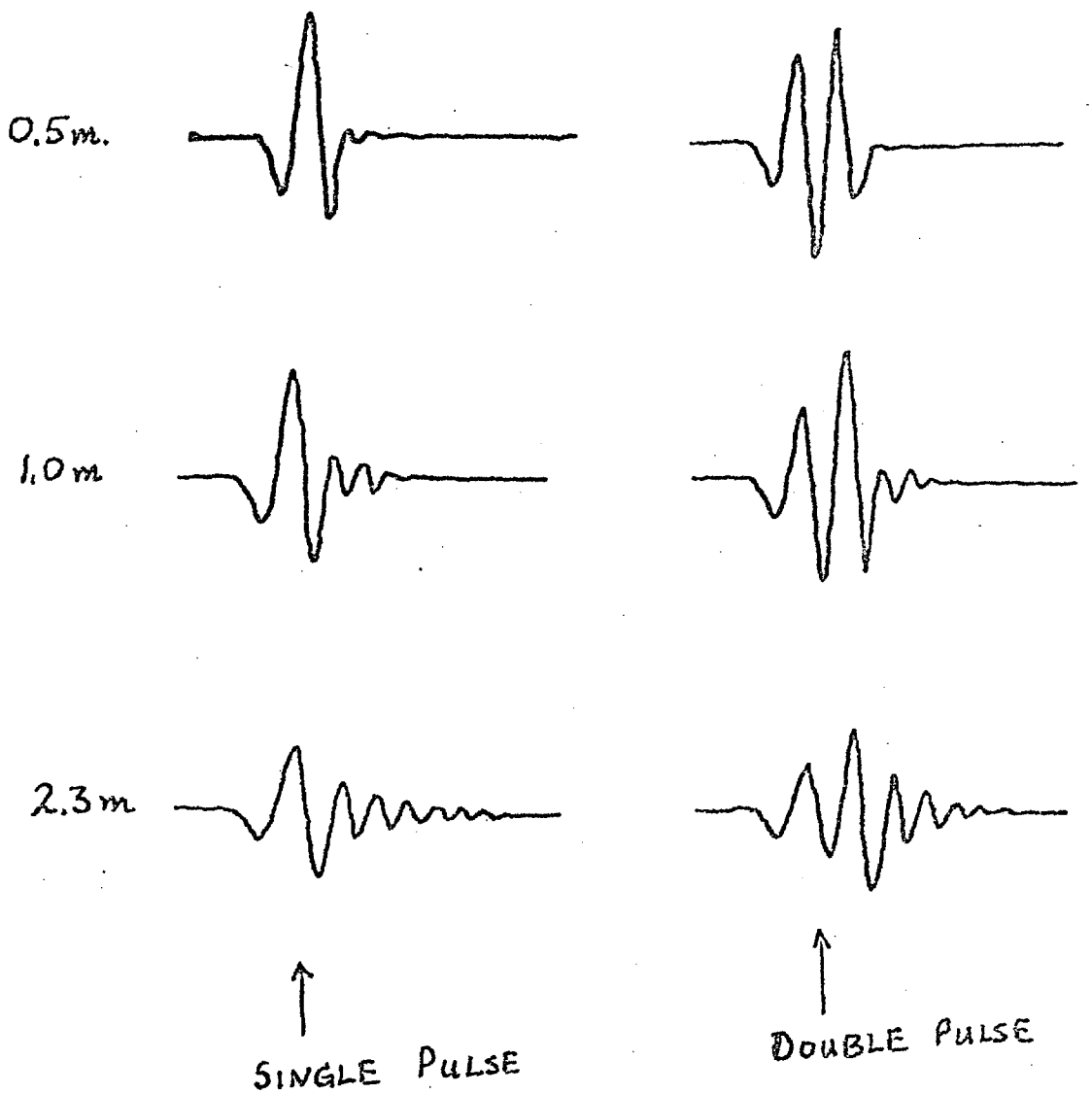

Fig. 8

MAGNETOSTRICTIVE PULSES

LINE 5 x 12 MILL

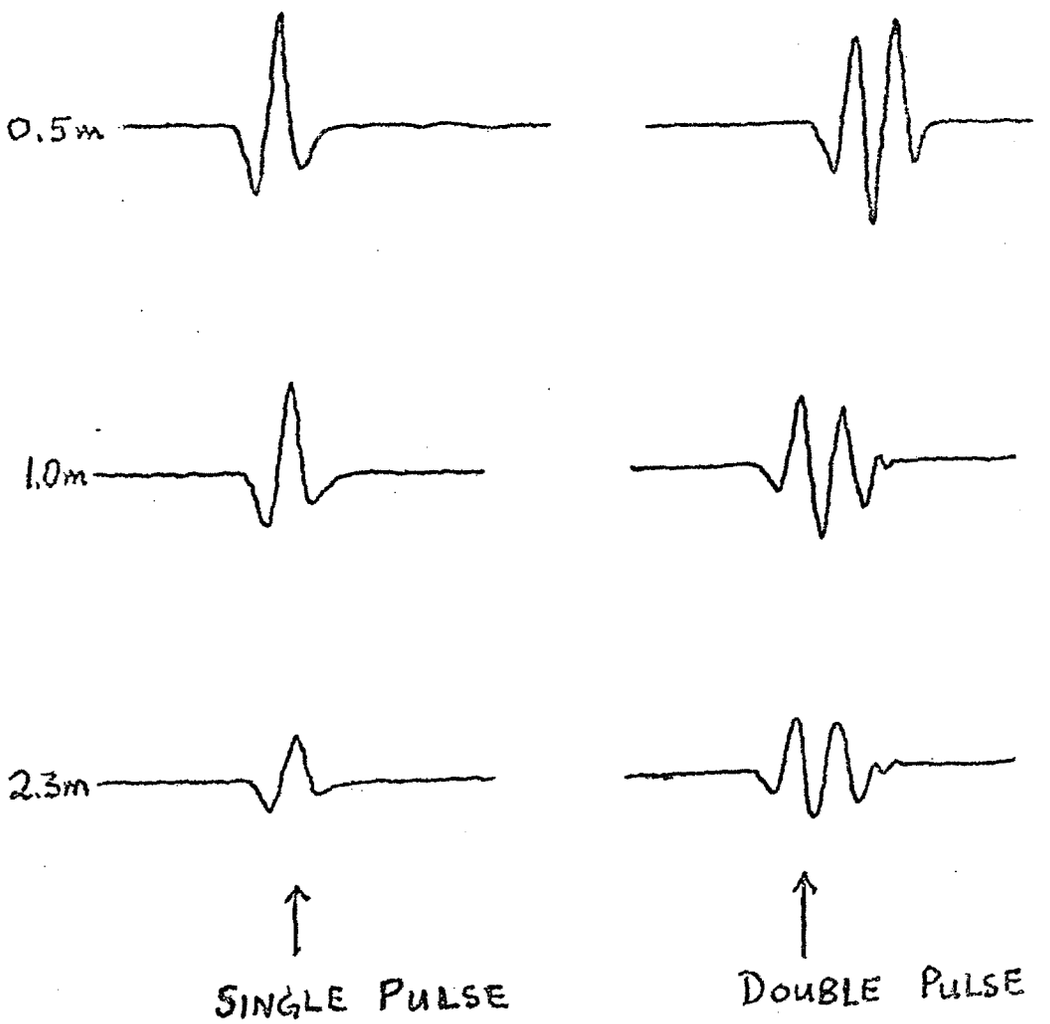

Fig. 9